ABSTRACT

WILBANKS, MATT CHESTON. Near Surface Density Currents Observed in the Southeast Pacific Stratocumulus-Topped Marine Boundary Layer. (Under the direction of Sandra Yuter.)

Ship-based observations obtained during the 2008 VOCALS-Rex campaign reveal the presence of 70 near surface density currents in the Southeast Pacific (SEP) stratocumulus-topped marine boundary layer. Scanning High Resolution Doppler Lidar (HRDL) was employed to capture the evolving horizontal and vertical structures of these features for the first time. We characterize and contextualize the phenomenology of the observed density currents and provide new insights about their roles in boundary layer transport and mesoscale convective organization. Four contrasting mature and relatively strong density currents are examined in detail. The mesoscale environment and vertical structure of the boundary layer associated with each event provide insight into the physical mechanisms for density current propagation and their relationship to convective initiation. Seventy density currents identified using a frontal zone slope criterion applied to the ship-level air density time series are used to determine bulk properties. Our density current identification method is similar but not identical to Terai's (2011) analysis of cold pool edges in the SEP based on aircraft flight-level data.

Density currents in the SEP stratocumulus region possess horizontal flow perturbations that are confined to the lowest 200-800 meters of the atmosphere and are observed to induce 0.5 m s^{-1} to 3.5 m s^{-1} updrafts along their frontal zones. Density currents occur preferentially in mesoscale environments with increased dry static stability and elevated areal average rain rates within 15 km of the ship. These findings are consistent with the hypothesis that the observed density currents are outflows generated by the evaporation of drizzle below cloud base within less-coupled boundary layer environments. In some cases, the relative movement of an individual drizzle cell and associated

density current is such that the drizzle cell may benefit from upward moisture transport of its own cold pool. This positive feedback associated with RKW theory may help explain long-loved (> 1 hr) drizzle cells observed in ship C-band radar data sets.

Near Surface Density Currents Observed in the Southeast Pacific Stratocumulus-Topped Marine
Boundary Layer

by
Matt Cheston Wilbanks

A thesis submitted to the Graduate Faculty of
North Carolina State University
in partial fulfillment of the
requirements for the degree of
Master of Science

Atmospheric Science

Raleigh, North Carolina

2013

APPROVED BY:

_____   _____

Sandra Yuter   Matthew Parker

Chair of Advisory Committee

_____

Walter Robinson

ACKNOWLEDGMENTS

TABLE OF CONTENTS

LIST OF FIGURES

CHAPTER 1

Introduction

Cold, dense near surface outflows (also known as atmospheric density currents or gravity currents) have been demonstrated to play a key role in the organization and formation of mesoscale convective activity in a variety of atmospheric environments. These outflows are generated when cooler, negatively buoyant air descends through the atmosphere until it reaches the surface, where it diverges and propagates out radially into the surrounding boundary layer. The dynamics that drive density current flows are very similar throughout a broad spectrum of interactions between fluids of different densities. The kinematic structure and evolution of density currents have therefore been described extensively in both laboratory and observational settings (Simpson 1997).

Evaporative cooling of precipitation has been known for some time to generate downdrafts and subsequent outflows (Srivastava 1987). Outflows generated by deep convection have been the subject of numerous studies, particularly in mid-latitude continental environments (Wilson and Schreiber 1986; Charba 1974; Engerer 2008; Goff 1976; Wakimoto 1982; Droegemeier and Wilhelmson 1987; Mahoney 1988; and many others). The phenomenon is also described in studies of deep convection over tropical oceans (Houze 1977; Gamache and Houze 1982; Zipser 1977; and many others). However, outflows generated by shallow precipitating clouds have received considerably less attention in the literature. Outflows have been studied beneath precipitating trade cumulus clouds (Zuidema et al. 2012; Snodgrass et al. 2009). Outflows found beneath drizzling subtropical marine stratocumulus in particular have been documented only recently (Terai 2011; Feingold et al. 2010; Jensen et al. 2000). Subtropical marine stratocumulus are capped by a strong inversion and are therefore confined to the boundary layer below ~2000 meters. This limits the intensity of precipitation and therefore the size and intensity of precipitation-generated outflows and

1

their associated temperature perturbations. Owing to higher relative humidities in marine boundary layers, evaporative cooling is also generally less intense, producing weaker cold pools. Despite the smaller scale of the outflows, the dynamics which drive their propagation and their effect on the circulation patterns beneath the cloud deck appear to be similar to outflows generated by deep convection.

Precipitation-induced outflows have been proposed to modify mesoscale circulation patterns below cloud in two ways. Of primary interest has been the role of mechanical lifting along the frontal boundary of outflows. This lifting occurs because of the prefrontal surface pressure maximum, which is related to the dynamic and buoyancy terms in the diagnostic pressure equation, and has been associated with convective initiation. Lifting is more intense and extends higher when two outflows collide, and this mechanism is most effective at generating convection when the two outflows collide head-on (Wilson and Scheiber 1986; Harrison 2009; Wakimoto & Kingsmill 1995). A second way that outflows may affect mesoscale circulations below cloud is by suppressing convective activity behind the frontal zone. This suppression can occur because the near surface wind field diverges within the outflow. Additionally, the colder near-surface air within the outflow can increase static stability in the boundary layer, which tends to reduce surface-based convection. A proposed theory for convective initiation along an outflow boundary in environments with preexisting wind shear is provided by Rotunno et al. (1988) and Weisman and Rotunno (2004)—often referred to eponymously as RKW theory. Fig. 1.1 shows how the horizontal circulation generated along an outflow frontal boundary can be counteracted or reinforced by the presence of environmental shear, which is the essence of RKW theory. The figure indicates that convective initiation along the outflow boundary is deeper and more sustained when the vorticity associated with environmental wind shear roughly balances the vorticity generated by the outflow circulation (Fig. 1.1 b). If, on the other hand, the combined vorticity associated with the outflow circulation overwhelms or is compounded by the

2

environmental shear generated vorticity, the convection slants backward with height up and over the cold pool behind the frontal zone (Fig. 1.1 c). This third configuration is not ideal for further convective development along the frontal zone because the convection is not aligned with updraft and is instead positioned over a layer of stable air.

Although RKW theory has been primarily applied to deep convective squall lines, convective initiation along outflow boundaries has been observed in regions of shallow convection as well. Zuidema et al. (2012) and Snodgrass et al. (2009) studied cold pools generated by precipitating trade wind cumulus clouds and their effect on ~ 3 km deep convection in the subtropical Atlantic using ship and satellite data. The highest precipitation rates presented in Zuidema et al. (2012)—~3 mm d^{-1}— and Snodgrass et al. (2009) —~25 mm d^{-1}—were found within a precipitation field organized along mesoscale arcs that outlined previous precipitation outflow boundaries. Zuidema et al. (2012) also observed the individual arcs propagating with respect to the mean wind field at speeds indicating that precipitation was being reinforced along an ~200 meter deep outflow boundary. Jensen et al. (2000) presented aircraft data taken beneath a closed cell stratocumulus region west of Tasmania during the Southern Ocean Cloud Experiment. They found consolidated, often linear subcloud cumulus structures which appeared to be connected to the stratocumulus deck along the frontal zone of drizzle-induced cold pools. They also observed moderately intense drizzle (R ≈ 5 mm d^{-1}) beneath these structures. The cloud structures propagated faster than the ambient wind and the authors suggested that they behaved analogously to deep convective squalls.

Much like deep convection, drizzling regions that are embedded within marine stratocumulus have been observed to exhibit a characteristic cellular kinematic structure. Comstock et al. (2007) explored the horizontal wind patterns within and below drizzling marine stratocumulus using C-band radar data collected during the 2001 EPIC campaign. Fig. 1.2 shows an example drizzle cell

kinematic structure within an open cell region. The y-axis of the two subplots is normalized to cloud top height. The drizzle cell exhibits a near surface divergent flow, which is attributed to a precipitation-induced downdraft. There is also divergence aloft associated with a combination of the effect of the latent heating profile on pressure perturbations in the updraft region (Pandya and Durran 1996) and mass continuity as rising air within the updraft encounters the stability boundary of the inversion. Notably, the inflow is at mid-levels rather than being surface-based. Leon (2006) found smaller (3-5 km) structures that were very similar in unbroken stratocumulus using observations from airborne vertically-pointing radar. The pattern of mid-level inflow and cloud-level outflow bears striking similarities to deep convective kinematic structures as exemplified in a horizontal flow field surrounding a simulated mesoscale convective system (MCS) shown in Fig. 1.3 (Fovell 2002). Latent heating is maximized in the middle levels and forms a low pressure region which draws in air from adjacent regions within the layer, creating the inflow. The kinematic similarities between drizzle cells and MCSs suggest that the two behave essentially the same way. The primary differences are that drizzle cells are smaller, shallower, and transport less energy than MCSs.

The influence of precipitation-induced surface outflows on the mesoscale pattern of convective activity in marine stratocumulus-topped boundary layers was explored in Feingold et al. (2010). They used an LES model and a simplified 2-D Rayleigh-Bernard convection model to simulate open mesoscale cellular convection (Fig. 1.4a). They also provided a composite image containing a C-band radar range-height indicator (rhi) scan superimposed onto a lidar rhi scan (Fig. 1.4b). The lidar and radar data used in Feingold et al. (2010) were collected in the Southeast Pacific marine stratocumulus region during the VOCALS-REx campaign. We use their outflow in our analysis. Fig 1.4b depicts a colliding outflow boundary in an open cellular region and its close proximity to precipitation. The rhi scans were used to support their theory that open mesoscale cellular convection (MCC) behaves like a system of coupled, oscillating cloudy/precipitating and

4

cloud-free regions. In their model, the precipitating regions of open MCCs evolve into cloud-free regions as convection is suppressed by evaporatively-cooled downdrafts and surface divergence (i.e. precipitation outflows). Conversely, precipitation outflows that propagate out into the cloud-free regions and collide with one another are proposed as the generative mechanism for new convection and therefore new cloudy/precipitating regions. The authors argued on the basis of apparent similarities between their model and limited observations of open cellular convection that the planform of open cellular convection was maintained through essentially this process.

Terai (2011) aggregated subcloud flight data collected at 150 meter height during VOCALS-REx and used a temperature drop criteria to identify the boundaries of 80 cold pools below marine stratocumulus in the Southeast Pacific. He found that the air inside cold pool boundaries was on average 0.4 K cooler and 0.45 g kg^{-1} moister than the air outside the cold pools, with elevated drizzle rates at cloud base (~2 mm d^{-1} on average) as well as cloud bases that averaged ~100 meters below the those of the surrounding areas. The mean updraft intensity along the cold pool boundaries averaged 0.2 m s^{-1}, and the cold pools contained air with higher equivalent potential temperature, an indicator of near-surface stability and reduced boundary layer mixing.

Previous studies of drizzle-induced cold, dense near-surface outflows beneath shallow, marine stratocumulus are limited in scope as they utilized data "snapshots" (Terai 2011; Jensen 2000; Feingold et al. 2010). This study is unique in that it employs a surface-based high-resolution scanning Doppler lidar (HRDL) to examine the *evolution* of the detailed kinematic structures associated with seventy outflows. The analysis also incorporates a diverse and complementary set of *in situ* instruments as well as a scanning C-band radar to establish the relationship of drizzle outflows to the boundary layer thermodynamic, kinematic, and precipitation processes observed in the Southeast Pacific marine stratocumulus region. The goal of this study is to characterize and contextualize

5

drizzle outflow phenomenology and provide new insights about their role in boundary layer transport and mesoscale convective organization.
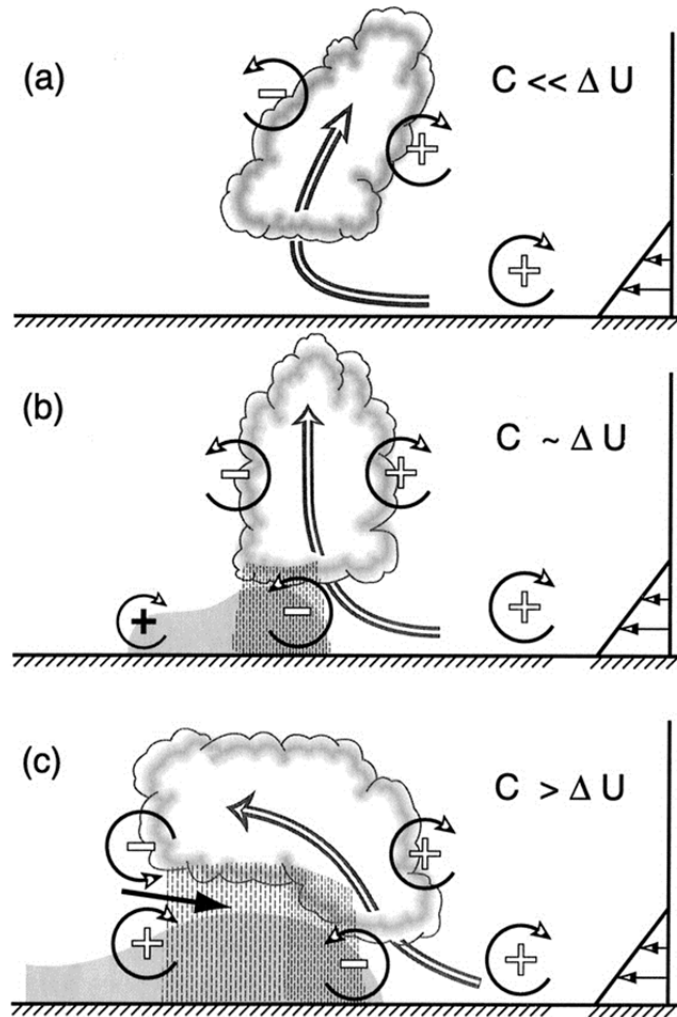
Fig. 1.1: Three stages in the evolution of a convective system. (a) An initial updraft leans downshear in response to the ambient vertical wind shear, which is shown on the right. (b) The circulation generated by the storm-induced cold pool balances the ambient shear, and the system becomes upright. (c) The cold-pool circulation overwhelms the ambient shear and the system tilts upshear, producing a rear-inflow jet. The updraft current is denoted by the thick, double-lined flow vector, and the rear-inflow current in (c) is denoted by the thick solid vector. The shading denotes the surface cold pool. The thin, circular arrows depict the most significant sources of horizontal vorticity, which are either associated with the ambient shear or which are generated within the convective system, as described in the text. Regions of lighter or heavier rainfall are indicated by the more sparsely or densely packed vertical lines, respectively. The scalloped line denotes the outline of the cloud. Here, C represents the strength of the cold pool while Δu represents the strength of the ambient low-level vertical wind shear, as described in the text (adapted from Weisman 1992). From Weisman and Rotunno (2004), their Fig. 2.
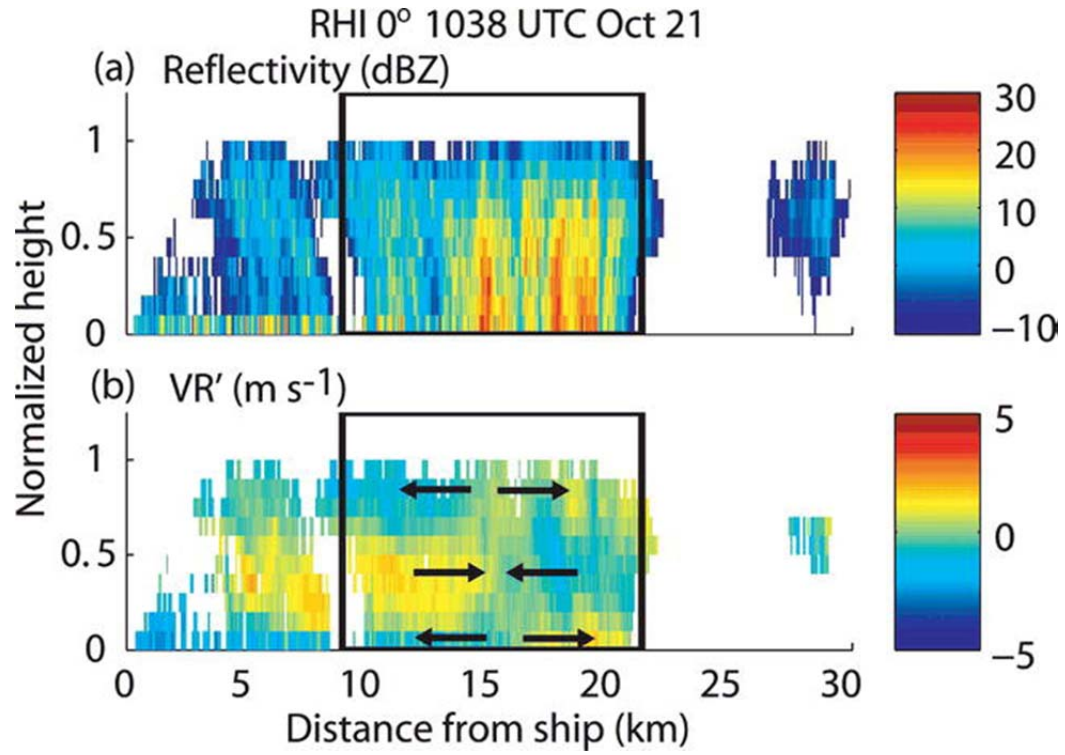
Fig. 1.2: Example of near-surface divergence in a drizzle cell transected by the 0° RHI at 1038 UTC 21 Oct (open-cellular cloud structure): (a) reflectivity and (b) anomalous radial velocity, VR′, where negative velocity is toward the radar. Arrows represent directions of radial inflow and outflow and are not drawn to scale. From Comstock et al. 2007, their Fig. 10.
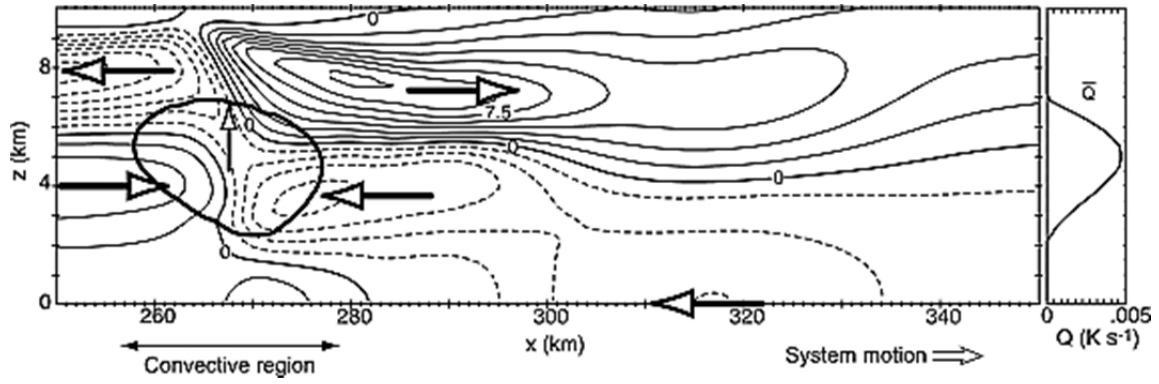
Fig. 1.3: Response to convective region heating in a simulated MCS. The circle outlined by the bold line shows the area in which heating was applied. Contours show the horizontal velocity response to the mean convective region heating profile indicated in the right-hand panel. Contours of perturbation horizontal wind in the plane of the cross section are at intervals of 1.5 m s^{-1}, with dashed contours indicating right-to-left flow in the cross section. Large arrows emphasize direction of motion. From Houze (2004), their Figure 8. Adapted from *Fovell* (2002).

9
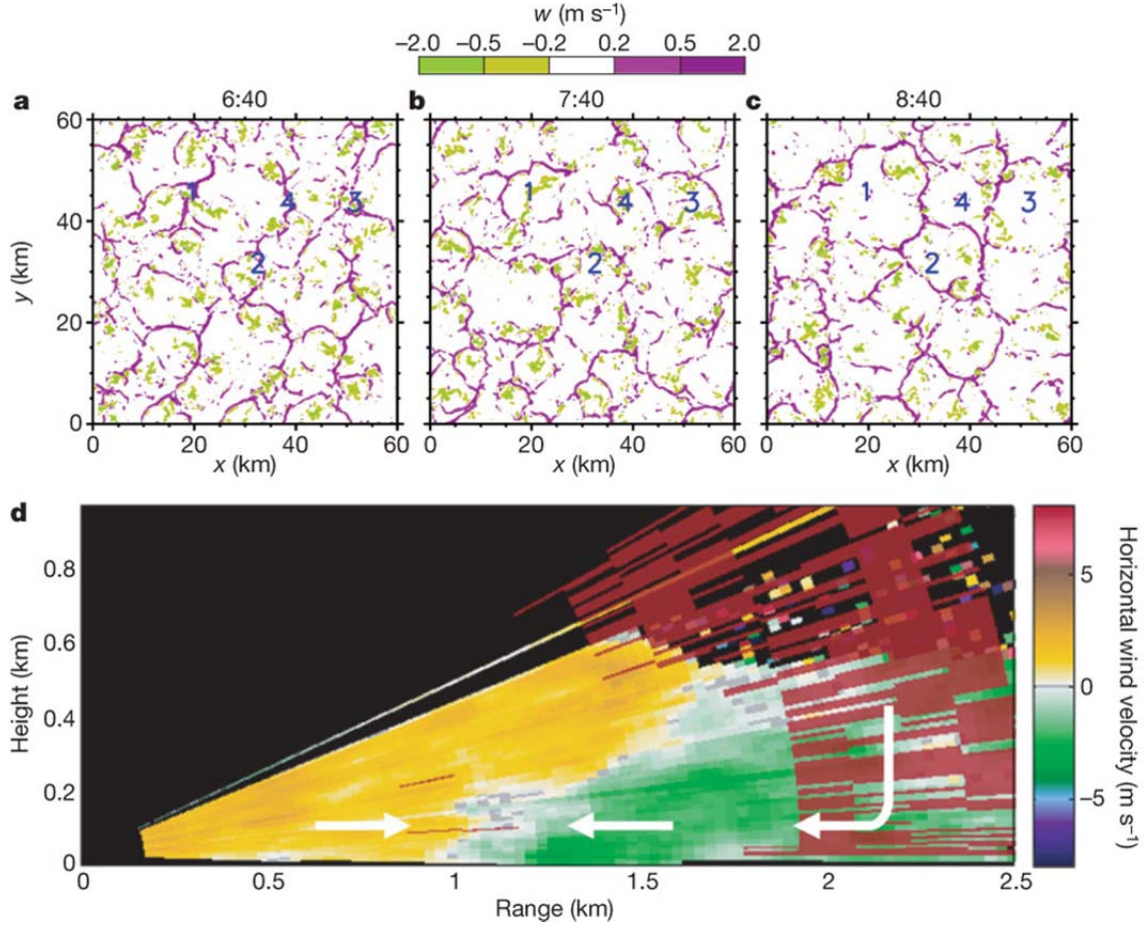
Fig. 1.4: Plan views of near-surface updraught (purple) and downdraught (green) patterns, each separated by one hour. *w* is vertical velocity; positive values are updraughts and negative values are downdraughts. Updraught regions correspond to surface convergence, and downdraughts to surface divergence zones. Four Y-shaped updraught patterns in **a** are labelled 1, 2, 3 and 4 to illustrate the evolution of the open cellular structures from one time (times relative to the start of the simulation) to the next (6:40 to 7:40 to 8:40). They occur at strong convergence zones and are favoured for the strongest convection. As time progresses (b and **c**), precipitation at these points changes the surface flow to a divergent one. New cellular structures emerge from the old planform as the cold-pool outflows interact with one another and generate new convergence zones that in turn generate new precipitation zones. d, Vertical cross-section of a precipitation-generated outflow and creation of a convergence zone as observed by ship-based radar and Doppler lidar (located at range 0 km and height 0 km). Radar reflectivity (>20 dB Z; dark red) is indicative of significant rain. Lidar data show air flow towards (green) and away from (yellow) the lidar. Arrows indicate the direction of flow. From Feingold et al. (2010), their Fig. 2.

Data and Methods

I. Data Sets

During the 2008 VOCALS-REx campaign, the National Oceanic and Atmospheric Administration (NOAA) research ship Ronald H. Brown (*RHB*) served as an instrument platform for observations of the marine boundary layer (Wood et al. 2011). An array of instruments on board collected ~35 days of data on cloud, precipitation, aerosol, and boundary layer properties while transecting the Southeast Pacific along 20°S between 70°W and 85°W. The instruments employed here include the scanning High Resolution Doppler Lidar (HDRL) (Grund et al. 2001), C-band precipitation Radar (Ryan et al. 2002), surface meteorology tower, laser ceilometer, passive microwave radiometer, Differential Mobility Particle Sizer (DMSP), Aerodynamic Particle Sizer (APS), sonic anemometer, and 4-hourly rawinsonde.

A. The Scanning High Resolution Doppler Lidar (HDRL)

i. Instrument Specifications

The scanning Doppler Light Detection and Ranging (lidar) data were collected from October 21 to November 2 and from November 11 to November 30. The instrument transmits coherent laser pulses at a 2.022 μm wavelength and is designed to accurately measure the radial velocity of light-scattering targets (primarily aerosols) along the beam path by estimating the Doppler frequency shift between transmitted and returned pulses. In addition to radial velocity, the instrument also records wideband signal to noise ratio and range-corrected backscatter intensity. The pulse repetition frequency (PRF) is 200 Hz, with a pulse-to-pulse frequency stability of approximately 1 MHz (Wulfmeyer et al. 2000). Each range gate was sampled 100 times to create the 2 Hz data set. The laser pulse width of 200 ns allows for a range gate spacing of 30 m for independent velocity measurements,

and the diffraction-limited transverse resolution is 60 µrad (<1 m arc length). The data were collected

to a maximum range of 8.3 km, and backscattered signal intensities were adequate for detection out to

6 to 8 km range in most of boundary layer scans observed. Very near field data is unusable because of

internal scattering within the lidar optical system, constraining the minimum range of the data to 180

m (Tucker et al. 2008).

When operating with ample backscattered signal intensity, the HDRL radial velocity has been

demonstrated to have better than 10 cm s^{-1} precision, though the precision is reduced to 30 cm s^{-1} at

lower signal intensity (Rye and Hardesty 1993). The Nyquist velocity (±25m s^{-1}) is constrained by the

system's sampling bandwidth--50 MHz, in the 75-125 MHz Doppler frequency range (Grund et al.

2000). The lidar's Nyquist velocity suffices for unambiguous measurement of the 15-20 m s^{-1}

maximum boundary layer winds measured by the surface meteorology tower and rawinsondes during

VOCALS-REx. Because aerosol particles have a negligible fall velocities compared to atmospheric

motions, the measured velocities outside of clouds and regions of precipitation are assumed to be

equivalent to the radial component of the wind. The high spatial, temporal, and velocity resolution

make HDRL data ideal for imaging turbulent motions and fine structure of mesoscale features below

and between boundary layer clouds, where aerosol scatterers are generally abundant and signal

attenuation due to clouds and drizzle infrequent.

ii. Technique for Measuring Radial Velocity and Signal to Noise Ratio

It should be noted that the HDRL differs from Doppler Radar in that it derives radial

velocities from independent sample volumes, rather than by comparing successive samples of

identical sample volumes over time. This is because the decorrelation time of the atmosphere at 2 µm

is a few microseconds, much briefer than for microwave radiation (Gossard & Strauch 1983). The

device uses a step-stare scan strategy to sample 100 independent pulse returns focused near the center

of each range gate. The radial motion of scatterers within the scattering volume generates Doppler

frequency shifts in the return laser pulse, which the instrument measures by mixing the received

signal with a reproduction of the transmitted oscillator output to create a spectrum of beat frequencies

corresponding to the Doppler phase shift. The detector signal is simultaneously mixed with the

oscillator output that has been phase shifted by 90° (quadrature), because the difference in phase

between the in-phase and quadrature beat frequencies indicates the sign of the velocity. An averaging

estimator is applied to the first harmonics of the resulting frequency peaks to derive the 2 Hz data

mean velocity and broadband signal to noise ratio (Grund et al. 2001; Frehlich 2001; Frehlich &

Yadlowsky 1994).

iii.   Volume Coverage Pattern (VCP)

For VOCALS-REx, the lidar was programmed to cycle through zenith stare, plan position

indicator (ppi), and range height indicator (rhi) volume coverage patterns (vcp) approximately every

20 minutes, spending roughly half the time in zenith stare. The zenith stare data is useful for

calculating turbulence statistics, identifying vertical motions, and locating cloud or virga directly over

the ship. The ppi and rhi vcps together provide detailed images of the three dimensional fine structure

of the boundary layer and mesoscale circulation features within 8.3 km of the ship. In addition, the

ppi and rhi scans obtain data below 180 meter height, the minimum range of the zenith stare. Rhi

scans were conducted at right angles to one another but with otherwise variable azimuth headings.

Generally, one rhi scan spanned $0\text{-}25^0$ in elevation angle over ~30 seconds. One or two 1^0 elevation

ppi scans (covering 0^0 - 360^0 azimuths in ~3 minutes) were usually performed every vcp cycle.

Additional ppi scans were conducted at higher elevation angles (4^0 - 25^0) to capture the mean wind

profile in a manner suitable for Velocity-Azimuth Display (VAD) analysis (Browning & Wexler

1968). If one neglects Earth's curvature, range gate heights in a 1^0 elevation angle ppi increase

linearly as a function of range up to ~150 meters altitude at maximum range.

iv.   Motion Correction and Stabilization

A GPS-based motion compensation system enabled active pointing stabilization and removal

of the ship's mean velocity in three dimensions from velocity measurements along the lidar's line-of-

sight. This system provides better than 0.5^0 beam direction precision in heavy seas (Hill et al. 2008).

To facilitate comparison with other data sources, each range gate was logged in world-fixed spherical

coordinates. Following standard practice, azimuth angles span clockwise from true north and

elevation angles extend up from the plane tangential to the Earth's surface at the location of the ship.

v.   Additional Constraints on HRDL Backscatter Detection

The hard limit of the lidar's maximum range (10.8 km) is determined by the system's

sampling bandwidth. However, in practice the maximum effective scan range is limited by instrument

sensitivity and signal energy, whereby the intensity of light scattered from more distant targets is

insufficient to overcome signal dissipation along the beam path. The laser's maximum beam strength

is low (~2 mJ), and at the farther range gates the receiver often operates near its minimum detection

threshold. Received power from the 2 µm wavelength lidar pulses is subject to a number of well-

constrained range-dependent effects—including atmospheric transmissivity, beam focus and Gaussian

diffraction, and the inverse-squared law of light propagation. The lidar beam was focused at 1 km

range for this data set, and beyond this range the net effect of these factors is to reduce signal

intensity along the integrated path of the beam. A range correction function which accounts for these

combined effects was applied to the broadband signal to noise ratio to create the backscatter intensity

data. The backscatter intensity data is therefore useful for identifying gradients in backscattered signal

intensity within portions of the scan volume where the received signal intensity meets or exceeds the lidar's minimum detectible threshold.

Additional path integrated constraints on HDRL signal intensity result when the lidar pulse encounters aerosols and hydrometeors in a turbulent environment. Signal attenuation due to absorption and scattering results in significant signal loss, especially in regions of clouds and precipitation. Because lidar pulses have a short wavelength, an additional concern results from variations in the path integrated strength of atmospheric turbulence. Turbulent motions along the beam path cause inhomogeneity in the refractive index of the atmosphere, a phenomenon known as refractive turbulence. Refractive turbulence causes both angular displacement and phase changes in the constituent wavefronts of the lidar pulse, leading to constructive and destructive interference and fluctuations in signal intensity (i.e. "twinkling") at both the target and the receiver. In more extreme cases, refractive turbulence may also cause the beam to partially overshoot the receiver. Coherent lidars do not directly detect and count received photons. Rather, the received signal is composed of spatially coherent "speckles" (Frehlich & Yadlowsky 1994). These speckles are in turn composed of in-phase, constructively interfering photons that can be resolved both temporally and spatially. Speckles are either detected or not, such that the signal to noise ratio for a single speckle is at most 1, regardless of how many photons combined to produce them. Because refractive turbulence decreases the spatial and temporal coherence of the returned pulse, signal intensity in regions of high refractive turbulence can be reduced by up to ~10 dB, with smaller variations between pulse repetitions (Grund et al. 2001). Calibration was not conducted to correct for refractive turbulence or attenuation in the VOCAL-REx lidar. As a result, backscatter intensity data should not be viewed as an absolute measurement. However, qualitative examinations of backscatter intensity gradients over limited time frames are nonetheless useful for our analysis (Tucker et al. 2008).

vi.   Lidar Backscatter Coefficient

The volumetric backscatter coefficient, β, is a measure of the brightness of the collection scatterers distributed through a lidar sample volume independent of range and beam intensity. Absent attenuation, refractive turbulence, and other path-dependent atmospheric effects described above, differences in backscatter intensity between range gates are primarily determined by changes in the backscatter coefficient. The backscatter coefficient is a function of the single particle scattering cross-section of each particle, Q_{sca}, and particle sizes integrated over their size distribution, $Nf(D)$ (Intrieri et al. 1993):

$$\beta = \int_0^\infty \pi \left(\frac{D}{2}\right)^2 Q_{sca}(\alpha, n) Nf(D) dD \tag{2.1}$$

$Q_{sca}(\alpha, n)$ parameterizes a host of mostly geometrical and physicochemical factors that affect the scattering efficiency of individual particles—such as the resonance behavior of Mie scattering as a function of the wavelength to particle size ratio, particle shape, the angle of incident light, and optical properties of the constituent materials. The principle determinants of β however are the combined effects of particle diameter, *D*, and number, *N*. In accordance with Mie theory, the backscattered energy emanating from each range gate tends to be dominated by particles with diameters approximating the wavelength of the laser. The lidar primarily detects particles whose sizes fall in the Mie scattering regime ($D \approx \lambda$). The D^2 dependence of β therefore enhances the size effect relative to the first order concentration effect. However, because of the resonance behavior of Mie scatterers, the relationship between the size of a particle and its backscatter coefficient is not linear. The size effect is less pronounced than the size effect on radar reflectivity (D^6). This is because the longer wavelength of radar pulses are designed to detect Rayleigh scattering from hydrometeors, which are much smaller than the transmitted wavelength ($D < \lambda/6$).

An important effect on aerosol size distributions within the marine boundary layer aerosol is deliquescence in high relative humidity (RH) environments. Deliquescence is the process by which a substance absorbs moisture from the atmosphere until it dissolves in the absorbed water and forms a solution. Hygroscopic aerosols are formed from substances that have an electrostatic affinity to water molecule and therefore deliquesce readily. The majority of the aerosols observed in the SEP boundary layer are hygroscopic—i.e. sulfate, sea salt, and nitrates (Shank et al. 2011; Allen et al. 2011)—and deliquescence in moist environments is a prominent aerosol growth mechanism. The effects of RH on aerosol size distributions and backscatter intensity are nonlinear and should occur throughout the observed RH range of 50-100% (Tang 1996). Large changes in RH associated with adiabatic lifting or advection can create backscatter intensity gradients of up to 10 dB in a subsaturated environment, with the largest effects observed between 90% and 100% relative humidity (Tang et al. 1997; Wulfmeyer & Feingold 2000). Inversely, because ultra clean boundary layer conditions were observed during VOCALS-REx (Kleinman et al. 2011;Wood 2011), reduced particle sizes in low relative humidity environments may exacerbate problems with scan volume coverage due to sub-threshold backscatter signal intensity. Nonetheless, adequate lidar signal fidelity has been achieved within relatively clean environments (aerosol number <100 cm^{-3}) that have aerosol size distribution modes below 0.3 μm (Tucker et al. 2008).

vii. Lidar Data Format and Visualization Method

Lidar netcdf data was provided by Alan Brewer at NOAA ESRL in separate hourly time series for each vcp, yielding ~2,200 netcdf files. In order to separate the rhi and ppi scan volumes embedded within each time series, we first binned the azimuth (rhi) and elevation (ppi) angle logged for each scan range. The rhi azimuth angle bin spacing was 5°, whereas the elevation angle bins for the ppis were placed every 3° from 0° - 12° and every 6° from 12° - 30°. If 15 seconds of consecutive rhi data fell within a single azimuth bin, these data points were stored as a separate scan. Similarly, if

30 seconds of ppi data fell within an elevation bin, a separate scan was stored. The resulting arrays were converted from spherical to Cartesian coordinates. PPI elevation angle and rhi azimuth angle were reduced to a single scalar for each scan, so that the resulting data could be more readily viewed within a two dimensional grid. Each scan range within 10-minute segments of zenith stare data was reassigned to the nearest half second.

B. C-Band Precipitation Radar

A scanning C-band radar was used to detect light precipitation falling from shallow clouds in the region surrounding the ship. The radar transmits at a 5 cm wavelength and is therefore sensitive to drizzle and heavier precipitation but not cloud droplets (Ryan et al. 2002). PPI scan volumes were completed every 3 minutes, yielding over 16,000 files. The maximum range of the C-band radar data was 60 km. Reflectivity data was quality controlled using the methods described in Comstock et al. (2004) and interpolated to a 250 m horizontal Cartesian grid with 500 m vertical layers. The reflectivities presented here are the column maximum values for each horizontal grid box. Areal average and conditional average rain rates were derived using a modification of the Z-R relationship from Comstock et al. (2004):

$$Z \ = \ 25R^{1.3} \tag{2.2}$$

where Z is radar reflectivity in $mm^6 m^{-3}$ and R is rain rate in $mmhr^{-1}$. A full discussion of the method used to derive rain rates for the cruise is presented in Burleyson et al. (2013). The rain rates used in this study are the column maximum values for each horizontal grid box.

C. Surface Meteorological Variables

Wind, temperature, pressure, and humidity were measured at 1 Hz on the forward mast of the ship following the method of Fairall et al. (1997) and are available as a one minute average data set.

A complete description of this VOCALS-REx data set is provided in de Szoeke et al. (2010). An aspirated and shielded Vaisala HMP-235 or HMT-335 thermometer/hygrometer measured temperature and humidity. The Vaisala sensors have an accuracy of 0.1°C for temperature and 2% for relative humidity. Atmospheric pressure at 0.2 hPa accuracy was measured on the deck of the ship in static barometer housing at approximately 7 m above sea level. Ship-relative winds were measured at 1 Hz using the on-board imet sensor. Winds were corrected for ship heading, speed, pitch, roll and yaw to derive the true winds. Wind data were then discrete averaged over 1-minute intervals. The presence of precipitation at the ship deck was detected by an optical scintillation rain gauge. Sea surface temperature was collected by a "sea snake" thermometer floating $\approx$5 cm below the surface. This instrument can detect solar warming but is too deep to be affected by evaporative cooling at the surface.

D. Additional Instruments

The ship's Vaisala lidar ceilometer retrieved cloud base heights every 15 seconds for up to three cloud layers at 15 or 30-m resolution (de Szoeke et al. 2010). Median cloud base height was averaged over 10-minute intervals.

Passive microwave radiometers retrieved column-integrated water vapor and liquid water from brightness temperature measurements at multiple wavelengths. A complete description of the methods used to retrieve integrated cloud liquid water path and water vapor path is provided in de Szoeke et al. (2010).

A Vaisala RS92 rawinsonde was launched from the ship every four hours to collect data on the winds and thermodynamic state in the boundary layer. The instrument measures temperature to an accuracy (reproducibility error) of 0.2^0C, relative humidity to 2% accuracy, and pressure to 0.5 hPa accuracy. Profiles of temperature, pressure, and relative humidity were also used to derive virtual

potential temperature (θ_v) within the boundary layer. For this study, θ_v was calculated without the contribution due to liquid water, as precipitation was rarely observed outside of cloud during sounding launches. Dry Brunt-Väisälä frequency (N^2) was calculated for the subcloud boundary layer by first averaging virtual potential temperature over 100 meter intervals. The dry Brunt-Väisälä frequency of the subcloud layer was calculated from the lowest 100-meter layer to the 100-meter layer just beneath the median cloud base:

$$N^2 = \frac{g}{\overline{\theta_v}} \frac{\Delta \theta_v}{\Delta z} \tag{2.3}$$

where g is 9.81 m s^{-2}, Δz is vertical distance between the centers of the two layers, and $\overline{\theta_v}$ is the average virtual potential temperature from the surface through the layer just beneath the median cloud base.

Aerosol number concentrations were recorded using the instruments and methods described in (Bates et al. 2008). A TSI model 3321 Aerodynamic Particle Sizer (APS) on the RHB was used to measure aerosol concentrations in the 0.8 – 10 μm size range. This device draws air through an optical forward scattering probe and counts aerosols in six bins. Smaller particles (20 – 800 nm) were sorted and counted by a Differential Mobility Particle Sizer (DMSP). The DMSP used was a combination of a Hauke Long and Hauke Short with TSI particle counters—models 3010 and 3025, respectively. A quality controlled time series of aerosol concentrations were provided by Simon de Szoeke at Oregon State University as 10-minute averages in 5 size bins: .02 – 0.1, 0.1 – 0.3, 0.3 – 1.0, and >1.0 μm. For this analysis, we present aerosol concentrations in three bins corresponding to the Aitken (20 – 100 nm), Accumulation (0.1 – 1 μm), and Coarse (>1.0 μm) modes.

II. Feature Identification and Classification of Density Currents, Cold Pools, and Temperature Spikes from *in situ* Ship Data

A. Initial Processing of Ship Time Series

Our initial step is to calculate air density from the one minute ship-level temperature, relative humidity, and pressure data. Virtual temperature is calculated first and then combined with air pressure to determine air density using the equation of state. During several days of the cruise, unphysically low pressure values were recorded. These data are removed from the ship time series prior to analysis. The ~30 day data window used to identify temperature and density anomalies spanned from 00:00:00 GMT on 24 October 2008 to 06:00:00 GMT on 3 November 2008 and from 00:00:00 GMT on 11 November 2008 to 00:00:00 GMT on 30 November 2008. Aerosol concentrations are upsampled to 1 min to match the sampling interval of the other ship meteorological data.

During VOCAS-REx the RHB's course and heading varied over time and was comparable in magnitude to the winds observed (4-12 m s^{-1}). In order to compare the shape and extent of density currents, temperature spikes, cold pools, and their features more directly and generically, we then calculate the ship-relative displacement. The ship-relative displacement vector is calculated discretely at each point in the time series by multiplying the sum of ship-relative wind speed by the 60 s time interval of the data. Next, time series variables are linearly interpolated along a regularly spaced ship-relative wind displacement vector of 100 m spacing. One minute of data translates to between 200 and 700 m of ship relative displacement for ~84% of the series, and ~1.1% of data points are downsampled at 100 m spacing. We also calculate the 3 km and 100 km simple unweighted moving window average series of temperature and density to smooth high frequency noise and isolate lower frequency background variations.

B. Criteria for Identifying Density Current Feature Points

The criterion used to identify a density current front passing over the ship is a 1 g m^{-3} increase in the 3.5 km moving window average of density, $\bar{\rho}$:

$$\frac{\Delta \bar{\rho}_{front}}{\Delta x} \geq 1 \text{ g m}^{-3} (3.5 \text{ km})^{-1} \tag{2.4}$$

The criterion corresponds to a change in density of ~0.083%, which is equivalent to a cold pool of intensity of ~0.24^0C at T=290 K assuming constant specific humidity (Terai 2011). Any contiguous data points with where $\bar{\rho}$ meets this criterion are combined into a single density current front. The start time of the density current can be offset from the start of the density increase by up to three minutes. This is because the $\bar{\rho}$ series tends to diverge from the 100 m data before the start of the density current front. We therefore adjusted the start times of each density current by eye.

Density currents often display a signature shape in the ship data series of density. The density current front is followed by a plateau of roughly peak density. This region we refer to as the density current "core." After the density core has passed over the ship, density steadily decreases. This region we refer to as the density current "tail." The density current core is defined as the set of data points that lie between the last data point within the density current front identified by Eq. 2.4 (i.e. the end of the density current front) and the end of the core. The end of the core is found where the slope of the 3.5 km moving window average density value, $\bar{\rho}$, first becomes negative *after the density current front*—that is,

$$\frac{\Delta \bar{\rho}_{core\ end}}{\Delta x} < 0 \text{ g m}^{-3} (3.5 \text{ km})^{-1} \tag{2.5}$$

The density current tail is defined as the region between the end of the density current core and the end of the density current tail. The end of the density current tail is located where the slope of the 3 km moving window average density value, $\bar{\rho}$, first becomes positive *after the density current core*:

$$\frac{\Delta\bar{\rho}_{tail\ end}}{\Delta x} > 0 \text{ g m}^{-3} (3.5 \text{ km})^{-1} \tag{2.6}$$

The complete set of criteria for finding density current feature points--including front, core end, and tail end—are demonstrated on an idealized short density series in Fig. 2.1. Note that density currents are allowed to vary in size, and the distances shown on the abscissa of Fig. 2.1 are only intended to demonstrate the density current front criterion.

C. Criteria for Identifying Temperature Spike Feature Points

The onset of a temperature spike is identified by a 0.24 K increase in the 3.5 km moving window average of temperature, $\bar{T}$:

$$\frac{\Delta\bar{T}_{onset}}{\Delta x} \geq 0.24 \text{ K} (3.5 \text{ km})^{-1} \tag{2.7}$$

Any contiguous data points that meet the temperature spike slope criteria are combined into a single temperature spike onset. The next step is to find the end of the temperature spike. The end of the temperature spike is the first location in the series after the temperature spike onset where one of three criteria is satisfied:

T drops below the 100 km running average temperature, T^*; *or,* (2.8.1)

the start of another temperature spike is reached, applying condition (2.7); *or,* (2.8.2)

the start of a "reverse" temperature spike is found by applying condition (2.7) to the reversed order

temperature series.   (2.8.3)

The third feature point identified within a temperature spike is the point between the start and end

of the temperature spike where temperature is at maximum value, TSmax. Temperature spikes are

required to have a maximum unfiltered 100 m temperature value (T_{TSmax}) that exceeds the 100 km

running average temperature, T^*, by at least 2 standard deviations above the mean exceedance from

T^* for the entire data set:

$$(T - T^*)_{TSmax} \geq 2\sigma_{(T - T^*)}$$ (2.9)

where $2\sigma_{(T - T^*)} \approx 0.3$ K. Points lying between TSmax and the end of the temperature spike are in

the "rebound" of the temperature spike. The criteria for finding all temperature spike feature points—

including onset, max value, and rebound end—are demonstrated on an idealized short temperature

series in Fig. 2.2. Note that temperature spikes are allowed vary in size and overall shape, and the

distances shown on the abscissa of Fig. 2.2 are only necessary to demonstrate the onset criterion (2.7)

and options 1 and 3 of the rebound end criteria (2.8.1 and 2.8.3).

D. Criteria for Identifying Cold Pool Edges and Reverse Cold Pool Edges

The criteria for identifying cold pool edges is adapted from those described in Terai (2011), who

used VOCALS-REx aircraft data to identify colds pools at ~150 m altitude using potential

temperature. Their method required drops in temperature to be observed in the unfiltered data over

four successive intervals. We applied their criteria over 900 meter long ship-relative displacement

intervals. A point in the ship series, X, with temperature T, is identified as being within a cold pool

edge if it meets all of the following:

T(X) - T(X - 900 m) ≤ -0.06 K, and

T(X) - T(X - 1800 m) ≤ -0.12 K,

T(X) - T(X + 900 m) ≥ 0.06 K,

T(X) - T(X + 1800 m) ≥ 0.12 K   (2.10)

Consistent with the method presented in Terai (2011), reverse cold pools are also identified by

applying (2.10) over the ship series that has been reversed in order. Reverse cold pools are therefore

identified by temperature *increases* of the same magnitude and progression as cold pool temperature

decreases. In other words:

T(X) - T(X - 900 m) ≤ 0.06 K, and

T(X) - T(X - 1800 m) ≤ 0.12 K,

T(X) - T(X + 900 m) ≥ -0.06 K,

T(X) - T(X + 1800 m) ≥ -0.12 K   (2.11)

The criteria for finding cold pools and reverse cold pools are demonstrated on an idealized

short temperature series in Fig. 2.3. Note that our use of the term cold pool "edge" will henceforth

differ from how it was used by Terai (2011) to make the term more consistent with a density current

"front." Terai (2011) defines the "cold pool edge" as the single point (X) that meets either 2.10 or

2.11, whereas we define the "cold pool edge" ("reverse cold pool edge") as all of the four points

adjacent to Terai's "edge." As with density currents and temperature spikes, any contiguous points

that meet 2.10 (2.11) are combined with each other and with each of the unique adjacent data points to form a single cold pool edge (reverse cold pool edge).

Examples of density currents, cold pools, reverse cold pools, and temperature spikes are provided to demonstrate the performance of each within the data series. Fig. 2.4 c,d depicts the signature of density and temperature of two consecutive Doppler lidar confirmed density currents crossing over the ship. The corresponding two cold pools and one reverse cold pool are shown in Fig. 2.4 a,b. Fig. 2.5 shows an example of an isolated temperature spike in the density and temperature data series.

E. Removing Temperature Anomalies from Ship Exhaust Contamination

Ship exhaust traveling forward across the instrument mast at the bow of the ship was found to contaminate the ship temperature data on a number of occasions throughout the data set. The ship exhaust caused sudden increases in temperature. For this reason, we disregard any temperature spikes or reverse cold pools that are identified when the ship-relative wind direction was either more than 60^0 off the bow of the ship or the ship-relative wind speed was less than 3 m s^{-1} (Bates et al. 2008). We also disregard any density currents or cold pool edges that are identified as the ship exhaust resumed blowing away from the ship's bow and the temperature sharply decreased.

F. Classification of Density Currents, Cold Pools, and Temperature Spikes

Density currents, temperature spikes, and cold pools often overlap with one another. It is expected that sharp drops in temperature would be identified as both cold pools and density currents in many cases. However, temperature spikes also are identified adjacent to density currents. An example of a phenomenon that is flagged as a temperature spike embedded in a series of density currents/cold pools is shown in Fig. 2.6. In this case the temperature spike starting at t=0 is bounded

26

on both sides by a density current. Although it clearly is a high temperature anomaly (Fig. 2.6f), the fact that it is bounded on both sides by density currents makes it nonetheless ambiguous. It could simply result from the temperature increase at the tail of the previous density current and not from a separate physical process. This is a problem for temperature spike identification particularly, because we do not know what they are physically. We therefore have no way of corroborating temperature spikes in the same way that we can verify density currents via lidar. If, on the other hand, the temperature spike does in fact represent a physical process, the intensity of the density current front starting at x=10 km is augmented because its front overlaps with the temperature spike's rebound. We therefore feel it necessary to identify these hybrid phenomena, so that we can track their influence on the bulk statistics presented in Chapter 5.

The classification scheme used for temperature spikes is summarized in Fig. 2.7. Temperature spikes are grouped based on whether they overlap on one side, both sides, or neither side by a density current. Temperature spikes that do not overlap at any point with a density current are classified as "isolated" temperature spikes (see Fig. 2.5). Temperature spikes whose onset or rebound overlaps with a density current, but not both, are classified as "simple hybrid" temperature spikes (example not shown). Temperature spikes whose onset and rebound both overlap with a density current are classified as "bounded" temperature spikes (Fig. 2.6). Any simple hybrid or bounded temperature spike that overlaps with a density current tail along its onset is also noted in the analysis as a temperature spike with "onset overlap."

Fig. 2.8 provides an overview of the classification scheme for density currents. Density currents are grouped in a manner very similar to the classification scheme used for temperature spikes—i.e. according to whether their front, their tail, both sides, or neither side overlap with a temperature spike. Because we have cross-referenced the ship and lidar data, we are confident that the

identified density currents represent a real physical process. In our bulk analysis, we therefore have tracked only cases where the intensity of the density current front may be augmented by a previous temperature spike. Any density current whose front overlaps with a temperature spike rebound is noted in the analysis as a temperature spike with "front overlap." Fig. 2.6 shows an example of a simple hybrid density current with front overlap starting at x=10.

The classification scheme for cold pools is summarized in Fig. 2.9. Any cold pool edge that overlaps a density current is designated as "density current match." Cold pool edges that overlap with a temperature spike rebound are classified as a cold pool edge with front overlap. Any cold pool edge that does not overlap with a density current is assumed to be an isolated cold pool unless it overlaps a temperature spike, at which point it is categorized as a cold pool with front overlap. Note that a density current that overlaps one or more cold pools is also classified as a "cold pool match" using the above scheme. Reverse cold pool edges are classified only as to whether or not they overlap a density current or a temperature spike.
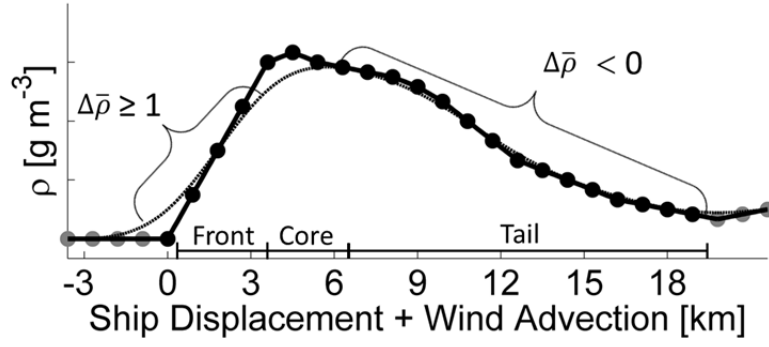
Fig. 2.1: Graphical summary of the criteria used to find density current front start, front end, core end, and tail end feature points. Data points spaced at 900 meter intervals are shown in circles. Black circles represent data points identified by the algorithm as either the front zone, core zone, or tail zone of the density current. The black line shows the idealized 100 meter density data. The black dotted line shows the 3.5 km moving average ($\bar{\rho}$) of the density data.
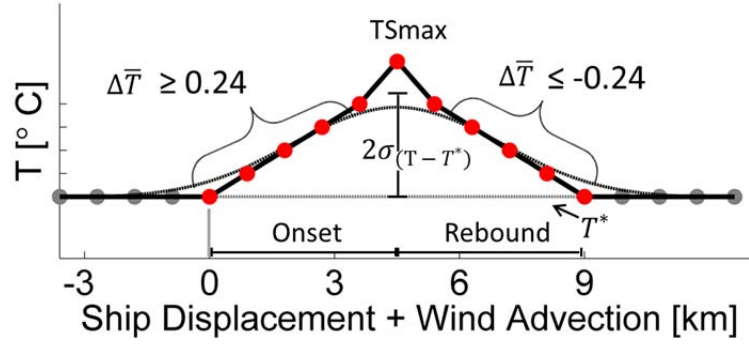
Fig. 2.2: Graphical summary of the criteria used to find temperature spike onset start, max, and rebound end. Data points spaced at 900 meter intervals are shown in circles. Red circles represent data points identified by the algorithm as either the onset or rebound of the temperature spike. The black line shows the idealized 100 meter temperature data. The black dotted line shows the 3.5 km moving average ($\bar{T}$) of the temperature data. The gray dotted line shows the 100 km moving average (T^*) of the temperature data. The maximum temperature value within the temperature spike is required to exceed T^* by more than two standard deviations of the mean exceedance for the data set ($2\sigma_{(T - T^*)}$).
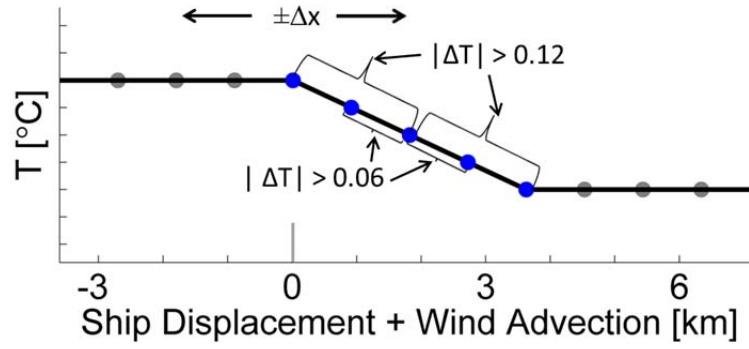
Fig. 2.3: Graphical summary of the criteria used to identify cold pool edges and reverse cold pool edges. This method is described in Terai (2011). Cold pools edges are found by evaluating the temperature data series from left to right in this diagram. Reverse cold pool edges are found by reversing the order of the data series and applying the same criteria. Data points spaced at 900 meter intervals are shown in circles. Blue circles represent data points identified by the algorithm as a cold pool edge. The black line shows the idealized 100 meter temperature data.
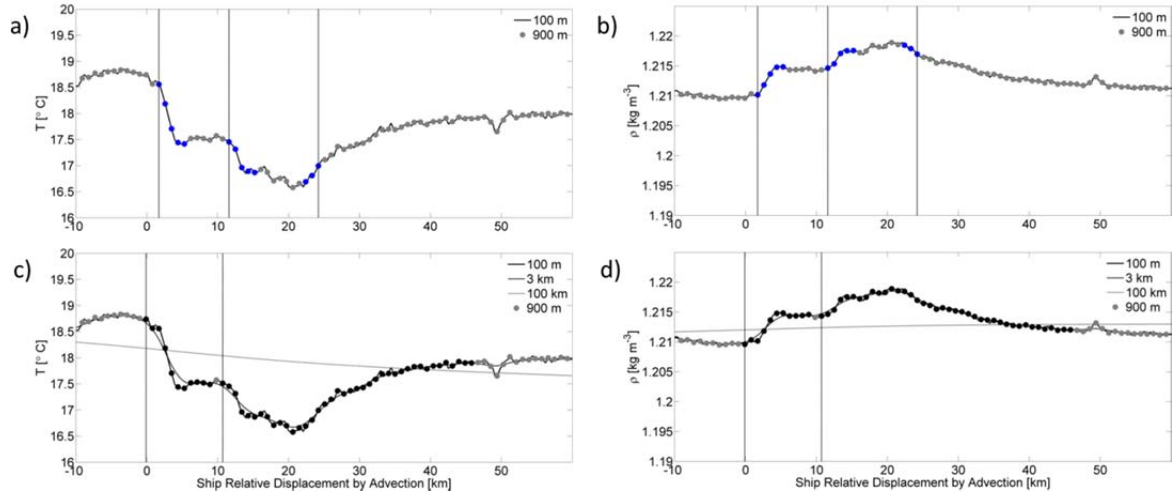
Fig. 2.4 a-d: Example of a phenomenon identified in the ship data series by both the density current and the cold pool algorithm (i.e. density current/cold pool 'match'). The density data corresponding to this feature are shown on the left (a,c) and the temperature data for the same segment of the data series are shown on the right (b,d). The data points identified by the cold pool algorithm (a,b) are shown at 900 meter intervals shown in blue. Data points identified by the density current algorithm (c,d) at 900 meter intervals are shown in black. Vertical gray lines indicate the start of a density current (c,d), cold pool edge (a,b—at x=2 and 12), or reverse cold pool edge (a,b—at x=24). The origin of the x axis is set to the start of the first density current front identified in the series. The 100 meter data set (light gray line), the 3 km moving window average (gray), and the 100 km moving window average (black) are also shown.
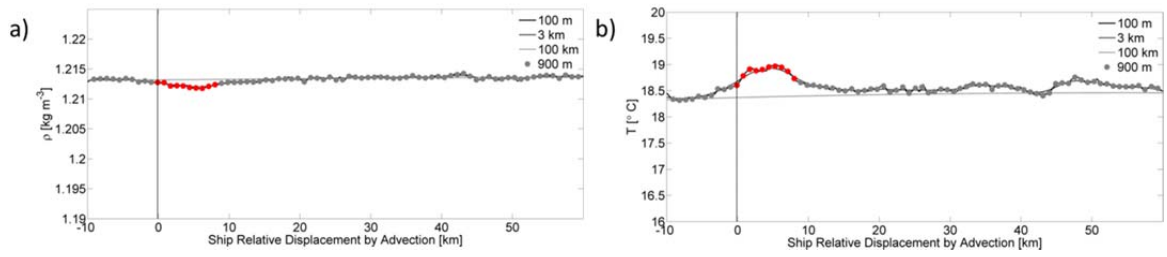
Fig. 2.5 a,b: Example of an isolated temperature spike. The data points identified by the temperature spike algorithm are shown at 900 meter intervals shown in red. The origin of the x axis is set to the start of the temperature spike identified in the series. Vertical gray lines indicate the start of a temperature spike. The density data corresponding to this feature are shown on the left (a) and the temperature data for the same segment of the data series are shown on the right (b). The 100 meter data set (light gray line), the 3 km moving window average (gray), and the 100 km moving window average (black) are also shown.
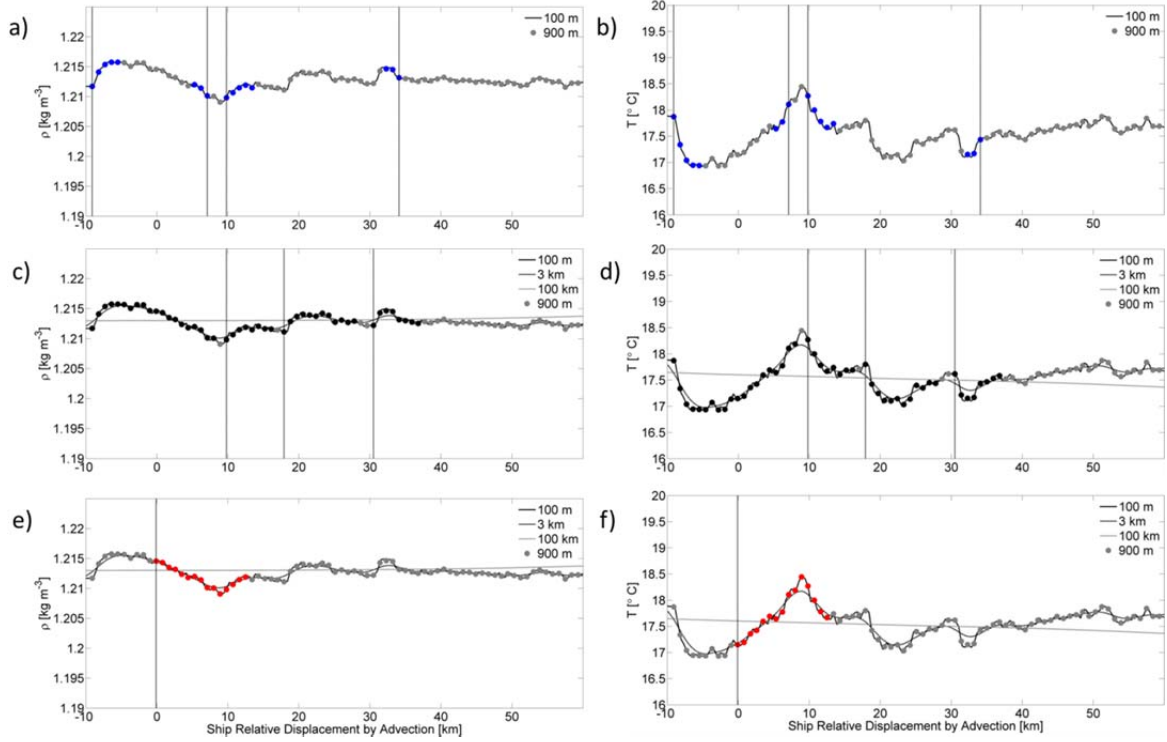
Fig. 2.6 a-f: An example of a phenomenon identified by all three algorithms, starting at x=0. The density data corresponding to the phenomenon is shown on the left (a,c,e) and the temperature data for the same segment of the data series are shown on the right (b,d,f). The data points identified by the cold pool (a,b—blue), density current (c,d—black), and temperature spike (e,f—red) algorithms are shown at 900 meter intervals. The origin of the x axis is set to the start of the temperature spike identified in the series. Vertical gray lines indicate the start of a cold pool or reverse cold pool edge (a,b), density current (c,d), or temperature spike (e,f). The 100 meter data set (light gray line), the 3 km moving window average (gray), and the 100 km moving window average (black) are also shown.

34
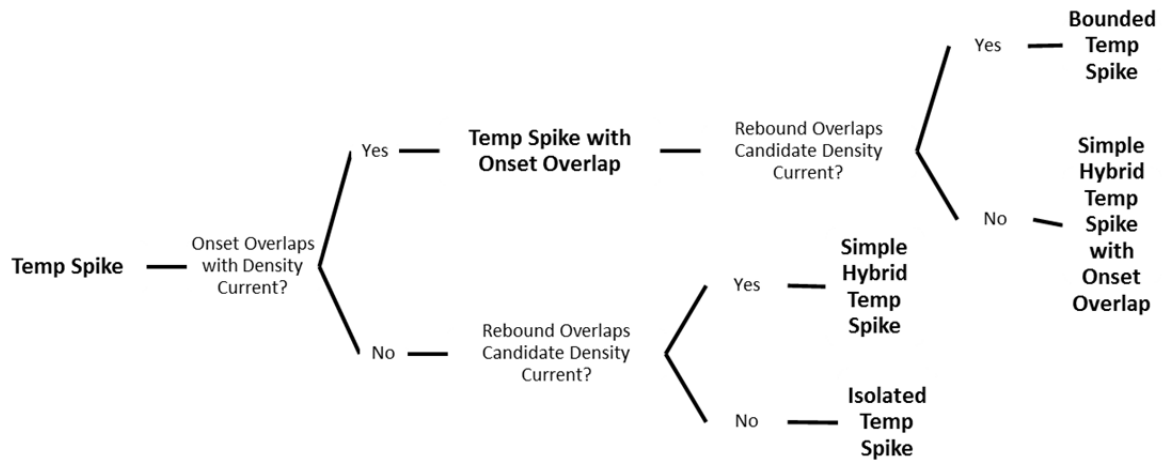
Fig. 2.7: Summary of the criteria used to classify a temperature spike based on its overlap in the data series with one or more density current features.
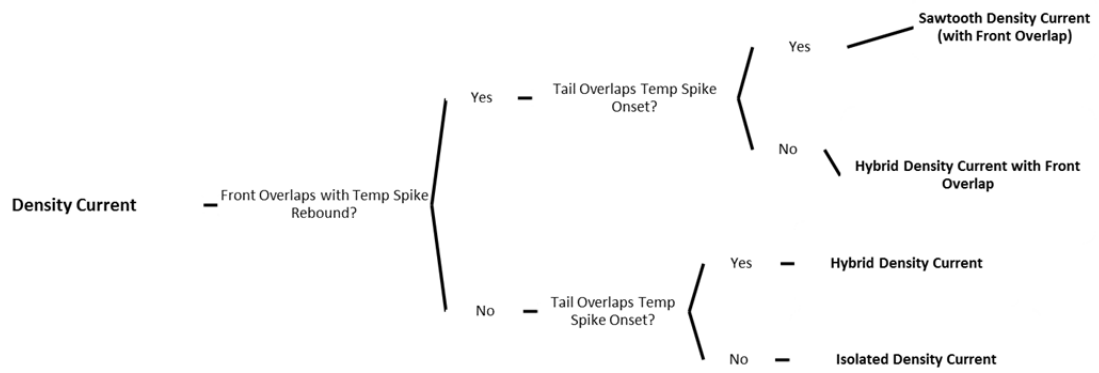
Fig. 2.8: Summary of the criteria used to classify a density current based on its overlap in the data series with one or more temperature spike features.

Density Current Match*

Yes

Candidate Cold Pool ——— Overlaps Density Current?

No ——— Overlaps a temp spike rebound?

Yes ——— **Cold Pool with Front Overlap**

No ——— **Isolated Cold Pool**
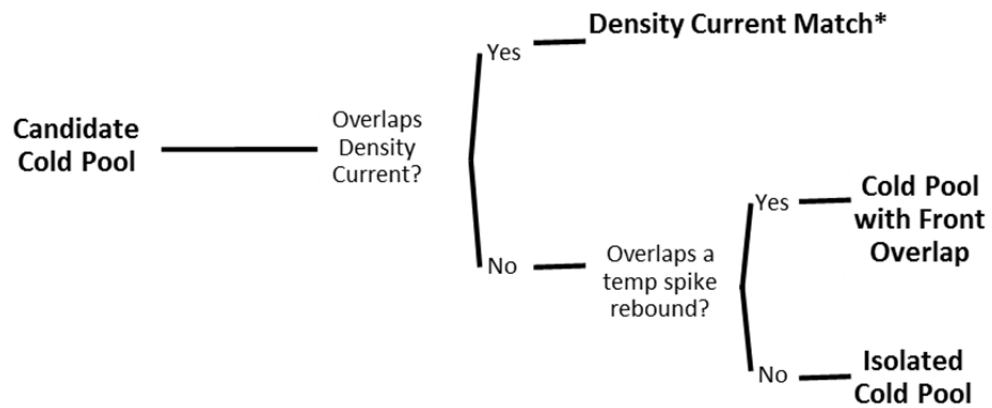
* The identified matching density currents are called "Cold Pool Matches"

Fig. 2.9: Summary of the criteria used to classify a cold pool based on its overlap in the data series with a density current front or a temperature spike rebound.

<center>CHAPTER 3</center>

Detailed Examination of Density Current Cases

Of the 76 density currents identified in the RHB ship meteorological data, three were selected to contextualize, exemplify and detail the structure of these kinematic features, their evolution over time, and their orientation relative to the precipitation field. All three occurred near or within an open cell region with drizzle present in the radar domain. These exemplars however differ in the configuration of existing and developing precipitation cells around the ship. In the first case, a density current crossed the ship at 1617 GMT on 26 October 2008, but only relatively weak and diminishing precipitation was observed at close range. The air behind the front was characterized by a 20% increase in relative humidity, and this case was dubbed a "humidity front." The second event, a drizzle outflow that crossed the ship at 556GMT on 27 October 2008, has been previously documented by Feingold et al. (2010) and serves as the reference case for a drizzle-induced density current. The final event presented in this section took place around 827 GMT on 26 October 2008. In this case, a density current appeared to collide with another that had passed over the ship fifty minutes earlier. This third case also shows evidence of subsequent drizzle cell initiation along the line of convergence between the colliding density currents.

For the figures depicted in this chapter, data collection times are expressed as an offset from the time (t_0) at which the density current front of interest passed over the ship. In the composite lidar figures (Figs. 3.1, 3.8; 3.14), dotted lines demarcate any depicted scans that were taken at approximately the same time as the 1^0 elevation angle ppi scans contained within each group. Additionally, the azimuth angle of lidar rhi scans are indicated by radially-oriented green line segments superimposed on the corresponding ppi scan within a group. A mean wind correction was applied to lidar ppi and rhi radial velocity data for all three cases to better display the velocity

<center>38</center>

perturbations associated with density currents. The mean wind speed and direction used for the mean wind correction was calculated from the 8-hour moving window average of the orthogonal wind components measured on the ship at the time of each scan. Data collected when signal-to-noise ratio (SNR) was below -10 dB were converted to missing values because instrument noise was found to significantly degrade the accuracy of radial velocity estimates below this value. PPI scans do not cover the full set of azimuth angles from 0^0 to 360^0 because a wedge of $\sim25^0$ is blocked by the bridge of the ship located behind the lidar. Similarly, there are intermittent gaps in both the ppi and rhi scan volume coverage caused by objects on or near the ship.

I. Humidity Front (1617 GMT 26 October 2008)

A. Evolution of Kinematic Features

Lidar ppi, rhi, and zenith scare scans shown in Fig. 3.1 capture the progression of an air mass with increased aerosol backscatter intensity over the period of 1607-1643 GMT (t_0 = 1618 GMT). The front first appears (t_0 – 10 min) as an arc in the southeast quadrant of the 1^0 elevation angle ppi domain. By t_0 + 3 min, the front has crossed the ship, revealing a broad line with lobes and clefts that transects the ppi domain. The ship track during this period was towards the southwest, nearly parallel to the front, at ~5 m s^{-1}. Radial velocities behind the front increase by ~4 m/s and shifted $\sim10^0$ to the south. The gust weakens from 4 m s^{-1} to 1-3 m s^{-1} in the southeast quadrant of the lidar domain by t_0 + 23 min.

RHI scans shown in Fig. 3.1 were taken 7-8 minutes after the front passed the ship. They were collected roughly perpendicular to the front at an azimuth angle of 339^0, providing vertical cross sections along the axis of the main density current circulation. The density current is visible as a layer of -5-10 dB backscatter intensity ~700 meters deep between the ship and ~4 km range. The two associated mean wind corrected radial velocity rhis reveal a classic density current structure of

densest and fastest main horizontal flow embedded within the deeper zone of increased backscatter. The core region of maximum flow is deepest near its leading edge between 3 and 4 km range, where it forms a ~400 meter deep "head" with a small "nose" jutting out from the leading edge just above the ocean surface. Behind the head at less than 3 km range, the layer of maximum velocity thins to less than 200 meters, and a layer of decreased forward flow characterized by swirls, mottling and unevenness in radial velocity within the scan volume is superposed on the maximum flow. This pattern to the radial velocity signature is caused by velocity couplets, and these coupled are most pronounced within a zone of turbulent flow over top of the main density current flow. The turbulence observed in this layer can be explained by the fact that there is ~6 m s^{-1} shear between 200 meters and 700 meters. Shear generated turbulence between 200 and 700 meters altitude also explains why the layer of maximum backscatter intensity observed behind the humidity front extends to 700 meters, several hundred meters above the main flow. Shearing instability generates turbulent eddies, and these motions would tend to vertically mix the upper regions of a density current. This mixing transports moisture and aerosol into the layers above the main flow—in this case, the air at these heights is markedly dry and clean in advance of the density current—and additionally cools and moistens parcels lifted in this manner. These processes together serve to increase the size and concentration of aerosol scatterers above the main density current flow. As a result, a zone of increased backscatter extends through the depth of the shear layer and thus encapsulates the main density current flow.

Fig. 3.1 also shows upward-pointing velocity data taken between 1610 and 1620 GMT, before and during the passage of the humidity front at 1618 GMT. A prominent updraft of ~1.5 m s^{-1} reached 700 meters in height in the minute prior to the arrival of the front at the ship. The observed updraft is generally consistent with modeling studies (Xue et al. 2008; Feingold et al. 2010; Wang et al. 2010) as well as observational studies (Jensen et al. 2000; Terai 2011) of the updraft strength at the

leading edge of cold pools beneath marine stratocumulus. In the ~ 5 minutes before this pronounced

updraft, the lidar also detected an increase in turbulent vertical motion in the lower 400 meters of the

boundary layer. This finding suggests that the density current may have generated gravity waves or

other disturbances that propagated ahead of the front and induced vertical motions.

B. Surface Air Mass Properties and Winds

Fig. 3.2 plots time series of RHB surface air density, other meteorological variables and

aerosol concentrations from 1400 GMT to 1800 GMT. During this period, two density current fronts

were identified starting at 1421 GMT and 1618 GMT (t_0) using the method described in the Chapter

2. The stronger of the two density perturbations corresponds to the passage of the humidity front over

the ship (t_0).

The period between 1430 and 1540 GMT leading up to the humidity front was characterized

by a small, gradual decrease in density caused by increasing temperature and coincident drying.

Relative humidity near the surface dipped to ~70% during this period, surprisingly low for 10 m

above the ocean surface. After the front passed the ship, the air became substantially cooler (-1.25^0C)

and moister ($+1.5$ g kg^{-1}) and relative humidity peaked at ~90%. The increase in relative humidity

partially explains the increase in backscatter intensity observed in the lidar domain behind the

humidity front: enhanced hygroscopic growth leads to larger aerosol particles and higher backscatter

intensity. Ship level pressure increased by ~0.5 hPa behind the humidity front, which we expect in a

hydrostatic system. On the backside of the humidity front, ship level wind speed increased by ~3 m/s

and the wind shifted ~10^0 towards the south, which agrees well with the lidar observations from this

time. The increase in winds was more gradual than the change in state variables and began ~15 min

before the arrival of the front. The tail of the density current that produced the humidity front was

punctuated at 1648 GMT by a jump in temperature that corresponded to when the ship was moving

through a tailwind. For this reason, this feature—as well as a similar temperature increase at ~1400 GMT—are very likely caused by the ship exhaust plume blowing across the temperature sensor and are disregarded.

Two notable features emerge from the aerosol concentrations measured at the ship level from 1415-1635 GMT, which includes all times when these data are available for this case. First, Aitken mode particles dominate the number distribution, and accumulation mode aerosols are scarce during this time. Accumulation mode concentrations are between 20 and 35 cm^{-3}, with Aitken mode concentrations approximately 10x greater. This is consistent with other studies of the aerosol number distributions in the vicinity of areas of open cells (Petters et al. 2006; Sharon et al. 2006). Coarse mode aerosols are notably scarcest of all (0.5 – 2 cm^{-3}). Second, the humidity front carries air with a higher aerosol load in all three modes (Aitken +100 cm^{-3}, accumulation +15 cm^{-3}, coarse mode +1 cm^{-3}). Aerosol concentrations in all three size modes roughly follow that of wind speed from 1415-1635 GMT, suggesting that aerosol concentrations may be linked to wind driven sea spray fluxes. This is a somewhat surprising result, because we expect aerosol concentrations to decrease when entering a freshly scavenged drizzle outflow. Over several minutes, however, wind-driven sea spray fluxes would perhaps have had time to fully replenish aerosol concentrations near the surface and remove the signature of aerosol scavenging. We therefore suggest that the higher aerosol concentrations behind the humidity front may simply reflect the processes occurring in an aging drizzle outflow.

C. Boundary Layer Conditions

Fig. 3.3 plots the time-height series of upward-pointing lidar backscatter intensity, which depicts the distribution of hydrometeors, moisture, and aerosol through the depth of the boundary layer directly over the ship. Cloud coverage is broken from 1400-1500 GMT, with subcloud cumulus observed between 600 and 1000 meters altitude at ~1420 GMT. These subcloud cumulus were

associated with the passage of a density current over the ship identified in the ship series (see Fig. 3.2). Over the case period, there is a gradual descent of the stratocumulus deck, whose base is located at ~1350 meters altitude at 1445 GMT and ~1200 meters at 1730 GMT. Moderately intense virga descended to ~700 meters height from 1750 GMT to 1800 GMT, and lighter, sporadic virga was observed 100-800 meters below the cloud base during much of the period. The vertical extent of the moist and aerosol-laden air within the surface mixed layer shallows from 1430-1530 GMT, after which very dry and/or clean air is observed from 180 meters altitude up to the cloud base. A clearly delineated, higher backscatter intensity surface mixed layer of 300-400 meter depth resumes at 1540 GMT. A distinct jump in backscatter intensity is observed below 750 meters at 1618 GMT, corresponding to the increase in updraft velocities observed near and over the humidity front. Afterwards, virga becomes more frequent and intense, and the increase in backscatter intensity throughout the boundary layer suggests gradual moistening and/or increases in aerosol loading in ~500 meters below the base of cloud/virga.

Fig. 3.4 shows temperature, relative humidity, and virtual potential temperature derived from the 1530 GMT rawinsonde data. Relative humidity sampled in the boundary layer prior to the advance of the humidity front was below 75% from the surface up to 1 km, making this among the driest boundary layers sampled during the cruise. Virtual potential temperature indicates a nearly neutral boundary layer, although positive gradients of virtual potential temperature gradients were observed, most notably at 280 and 1000 meters. These very thin potential temperature increases across these layers are 0.5 K or less. Despite their small magnitude, such stability barriers may nonetheless indicate reduced boundary layer coupling (Jones et al. 2011).

Further evidence for reduced coupling in boundary layer environment associated with this case comes from lidar VADs acquired at 20 minutes intervals from 1400 GMT to 1800 GMT. These

profiles are depicted in Fig. 3.5. Wind speeds vary between 2 m s^{-1} and 10 m s^{-1} below the layers of cloud and drizzle depicted in Fig. 3.3 and speed shear of 2-6 m s^{-1} is observed from the surface to 800-1000 meters height. Wind direction ranges from 90^0 to 140^0 in the subcloud layer, with the largest temporal variations within the lower 400 meters of the boundary layer. Looking at the evolution of wind speeds within different layers over time reveals the presence of separated flows. This effect is perhaps best seen by comparing changes in wind speed within the 500-1000 meter layer with those below 300 meters. When wind speeds in the 500-1000 meter layer change in one direction across successive scans, wind speeds in the lowest ~300 meters often change in the opposite direction. For example, between 1405 GMT and 1425 GMT wind speed increases in the lowest 300 meters, while at the same time decrease between 500 meters and 1000 meters. The same pattern is observed between 1725 GMT and 1745 GMT, and so on across several other profiles in the series. Therefore, not only is the boundary layer sheared, but wind perturbations at different heights are often opposite of one another. This is another indication that the boundary layer is composed of distinct layers, but also that the flow perturbations within these layers often countered one another.

In in Fig. 3.5 the highest wind speeds observed below 300 meters were associated with the passage of two density currents over the ship. These density currents crossed the ship starting at 1421 GMT and 1618 GMT (t$_0$), respectively. The VAD profiles associated with the two density currents (~1425, 1445, 1625 and 1645 GMT) show a 3-4 m s^{-1} increase in wind speed in the lower 200-400 meters of the boundary layer. The winds also shifted towards the north by ~30^0 after the first density current passed (1425 GMT) and then shifted back towards the south (1445 GMT). A wind shift of ~10^0 towards the south was consistent observed behind the humidity front (1625 GMT and 1645 GMT). This observation confirms that the layer of maximum forward flow within the density current which produced the humidity front was located below 300 meters, and that it propagated along an

axis slightly to the south of the mean wind (see Fig. 3.1). Additionally, the profiles confirm the presence of significant shear over top of the main flow of the two density currents (~3-5 m s^{-1} between 200 and 800 meters altitude).

D. Relationship to Drizzle and Cloud Fields

The relationship between the humidity front and the surrounding mesoscale precipitation field is difficult to untangle. Fig. 3.6 depicts the sequence of radar images from this time, embedded in the satellite IR images of the cloud field. The lidar 1^0 tilt ppi mean wind corrected radial velocity field is also shown in the vicinity of the ship to a maximum range of 6 km. Upwind of the humidity front, a dissipating drizzle cell of ~10 dBZ intensity approaches the ship from the southeast at ~15 km distance, with an additional dissipating cell of ~25 dBZ intensity farther east at ~25 km. The light virga detected by the upward-pointing lidar following the passage of the humidity front over the ship (Fig. 3.3) may also be corroborated by the ~5 dBZ reflectivities bordering the lidar domain. However, distinguishing such short-range light precipitation from sea clutter is untenable.

The lack of a near-range intense drizzle cell in the radar domain presents difficulties for diagnosing this event as a drizzle outflow. The density current described in this case was relatively intense. It was also quite large, cohesive and persistent. It lasted for ~1 hour while maintaining a remarkably even and temporally consistent horizontal wind field across the 16 km diameter lidar domain for more than 30 minutes. For these reasons, we do not believe that the patchy virga observed in the upward-pointing lidar data could have produced this flow on its own. Because the humidity front advanced from the SSE, it is perhaps most likely that the humidity front was generated by an outflow from the drizzle cell of ~10 dBZ intensity that is located ~15 km to the SSE of the ship in Fig. 3.6 at $t_0 - 10$ min. For ~1.5 hours, this relatively isolated cell traveled through the radar domain before it reached 15 km of the ship. For much of this time the intensity of this drizzle cell exceeded

25 dBZ. An unimpeded, radially propagating drizzle outflow traveling at 4 m s^{-1} could have outrun its source drizzle cell by 15 km over the course of one hour. This would suggest that the humidity front resulted from an outflow from this drizzle cell. However, the radius of curvature of the humidity front appears in Fig. 3.1 to be significantly larger than 15 km. This observation may be explained by considering two aspects of the precipitation field. First, the proposed source drizzle cell was itself ~15 km in diameter at its peak, and exhibited considerable changes in shape and horizontal extent over its lifetime. As a result, outflows propagating from this cell would not be emanating from a single point, but from an irregularly shaped swath whose width exceeds the drizzle cell diameter at any given point along the drizzle cell track. Over the course of the ~1 hour travel time for a density current to be displaced by 15 km from the drizzle cell, the successive outflow pulses produced by the cell would have had time to collide and merge with one another to form a larger frontal zone. Second, the virga observed over the ship after the passage of the humidity front could have replenished the outflow with cool, dense air as the density current passed underneath. The boundary layer in advance of the front was exceptionally dry, making any precipitation falling from the cloud deck likely to rapidly evaporate. In this way, virga could have continuously reinforced the forward flow of the density current behind humidity front. Following this reasoning, the broad curvature of the humidity front may reflect the shape of an extensive patch of virga behind it.

A selected lidar rhi scan captured subcloud cumulus formation as the humidity front crossed through the lidar domain and is shown in Fig. 3.7.This rhi was taken at 249^0 azimuth confirms the formation of a small patch of subcloud cumulus (5-7 km range, 200-700 m altitude) within and above the density current. Additionally, the intense (>20 dB) backscatter above 1 km altitude marks the stratocumulus cloud deck with a small pocket of virga descending from the cloud base at ~3 km

range. The humidity front case was neither associated with extensive cloud formation nor drizzle reaching the surface within the lidar domain.

II. Feingold et al. 2010 (0556 GMT 27 October 2008)

In the following case, we present a phenomenological analysis of an unambiguous drizzle outflow which has been documented previously by Feingold et al. (2010). The authors of that study proposed that open mesoscale cellular convection (MCC) is a manifestation of a weakly stable equilibrium state comprised of oscillating cloudy/precipitating and cloud-free regions. According to their theory, the precipitating regions of open MCCs evolve into cloud-free regions as convection is suppressed by evaporatively-cooled downdrafts and surface divergence (i.e. precipitation outflows). Conversely, precipitation outflows that propagate out into the cloud-free regions and collide with one another are proposed as the generative mechanism for new convection and therefore new cloudy/precipitating regions. In their Fig. 2, they superimpose a c-band radar scan onto a lidar rhi scan, which together depict a colliding outflow boundary in an open cellular region and its close proximity to precipitation. We include the same lidar rhi scan in our analysis and further describe this case in the context of the full lidar data set and other data sources in a manner parallel to the other two cases.

A. Evolution of Kinematic Features

Fig. 3.8 displays selected ppi, rhi, and upward-pointing lidar scans prior to the passage of a moderately large and intense developing drizzle cell over the RHB starting at ~1610 GMT. The ship was very nearly stationary during this case. The lidar 1^0 tilt ppis in Fig. 3.8 show the near-surface prefrontal environment at ~527 GMT, 29 minutes before the arrival of the density current ($t_0 = 556$ GMT). At this time the backscatter intensity field is coarsely uniform, with only fine-scale (<1 km wide) filaments of higher and lower backscatter across most of the domain. The fine-scale streaks in

backscatter intensity also line up with bands of higher and lower mean wind corrected radial velocity that are orientated roughly along the mean wind. An rhi scan of backscatter intensity transecting the southeast of the domain at $t_0 - 30$ min shows a surface mixed layer extending to between 300 and 600 meters altitude and virga descending to 700 meters below the stratocumulus layer, which is located above 1 km. Between these the virga and the surface mixed layer lies a very dry and/or clean subcloud layer.

Nine minutes prior to its crossing over the ship ($t_0 - 9$ min), the outflow boundary of the approaching drizzle cell is visible in the ppis as two flanks of >10 dB backscatter intensity to the east (~4 km range) and the south (~6 km range) of the ship. Nestled in advance of these two flanks, a pocket of drier and/or cleaner air approximately 10 km across and backscatter intensity below -10 dB is also present. The pocket's leading edge appears ragged and cavitied and has passed to the north and west of the ship by this time. Isolated, smaller pockets of very low backscatter intensity 1-3 km in diameter were also detected to the northeast of the ship behind the drizzle outflow boundary. Along the leading edge of the larger pocket within ~2 km of the ship, signal intensity is greater than -10 dB and is sufficient to detect a 2-3 m s^{-1} flow away from the ship. Thus, the leading edge of the clean and dry pocket nearest the ship appears to be region of divergence. The spatial congruence of the divergence zone near the ship with the leading edge of the large dry and clean pocket suggests that perhaps a turbulent downdraft may be impinging on the surface layer and driving the divergence. The rhi taken at $t_0 - 12$ min transects the vertical dimension of the clean, dry pocket and further supports the conclusion that the clean and dry region has descended to the surface from the subcloud layer. The layer of dry and clean air that had been suspended above the surface mixed layer 20 minutes previously ($t_0 - 30$ min) now extends down to the ocean surface at ranges greater than 2 km. Moreover, both rhi radial velocity scans (not shown) and upward-pointing scans taken showed increased turbulent motions in the 20 minutes preceding the arrival of the drizzle outflow at the ship.

The first half (from $t_0 - 6$ min to $t_0 - 1$ min) of the upward-pointing lidar velocity scan shown in Fig. 3.8 shows a sample of the increased vertical motions observed during this time and further supports the hypothesis that clean and dry air from the subcloud mixed layer may have been entrained into the surface mixed layer from above.

At $\sim t_0$, an updraft of ~ 2 m/s intensity and ~ 900 meter height was also observed in the upward-pointing lidar data as the northeast flank of the drizzle outflow reached the ship. The updraft is slightly stronger and extends higher than the updraft that was observed along the humidity front. The ppi scan taken at $t_0 + 4$ min shows the horizontal extent of the two flanks of the drizzle outflow as they enfold along a zone ~ 2 km to the south and east of the ship. Meanwhile, the leading edge of the encompassing outflow structure has become more linear and exhibits small (<1 km) lobes and clefts. The clean, dry pocket that had been over the ship is now sequestered to the west of the domain. Drizzle is beginning to attenuate the lidar beam to the far south and east and the winds are consistent above 4 m s^{-1} within the outflow region.

The rhis from 604-606 GMT ($t_0 + 8$-10 min) at 213^0 azimuth angle show cross sections of the enfolding flanks of the outflow. The final scan of the three was included in Feingold et al. 2010 (see their Fig. 2). Virga strongly attenuates the lidar beam in the upper portion of each scan. In the first scan ($t_0 + 8$ min) the converging flows appear to stratify behind the collision zone located at ~ 2km range, with positive radial velocities below 300 meters and negative radial velocity above. This pattern perhaps indicates that a portion of the northeast flank, which has a positive radial velocity in these scans, has undercut the south flank. The second rhi ($t_0 + 9$ min) shows that this portion of the flow has propagated away from the ship beyond ~ 3 km range. Although it appears to continue propagating away from the lidar in the final scan ($t_0 + 10$ min), low signal intensity likely caused by attenuation from drizzle prevents further investigation of this feature. At $t_0 + 10$ min the collision

zone itself—now located at ~ 1km range—becomes convex as the south flank undercuts the northeast flank, indicating that the south flank is in fact denser than the northeast flank. This observation suggests that the flow away from the lidar below 300 meters and beyond 2 km range may not simply be a portion of the northeast flank undercutting the south flank, since evidently the south flank is denser. For this reason, it could also be possible that wave-like interactions, such as undular bore formation along the collision zone, may explain this radial velocity pattern. Undular bores have been observed in both atmospheric and laboratory studies of density current collisions (Wakimoto and Kingsmill 1995;Kingsmill and Crook 2003; Kot and Simpson 1987), and radial velocity features in the rhis captured across the collision zone bear similarities with undular bore structure and propagation. Another way of interpreting the velocity pattern behind the head of the collision zone at $t_0 + 8$ and $t_0 + 9$ min is that it is the signature of a vertically oriented counterclockwise circulation. This circulation propagates *away* from the lidar as the collision zone itself propagates *towards* the lidar, which is what we expect the main crest of an undular bore formed in this manner to do. Moreover, at $t_0 + 10$ the south outflow flow located beyond 1 km range takes on a wavy appearance, which perhaps indicates lower amplitude undulations behind the main crest. The pattern results from alternating regions of convergence and divergence that form below 200 meters, combined with an anti-correlated divergence in the above 300 meters. At 1 km and 2 km range, radial velocity is more positive above 300 meters and more negative below 200 meters. At ~1.5 km range there is radial velocities are more positive near the surface and more negative above. The details seen in the velocity field in these scans raise interesting questions about the dynamical interactions consequent to outflow collisions. Unfortunately, the outflows studied here are relatively small and thin, and corroborating evidence for bore propagation in the ship wind, pressure and temperature record is lacking. Furthermore, the lidar captured only snapshots of the flow anomalies about density current collision

zones where drizzle was not severely attenuating the signal, which further limits analysis of the dynamical interactions between these colliding outflows.

B. Surface Air Mass Properties and Winds

Selected ship meteorological variables and aerosol concentrations from 300-730 GMT are shown in Fig. 3.9. Two events, starting at 412 GMT and 556 GMT, met our criteria for a density current during this time. The first density current was accompanied by a relatively sharp drop in temperature of 1.6 K and a pronounced density jump of 0.8 kg m^{-3}. The 556 GMT drizzle outflow was the stronger of the two ($\Delta\rho \sim 1$ g m^{-3} and $\Delta T \sim 2.3$ K) and commenced in two stages corresponding to the passage of the two flanks observed in the lidar ppis (see Fig. 3.8). Unlike the humidity front case, precipitation was measured at the ship during both events. Density increases were larger for both events than for the humidity front, as the cooling was more pronounced and was not offset by large increases in mixing ratio. Notably, an additional drizzle cell precipitated onto the ship at around 650 GMT, though the change in surface air density observed at that time was too small and gradual to meet the density current criterion.

A temperature spike was identified starting at 536 GMT, immediately before the arrival of the drizzle outflow at the ship. The surface air was suddenly dry ($\Delta q_v \approx -2$ g kg^{-1}) and warm ($\Delta T \approx +0.5$ K) at the surface, resulting in a 15% drop in relative humidity. This corresponds to the period in which clear, dry air was observed over the ship in the lidar domain. The fact that temperatures increased and mixing ratios decreased at the surface supports the conclusions drawn from the circulations observed in the lidar. Higher potential temperature, lower mixing ratio air from the subcloud mixed layer was brought to the surface adiabatically from above 400 meter altitude in the minutes prior to the arrival of the eastern flank of the drizzle outflow boundary.

51

Perturbations in pressure are more complex than in the humidity front case. Both density current fronts were accompanied by a *decrease* in pressure and subsequent rebound within the density current. It is not known why an increase in pressure was not observed across the two fronts, though the increase in pressure observed within the core of the two density currents is what we expect to observe in a hydrostatic system.

Aerosol concentrations did not fit a linear trend over the period from 300-730 GMT, except in the Aitken mode. Aitken mode particles roughly halved, possibly due to decreased particle nucleation (Charlson et al. 1987; O'Dowd et al. 2002) after sunset and subsequent loss via coagulation and growth into the accumulation mode (Capaldo et al. 2012) as well as drizzle scavenging during the overnight drizzle maximum (Glantz et al. 2003;Burleyson et al. 2013). Accumulation mode concentrations varied from 26 to 42 cm^{-3} and coarse mode particles numbered between 0.3 and 1.1 cm^{-3}. As in the other density current cases, Aitken mode particles dominated the aerosol number distribution with concentrations ranging from 250 cm^{-3} to 550 cm^{-3}. The lower aerosol concentrations suggested by the reduction in near-surface lidar backscatter intensity within the 545 GMT temperature spike is also confirmed for all modes: concentrations dropped by 150 cm^{-3} (Aitken), 10 cm^{-3} (accumulation), and 0.5 cm^{-3} (coarse). Aerosol concentrations also decreased behind the drizzle outflow at 556 GMT by 75 cm^{-3} (Aitken), 5 cm^{-3} (accumulation), and 0.5 cm^{-3} (coarse). Unlike in the humidity front time series however, aerosol concentrations did not vary consistently with wind speed. This evidences other controlling factors on aerosol loading. The 556 GMT drizzle outflow was unlike the humidity front in that it was near the source drizzle cell and likely transported freshly scavenged air. This may explain why the humidity front brought comparatively dirty air, whereas the outflow in this case carried cleaner air.

C. Boundary Layer Conditions

Fig. 3.10 depicts upward pointing lidar backscatter intensity from 300-700 GMT. Lidar backscatter data for several hours after 700 GMT are unavailable on this day. Relatively intense drizzle was observed over the ship from ~420-500 GMT, from 610-620 GMT, and finally from ~640-700 GMT, with intermittent episodes of virga occurring frequently down to 500 meters height. In comparison to the humidity front case, the evolution of relative humidity and aerosol concentrations through the depth of the boundary layer is rapid and sporadic, confounding mixed layer height estimates via backscatter intensity gradient profiles. Further complicating efforts to determine a boundary layer structure are small, but relatively intense drizzle-induced downdrafts that descend several hundred meters from the cloud base before rushing away seconds later. The lack of smooth and gradual backscatter intensity gradients with altitude, together with inconsistency in backscatter profiles over time, indicate that the ship is not traveling through a well-coupled boundary layer region. However, the cloud layer itself is relatively consistent in both height and fractional coverage. Subcloud cumulus were observed only briefly around 515 GMT. Low backscatter intensities (< -5 dB) also confirm the presence of a clean, dry air descending below 180 meters during the 30 minutes prior to the arrival of the drizzle outflow (525-555 GMT), and further reveals that episodes of less pronounced and sustained drying and cleansing of the lower boundary layer also occurred just before 330, 400 and 500 GMT. Finally, a sudden jump in backscatter intensity extending from 180 meters up to 500-900 meters was observed from 555- 558 GMT, which matches the updraft observed during passage of the eastern flank of the outflow over the ship.

Data from soundings released at 322 GMT are shown in Fig. 3.11. The upward-pointing lidar data (see Fig. 3.10) from 310-320 GMT shares comparable profiles of moisture and aerosol concentrations with the lidar data taken at ~540 GMT. The cloud height is also similar during these two periods. Moisture and aerosol variability in the lower boundary layer and moisture and aerosol

content from 400-800 meter height, however, appears to be higher when the sounding was taken. The profile of virtual potential temperature is very nearly neutral, but there is a ~0.75K jump in virtual potential temperature at ~500 meters consistent with a less-coupled boundary layer. The boundary layer is moister overall than was the case preceding the humidity front. Nonetheless, the relative humidity of the air from 100-200 meters and from 500-800 meters is below 80% and is therefore drier than the surface air sampled at this time, further supporting the hypothesis that the dry and clean pocket ahead of the outflow was sourced in the decoupled boundary layer air above the surface mixed layer.

Boundary layer VADs acquired at 20 minutes intervals from 305 GMT to 625 GMT via upper elevation angle ppis are depicted in Fig. 3.12. Data from the final profile in the period is incomplete due to a small data sample in the estimate of the wind field between 100 and 300 meters altitude. Over the whole case, both speed and directional shear were observed throughout most of the period in comparable magnitude to those observed during the humidity front case. As in the previous case, the highest near surface wind speeds were also observed in association with the two density currents that passed over the ship at 415 GMT and 556 GMT. A final similarity between the evolution of the vertical wind profile between this case and the humidity front case is the negatively covariant evolution of wind perturbations at different heights. As in the previous case, as wind speeds increase above 500 meters, the wind speeds tend to decrease below ~300 meters, suggesting a mesoscale circulation pattern that varies with height. At 603 GMT, 7 minutes after the first flank of the Feingold drizzle outflow passed over the ship, the near surface wind speed and direction at are consistent those observed in the ppi wind field. Additionally, speed shear of ~2.5 m s-[1] was observed from 200 to 600 meters altitude. Unlike the humidity front, the evidence of a return flow over top of the Feingold outflow is not apparent. In fact, the wind above 500 meters slackened and its direction changed very

slightly between 545 GMT and 603 GMT, suggesting that the flow perturbation above the first flank

of the Feingold outflow opposed the mean wind, not the northeasterly outflow.

D. Relationship to Drizzle and Cloud Fields

The C-band radar, satellite IR, and lidar 1^0 tilt ppi mean wind corrected wind field for the this

case are shown in Fig. 3.13. The period was characterized by fairly scattered drizzle with numerous

large and often somewhat linear cells with peak intensities greater than 25 dBZ. In the hour prior to

the outflow the cloud field began to gradually break up in the southern portion of the scene. The radar

confirms the passage of drizzle cells over the lidar domain at around 430, 530, 615, and 700 GMT.

The cell at 430 GMT corresponded to the first density current observed in the ship time series (see

Fig. 3.9), while the 530 GMT cell of ~5 dBZ intensity corresponds to the period of virga observed in

the lidar rhis (see Fig. 3.8). The drizzle cell that passes over the ship at ~615 GMT is associated with

the outflow which crossed the ship starting at 556 GMT. The cell crosses the southeast quadrant of

the radar domain, maintaining a peak intensity of ~30 dBZ as it approaches the lidar domain. By 605

GMT, lighter precipitation (~10 dBZ) has developed to its northeast and west. This configuration of

drizzling cells traces the shape of the outflows observed in the lidar ppis of velocity (see Fig. 3.8).

The outflow boundaries observed approaching from the west and south of the lidar domain are less

than 10 km from drizzling region in and around the main drizzle cell. At 630 GMT, the drizzle

emerges downwind of the lidar with peak intensities arranged along the axis of convergence between

the two outflows located by the lidar volume scans. This linear configuration of drizzle cell intensity

appears to be short-lived however. By 700 GMT, the cell is no longer elongated and has become more

diffuse and circular.

III. Convergence of Two Density Currents (827 GMT 26 October 2008)

In this case, one vigorous and advancing density current was observed colliding head-on with a stalled and dissipating density current within the lidar domain. The collision coincided with the initiation of a new intense and persistent drizzle cell along the zone of convergence between the two flows.

A. Evolution of Kinematic Features

At 827 GMT on October 26 (t_0), a density current crossed the ship while it collided head-on with the remains of a density current that had passed over the ship at 736 GMT. The event coincided with the development of an intense and persistent drizzle cell over and along the zone of convergence. The ship was very nearly stationary during this case. Fig. 3.14 displays lidar scans collected from $t_0 -$ 39 min through $t_0 - 1$ min. At $t_0 - 39$ min, the first of the two density currents had crossed over the ship from the northeast 12 minutes earlier. The frontal zone of the outflow forms a line across the southern and western portion of the domain. The region behind the outflow shows a ~10 dB increase in backscatter intensity, though this contrast is weaker and less consolidated than was observed within the previously discussed density currents. The front is met by a ribbon of lower backscatter air advancing from the southwest. In the southern and western portions of the domain, a distinctive pattern interlaced leaves of higher backscatter intensity develops, which is reminiscent of breaking waves lapping along a beach. Mean wind corrected radial velocities in the observed flow are up to ~3.5 m s^{-1}, and the forward flow appears to be cleft into 2-3 bands congruent to the leaves seen in backscatter intensity data to the south and west of the ship. RHI cross sections oriented roughly along the flow of the density current between $t_0 - 43$ min and $t_0 - 40$ min show a collapsing density current of <300 meter depth. Maximum radial velocities within the flow are 3-4 m s^{-1}, though the density current does not have a persistent classic density current shape and appears to have stalled between

2.5 km and 4 km range. The head of the density current is not well defined as turbulent vortices

penetrate nearly down to the ocean surface.

The second density current is visible in the southwest of the lidar ppi domain at $t_0 - 19$ min.

A narrowing band of lower backscatter intensity ~3-5 km wide lies between the density current front

and the stalled wake of the density current that crossed the ship thirty minutes earlier. Winds within

advancing density current are relatively homogenous and strong, with mean wind corrected radial

velocities of up to 5 ms^{-1}. The line of greatest extent of the first outflow is still visible however as a

thin zone of reduced winds along its frontal zone to the south of the ship. The first outflow is

dissipating rapidly to the south and west of the ship as the band of air ahead of the southwestern

outflow overtakes it. The wind field to the north and east of the ship has also become riddled with 1-5

km zones of convergence and divergence during this time. Although no new large, spreading outflow

is apparent, there is in fact another lightly drizzling cell (<10 dB) in this portion of the domain

starting from $t_0 - 22$ min through $t_0 - 12$ min. Likely as a result, a new and distinct flow towards the

lidar has developed to the north and within 5 km of the ship. The upward-pointing lidar vertical

velocity data were collected from 810-820 GMT. During this time, the zone of decreased backscatter

intensity observed in the ppis was over the ship. Sustained lifting of 1-2 m s^{-1} from 180 meters to the

cloud base was observed between $t_0 - 12$ min and $t_0 - 7$ min. Additional lifting was observed up to

800 meters between $t_0 - 17$ min and $t_0 - 12$ min. The pattern differs substantially from the previous

cases in that lifting was more sustained, deeper, and occurred several kilometers ahead of the

advancing density current.

At $t_0 - 7$ min, ppi scans show that the southwestern density current has advanced to within 1

km of the ship, and the zone of reduced backscatter intensity to the north of the density current has

narrowed to a 1-2 km wide band roughly centered over the ship. This narrowing of the zone is also

accelerated by the flow from the north of the ship first observed in the previous ppi scan, which has intensified to >3 m s^{-1} and broadened to 6-8 km across, so that it is on a trajectory to collide along a comparably long segment of the southwestern density current. The rhi scans taken between $t_0 - 3$ min and $t_0 - 1$ min transected the southwestern density current roughly along its axis of motion. Though smaller than 10 km from head to tail, the depth of layer of maximum flow has a depth of ~400 meters with a well-developed head visible in the $t_0 - 3$ min image. Turbulent vortices are not prevalent throughout the upper portion of the density current, as was observed in the behind the humidity front and the first density current discussed in this case; overall, the layer of maximum flow is also deeper and less concentrated at the head than in those two cases. By $t_0 - 2$ min, the top of the layer of maximum main flow has swelled by about 200 meters at ~1.5 km and ~3 km range, giving the flow an undulating structure. The upper regions of the observed swells are flowing towards the lidar at a reduced speed and the peaks of the flow shift away from the lidar between $t_0 - 2$ min and $t_0 - 1$ min. A wave-like structure is however not seen in the near surface velocity field and the mechanism that generates the undulations is not clear. Nonetheless, it seems reasonable that this structure is related to the closing of the convergence zone observed over the ship over the previous 20-30 minutes, and the collision of the southwestern density current with the flow approaching the ship from the north.

B. Surface Air Mass Properties and Winds

The ship data time series shown in Fig. 3.15 includes three jumps in density that met our criterion for a density current. These density increases occur with the passage over the ship of the three outflows observed in the lidar domain: the northeastern outflow which crossed at 736 GMT, the southwestern outflow at 827 GMT, and a final outflow from the southeast at ~845 GMT. Changes in density were smaller than observed in the other two cases, primarily because temperature decreases did not exceed ~1 K. Mixing ratio increased only ~0.3 g kg^{-1} across the second density current and *decreased* across the other two by ~0.5 g kg^{-1}. The decrease in moisture content observed across two

of the density current fronts may be due to the fact that the prefrontal near-surface environment was very nearly saturated (relative humidity ~90 %), and the cooler air behind the front contained less moisture at saturation. Pressure perturbations behind the fronts were not substantial enough to counteract the downward trend in surface pressure observed over the case period. Surface pressure actually dipped slightly for ~5 minutes after the passage of the 736 GMT and 827 GMT density currents. We do not know why this pressure drop was observed.

A temperature spike was observed starting at 810 GMT, corresponding to the beginning of the period of convergence seen in the lidar data (see Fig. 3.14). The low backscatter intensity observed at the surface during the convergence of the two outflows was therefore accompanied by both warming and drying at the surface. This event therefore bears similarities with the warming and drying observed in advance of the drizzle outflow in the Feingold et al. (2010) case. However, the ppis and rhis from this time do not show the same pattern of increased turbulent motion throughout the boundary layer, accompanied by the subsidence of dry air from the subcloud mixed layer. The dip in relative humidity began just after 820 GMT and corresponds to the arrival of the 1-2 ms^{-1} flow moving ahead of the southwestern density current. It is therefore not known whether this air was associated with a broad region of subsidence, and the ppi scans from this period do not show a pattern of divergence near the surface associated with the dry air (see Fig. 3.14). Although the increase in temperature was comparable, the drop in mixing ratio was more modest than in the Feingold et al. (2010) case.

Aerosol concentrations at the surface bear similarities to the other cases, though correlations with other surface variables are difficult to ascertain. Aitken mode particles again dominate the distribution, with concentrations between 230 and 350 cm^{-3}. Measured concentrations fit a downward linear trend during this overnight period. Aitken mode particles increased slightly by ~20 cm^{-3} within

each of the two density currents which passed at 736 GMT and 827 GMT, countering the overall downward trend. Concentrations dropped by 100 cm^{-1} from 800 GMT to 825 GMT, perhaps corresponding to the demise of the northeast outflow and the increased surface mixed layer height in advance of the southwestern outflow. Accumulation mode concentrations, which varied from 35-60 cm^{-3}, peaked at 755 GMT. They then dropped sharply to a minimum at 835 GMT, only to rebound by 10 cm^{-3} before 845 GMT. This pattern is consistent with northeastern and southwestern density currents being both more laden with accumulation mode aerosol than the prefrontal environment, combined with a larger drop in concentrations within the convergence zone. Coarse mode concentrations varied from 1.3-2 cm^{-3}, and decreased by 0.7 cm^{-3} after the passage of the northeastern density current, yet increased by the same amount from 815-840 GMT. The southwestern outflow and the convergence zone therefore brought cleaner air, whereas the northeastern density current was comparatively dirty. Notably, accumulation and coarse mode aerosol are more abundant from 700-900 GMT than during the previous two cases, despite the fact that wind speeds are lower overall. Moreover, the variability in accumulation and Aitken modes appears to be poorly correlated with wind speed.

C. Boundary Layer Conditions

The evolution of aerosol backscatter intensity throughout the boundary layer from 600-900 GMT is shown in Fig. 3.16. The surface mixed layer varies in height from 400-800 meters, and the cloud base height is more variable than seen during the other two cases. In particular, the cloud base drops behind the first outflow boundary after 730 GMT. Drizzle occurs in the lower boundary layer just before 700 GMT and again between 830 GMT and 900 GMT, with some virga from 600 to 700 GMT and from 750 to 800 GMT. Subcloud cumulus are relatively frequent during the period from 710 to 740 GMT, and were also observed from 820 to 830 GMT. Both of these time periods correspond to the environment ahead of and over top of the two density currents showed in Fig. 3.14.

60

Finally, from 750-820 GMT the layer above the surface mixed layer appears to be considerably moister than at other times, visible here by the lower cloud base and more intense backscatter throughout the column. Between 810 GMT and 820 GMT, a second layer of intense aerosol backscatter (>10 dB) forms about ~500 meters above the surface mixed layer. The appearance of dual layer of intense backscatter between the southwestern and northeastern outflow further indicates a sustained lifting event in the middle of the boundary layer prior to the convergence of the two density currents shown in Fig. 3.14.

Fig. 3.17 shows the sounding data taken at 719 GMT, 17 minutes prior to the arrival of the first density current at the ship. As in the other cases, the increase in virtual potential temperature with height of indicates a layer of stability below cloud. In this case the layer appears to be spread across a comparatively deep layer from 400-700 meters through which potential temperature increase by ~1 K. The mixed layer is moister throughout than in the previous cases, and the transition to the ~15% drier subcloud layer above 700 meters is also more gradual. This pattern is consistent with the backscatter intensity gradients observed in the upward pointing backscatter intensity data at ~725 GMT. Shear was again observed across the boundary layer in this case.

Boundary layer wind profiles acquired at 20 minutes intervals from 605 GMT to 845 GMT via upper elevation angle ppis are depicted in Fig. 3.18. Data collected at 625 GMT appear to be erroneous for an unknown reason. Wind speed varies throughout the period from 3-14 m s^{-1} and wind direction varies between 120^0 and 140^0 before 730 GMT, after which the density currents detailed in this case began to alter the wind profile, particularly in the lower 500 meters. The two density currents that arrived at the ship at 736 GMT and 827 GMT shift the wind direction in the lower 500 meters northward and southward, respectively. The observed near surface wind speed and direction are consistent those observed in the ppi wind field. The lack of a large increase in wind speed within

the two density currents in this case results from the fact that they propagated approximately perpendicular to the mean wind. In the other two cases, the component of the net density current flow in the direction of the mean wind was larger than in this case. Also unlike the other two cases, wind speeds above 500 meters are consistently higher than wind speeds below 500 meters throughout the case period, resulting in positive wind shear of 2-6 m s^{-1} between the two layers. It is therefore more difficult to see the effect of the passing density currents on the near surface flow field as well as any associated wind perturbations above the main density current flow.

D. Relationship to Precipitation and Cloud Fields

The C-band radar, satellite IR, and lidar 1^0 tilt ppi mean wind corrected wind field from 743-843 GMT are shown in Fig. 3.19. The cloud field is breaking up in the vicinity of the ship over this period. Similar to the period surrounding the Feingold et al. (2010) drizzle outflow, the precipitation is characterized by scattered low intensity (<10 dB) drizzle and large, isolated, intense throughout the radar domain. Some of the intense drizzle cells take a more linear form, with arcs of higher reflectivity often aligned with breaks in the cloud field. The radar also confirms the presence of drizzle within 10 km of the ship during most of the period from 743 GMT to 843 GMT. The drizzle cells that passed by the ship as the two density current studied in this case crossed the lidar domain are relatively large (>20 km across) and intense (dBZ >25). The most interesting feature of these radar scans however is the emergence of an intense drizzle cell along the zone of convergence observed in the lidar domain between 800 and 830 GMT. The cell first appears at 743 GMT as a small (~ 10 km) patch adjacent to the southeast portion of the lidar domain. Most of the cell has low reflectivities (<5 dBZ), though a very small portion exhibits >20 dBZ intensity. Starting at 813 GMT, a line of drizzle of >25 dBZ intensity begins to emerge to the northwest of the ship along a line oriented from the northwest to the southeast. This line corresponds to the zone of convergence

observed in the lidar data between the two density currents detailed in this case. Additionally, a new break in the stratocumulus deck is opening up to the cell's north adjacent to the cell. Over the course of the following ~30 minutes, the drizzle cell grows into a line of intense precipitation more than 20 km across. This cell remains active until it exits the radar domain. This pattern suggests that the lifting and moistening of the boundary layer produced by the succession of colliding density currents observed in the lidar data was sufficient to generate an intense and persistent drizzle cell.

Additional evidence for convective initiation and condensation comes from the lidar backscatter data. Fig. 3.20 shows rhi scans taken along and across the zone of convergence collocated with the drizzle cell intensification shown in Fig. 3.19. The first image was taken at 806 GMT ($t_0 - 21$ minutes) along the zone of convergence and show evidence for deep moistening throughout the boundary layer. Backscatter intensity is greater than 0 dB in the subcloud layer and there are two distinct stratocumulus layers visible to the 1100 and 1400 meters height. These observations suggest that the air above the converging outflows seen in the lidar ppi domain (see Fig. 3.14) has been lifted uniformly to its lifting condensation level. The second image shows the rhi of backscatter intensity corresponding to the mean wind corrected velocity rhi from 825 GMT ($t_0 - 2$ minutes), which captured the southwestern density current along its axis of motion as it neared the ship. Multiple cumulus clouds are observed between 300 meters and 800 meters altitude. The clouds are positioned along the top of the southwestern density current, whose head is now within 1 km of the ship. The arc of clouds at 2.5- 4 km range clouds lie over top of the swell that formed at 3-5 km range just before the density current collided with another density current (see Fig. 3.14).
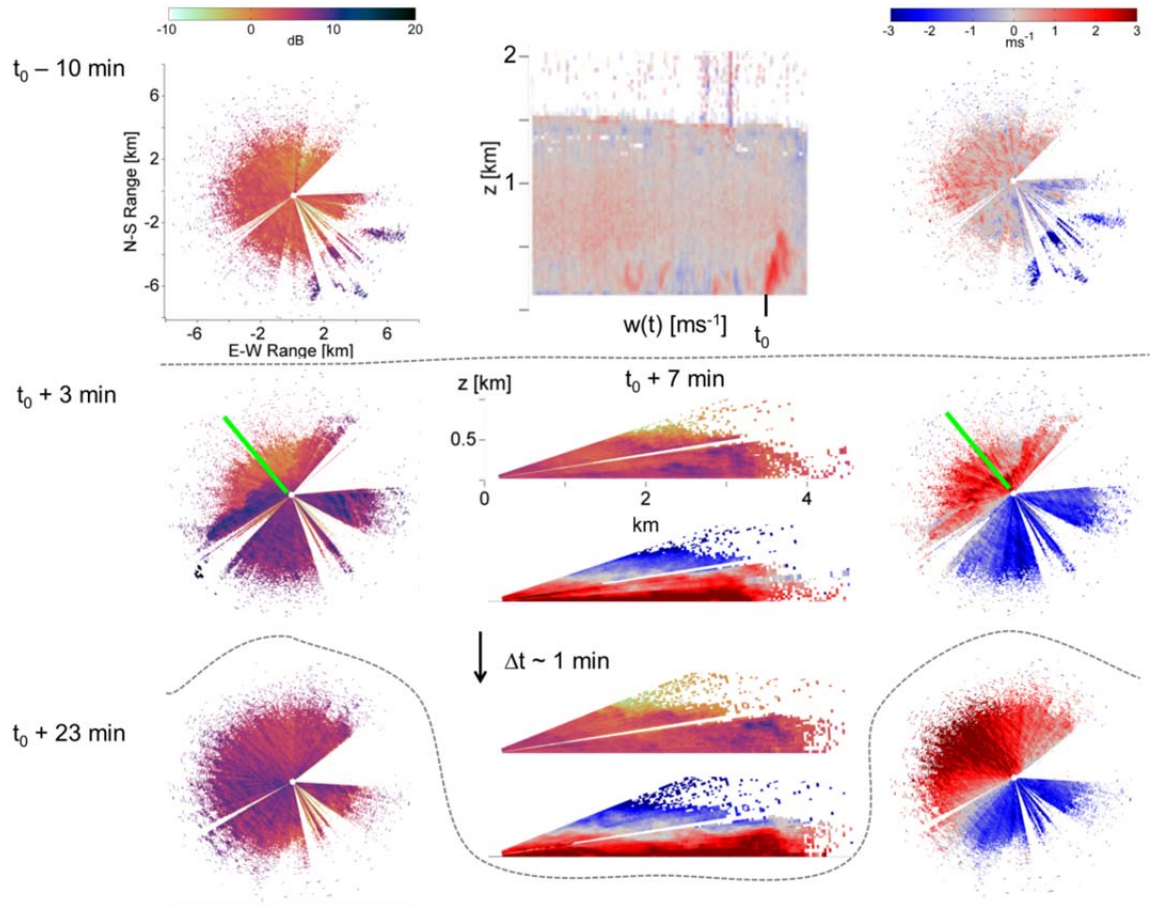
Fig. 3.1: A composite of doppler lidar scans taken before, during and after the passage of the humidity front over the ship at t_0 = 1618 GMT on 26 October 2008. Successive 1^0 elevation angle ppi scans are aligned from top to bottom in the left panel (backscatter intensity) and right panel (mean wind corrected radial velocity). Positive radial velocities (red) indicate motion away from the lidar, negative velocities (blue) indicate motion towards the lidar. Dashed lines group rhi and upward-pointing scans taken at approximately the same time as the ppi scans also contained within the group. At the top of the center panel, one ten minute upward-pointing scan shows vertical velocity measured directly over the ship before and during the passage of the humidity. RHI scans transecting flow behind and across the humidity front are shown in the middle group of the center panel. The green bar superimposed on the two ppi scans within the middle group indicate the azimuth angle of the rhi scans in that group.

64
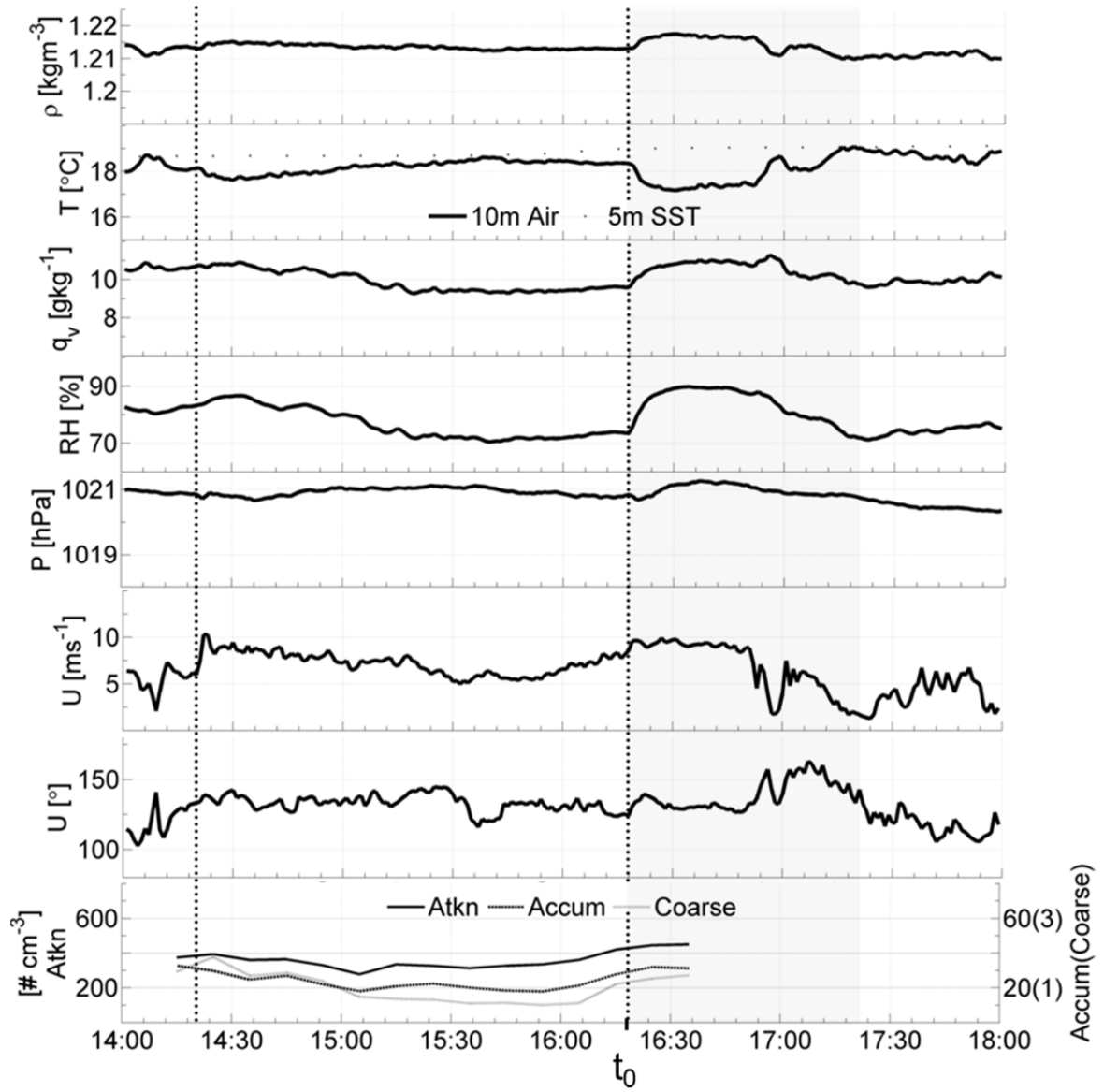
Fig. 3.2: Time series of meteorological variables measured on the ship between 1400 GMT and 1800 GMT on 26 October 2008. Data are averaged over 1 minute intervals, with the exception of the 10-minute average aerosol number concentrations. Vertical dotted black lines indicate the start of a density current front detected in the time series. Light shading indicates the full duration of the density current sampled after the passage of the humidity front at t_0.
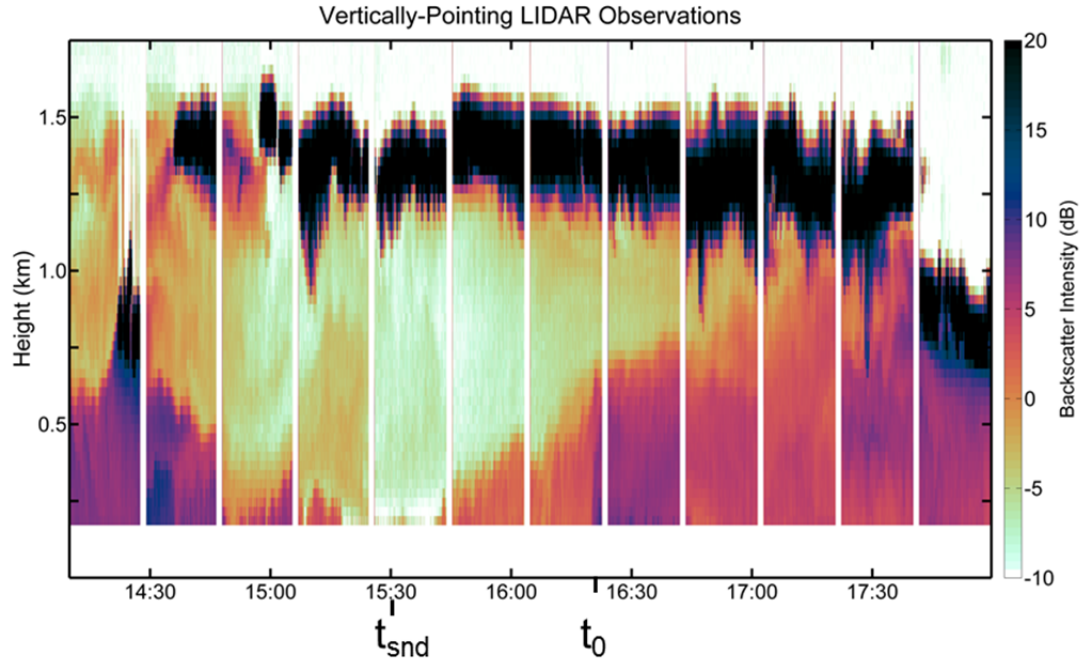
Fig. 3.3: A composite of 10-minute long upward-pointing lidar scans showing backscatter intensity in the boundary layer between 1400 GMT and 1800 GMT on 26 October 2008. For ease of viewing, the 10 minute gap between each of the twelve scans is narrowed. The humidity front start time (t_0) and rawinsonde launch time (t_{snd}) are annotated with a tick on the x-axis.
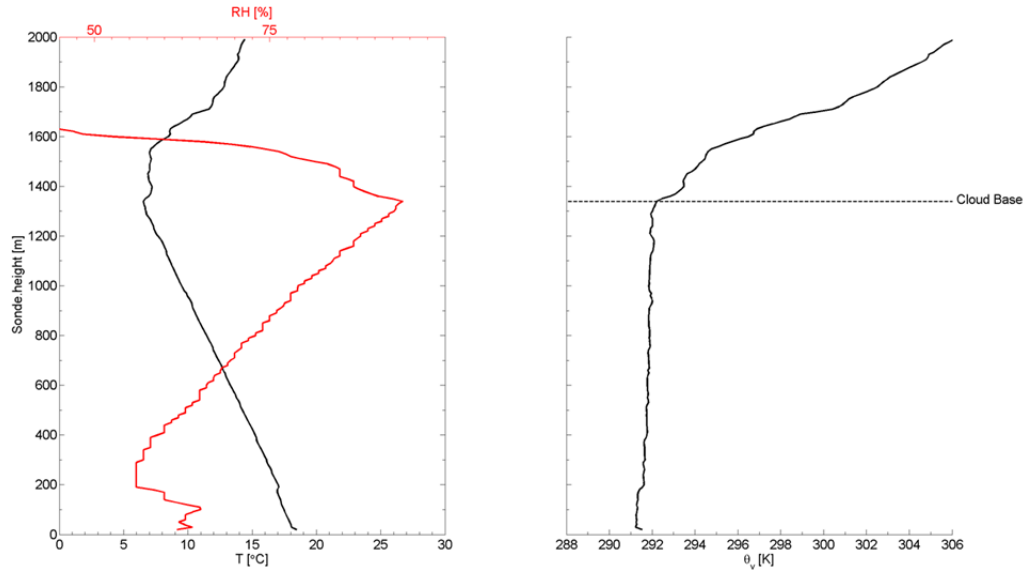
Fig. 3.4: Temperature and relative humidity (left) and dry virtual potential temperature (right) measured between 30 meters and 2000 meters height by a sounding launched at 1530 GMT on 26 October 2008. The height of the cloud base was estimated by ceilometer and is marked by the horizontal dashed line in the right panel.
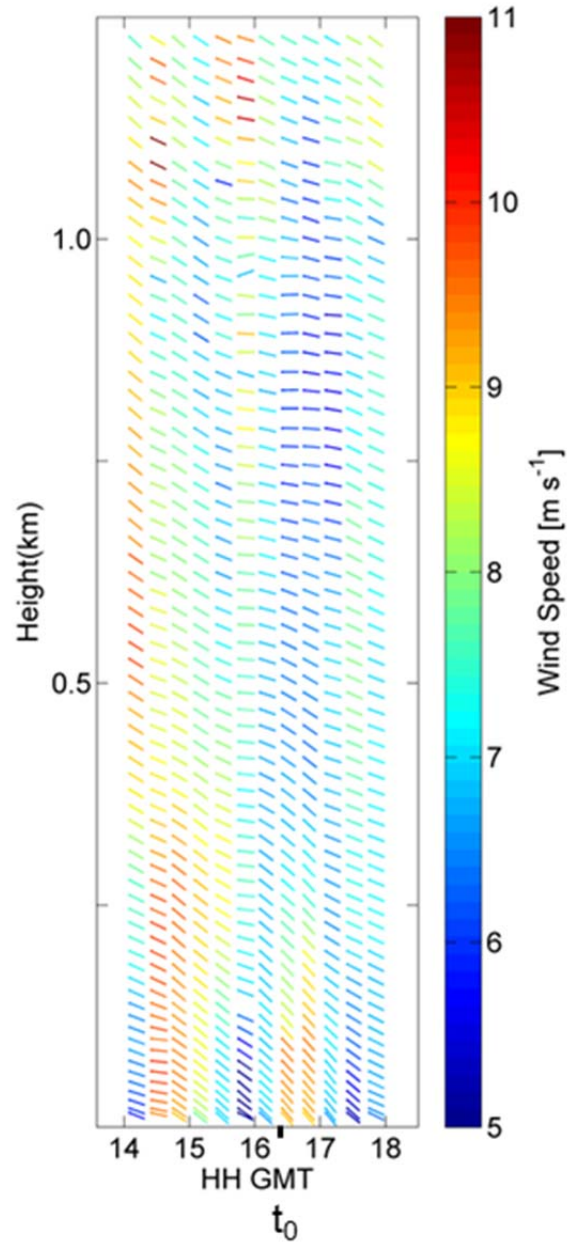
Fig. 3.5: VAD wind profiles derived from upper-tilt lidar ppi scans between 1400 GMT and 1800 GMT on 26 October 2008. Meteorological wind direction along each profile is indicated by the azimuth angle of the line segments with respect to the top of the page.
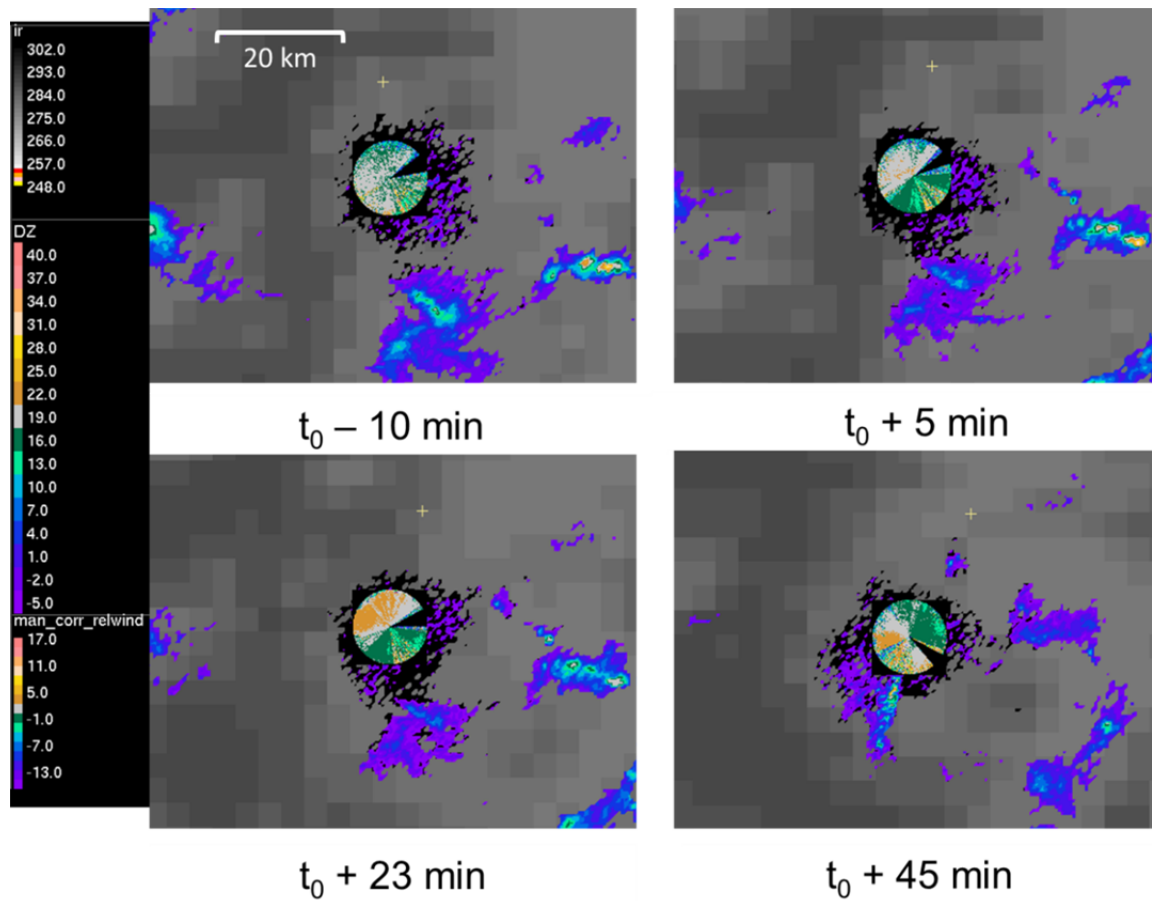
Fig. 3.6: C-band radar, GOES satellite IR, and lidar 1^0 tilt ppi mean wind corrected wind data collected before and after the passage of the humidity front over the ship at t_0. White regions in the satellite field indicate lower cloud cover. The lidar domain covers the 6 km radius nearest the ship.
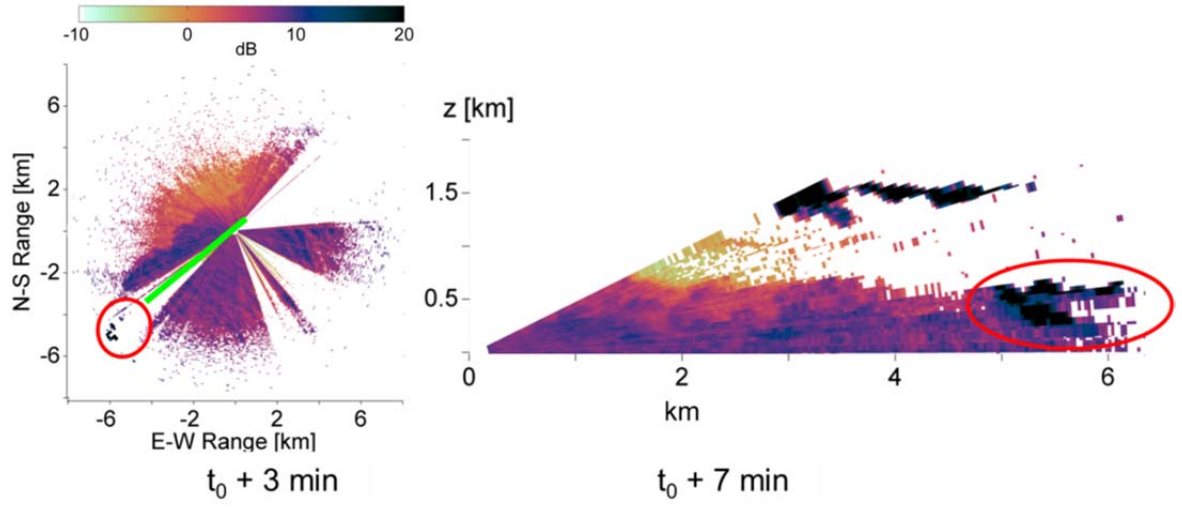
Fig. 3.7: Lidar backscatter intensity collected along and behind the humidity front. The green line in the ppi domain (left) indicates the azimuth angle of the rhi scan (right). A region of backscatter intensities above 20 dB that indicates cloud formation within the frontal zone is circled in red.
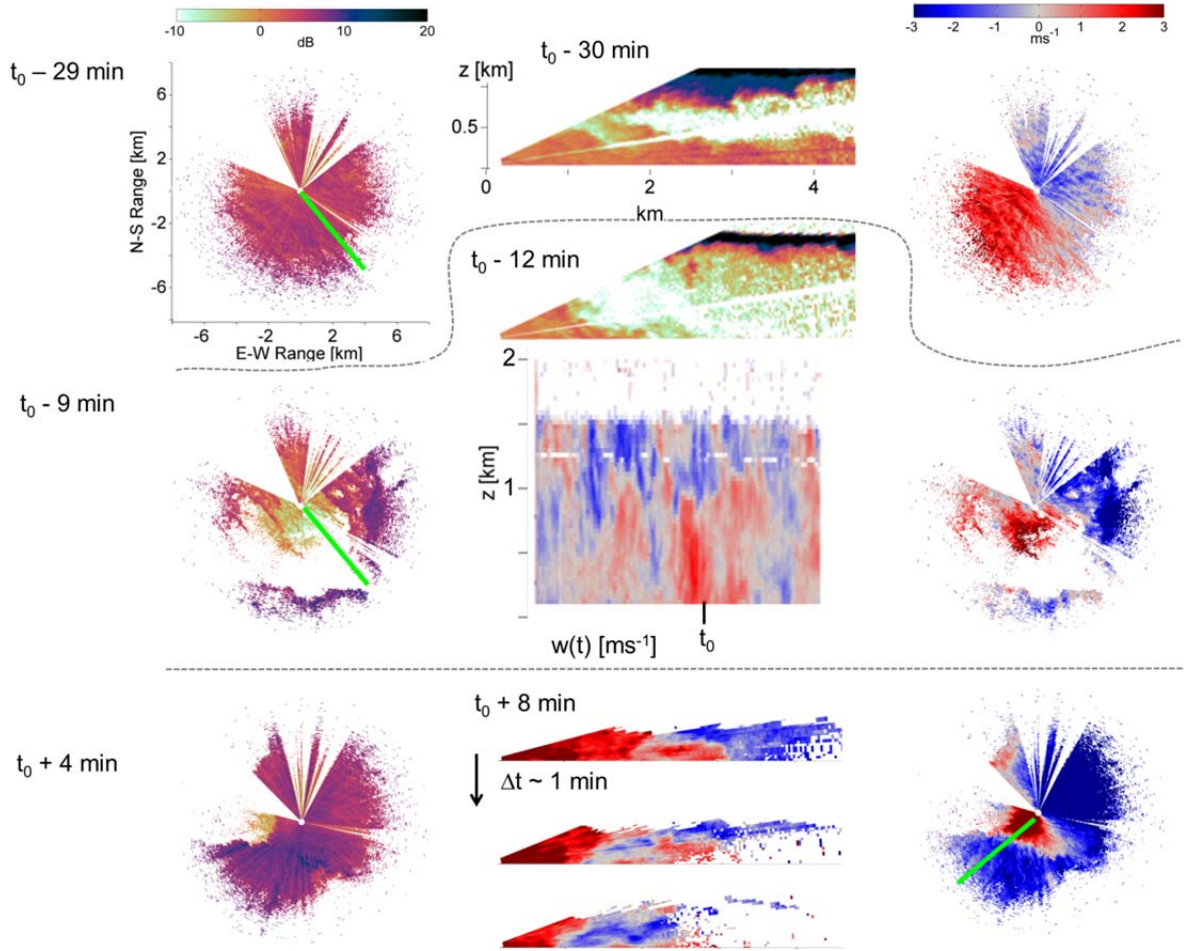
Fig. 3.8: A composite of doppler lidar scans taken before, during and after the passage of the Feingold outflow over the ship at t_0 = 556 GMT on 27 October 2008. The procession and grouping of ppi, rhi, and upward-pointing scans are explained in Fig. 3.1.
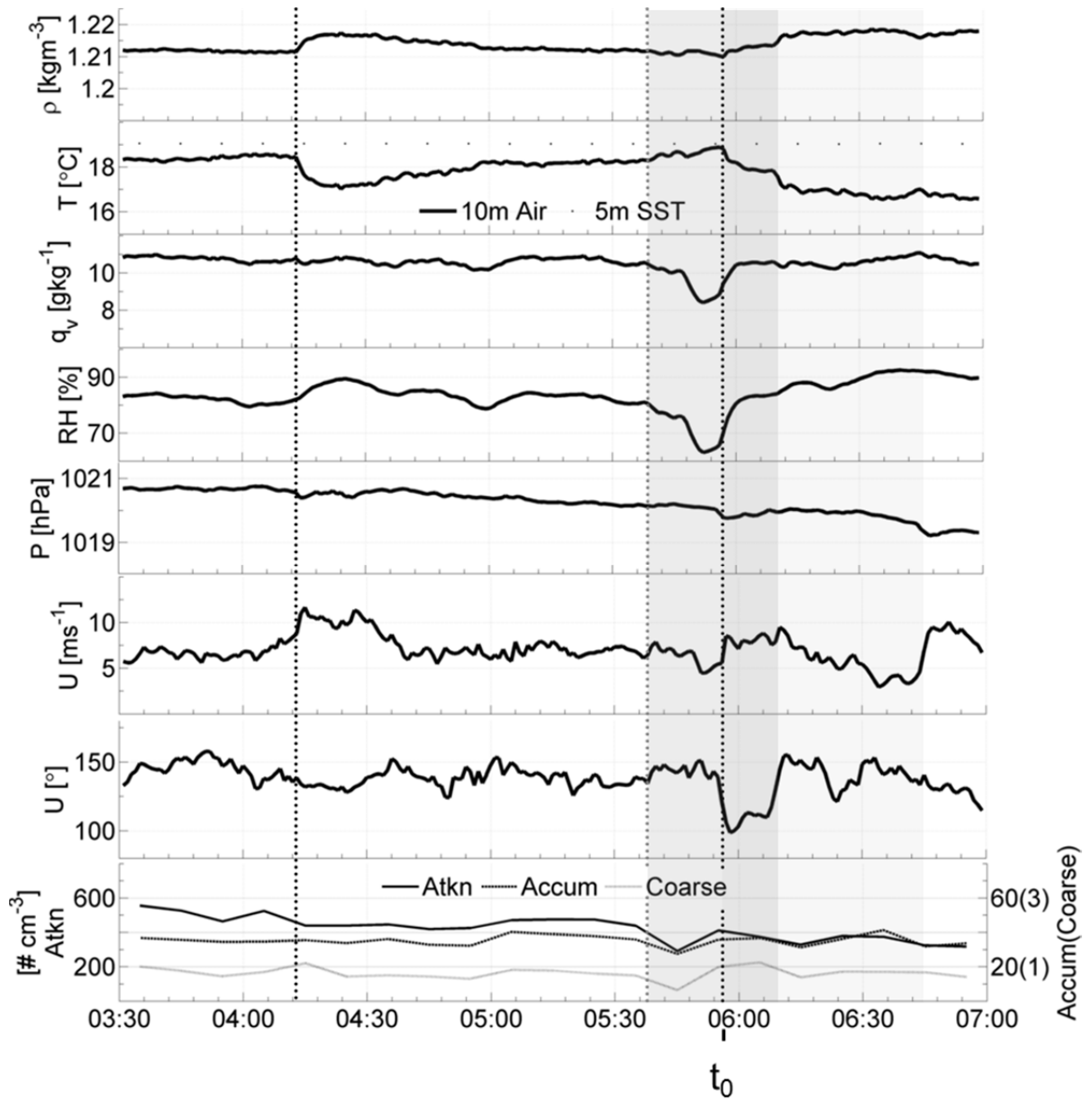
Fig. 3.9: Time series of meteorological variables measured on the ship between 0330 GMT and 0730 GMT on 27 October 2008. Data are averaged over 1 minute intervals, with the exception of the 10-minute average aerosol number concentrations. Vertical dotted black lines indicate the start of a density current detected in the ship data. Light shading indicates the full duration of the Feingold outflow over the ship. The vertical dotted gray line indicates the start of a temperature spike detected in the ship data. The darker shading denotes when the temperature spike was observed ahead of the Feingold outflow. The darkest shading indicates where the rebound of this temperature spike overlapped in time with the Feingold outflow.

72
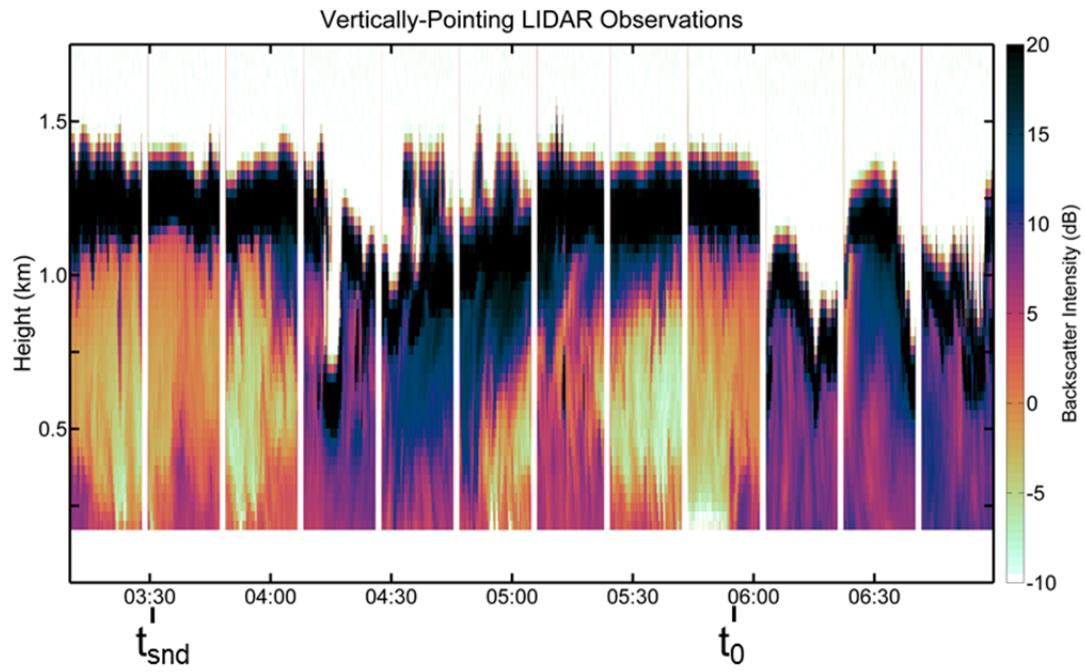
Fig. 3.10: Same as Fig. 3.3, but for the period between 300 GMT and 700 GMT on 27 October 2008.
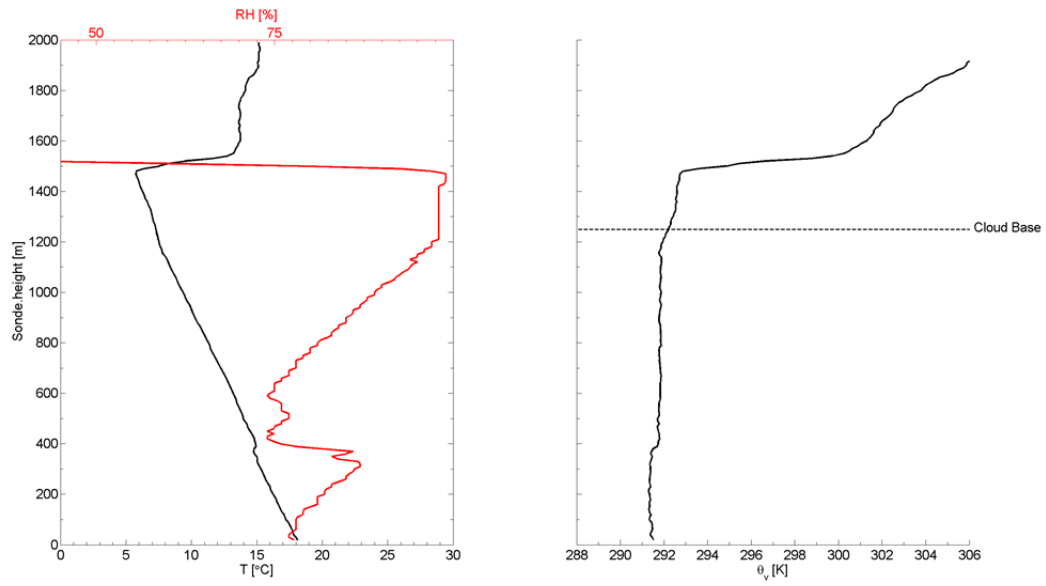
Fig. 3.11: Same as Fig. 3.4, but for the sounding launched at 322 GMT on 27 October 2008.
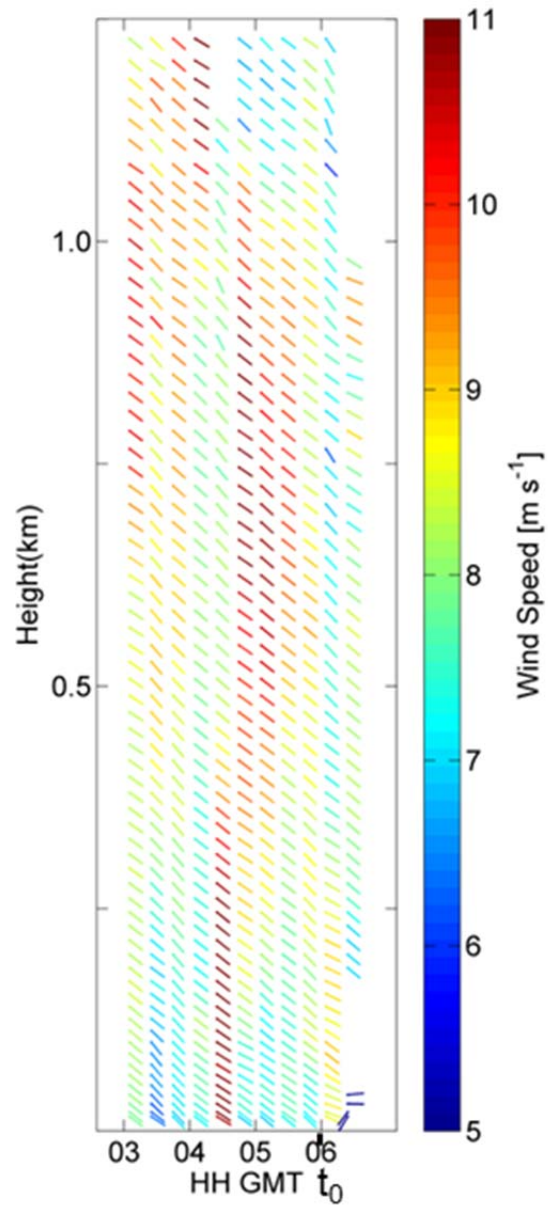
Fig. 3.12: Same as Fig. 3.5, but for the period between 305 GMT and 625 GMT on 27 October 2008.
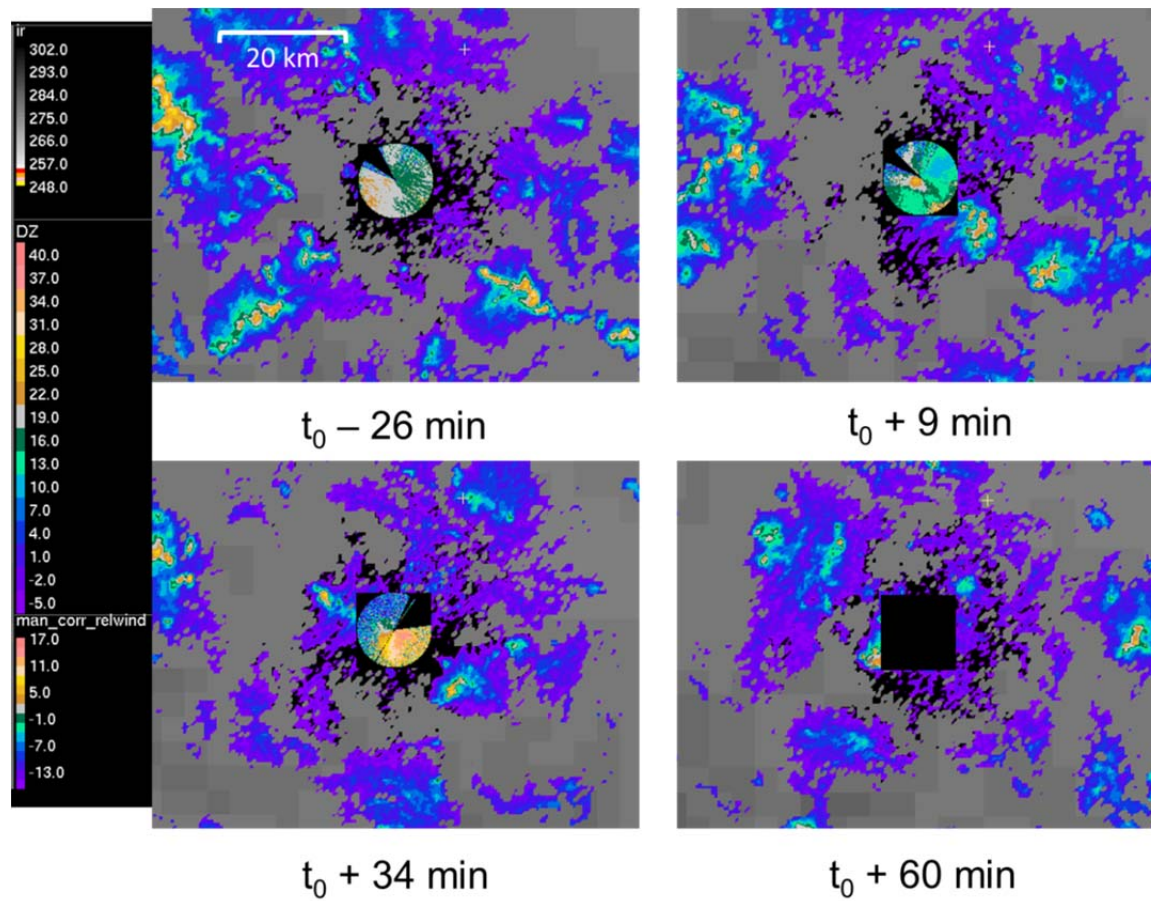
Fig. 3.13: Same as Fig. 3.6, but with t_0 = 556 GMT on 27 October 2008.
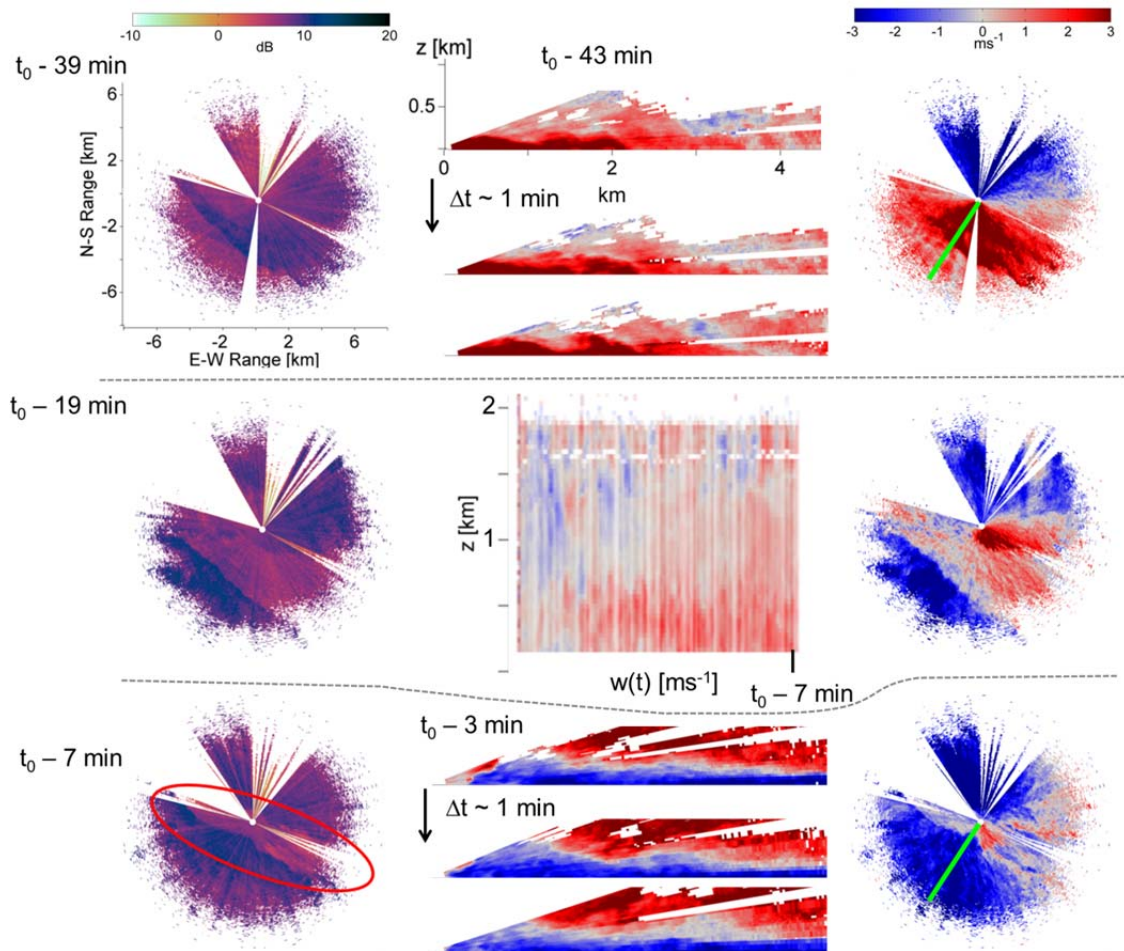
Fig. 3.14: A composite of doppler lidar scans taken of the two density currents that passed over the ship at 736 GMT ($t_0 - 51$ min) and 827 GMT (t_0) on 26 October 2008. These two density currents converged over the lidar domain from $t_0 - 25$ min to t_0. The procession and grouping of ppi, rhi, and upward-pointing scans are explained in Fig. 3.1. The red circle on the ppi scan at $t_0 - 7$ min is around the zone of convergence between the two density currents.
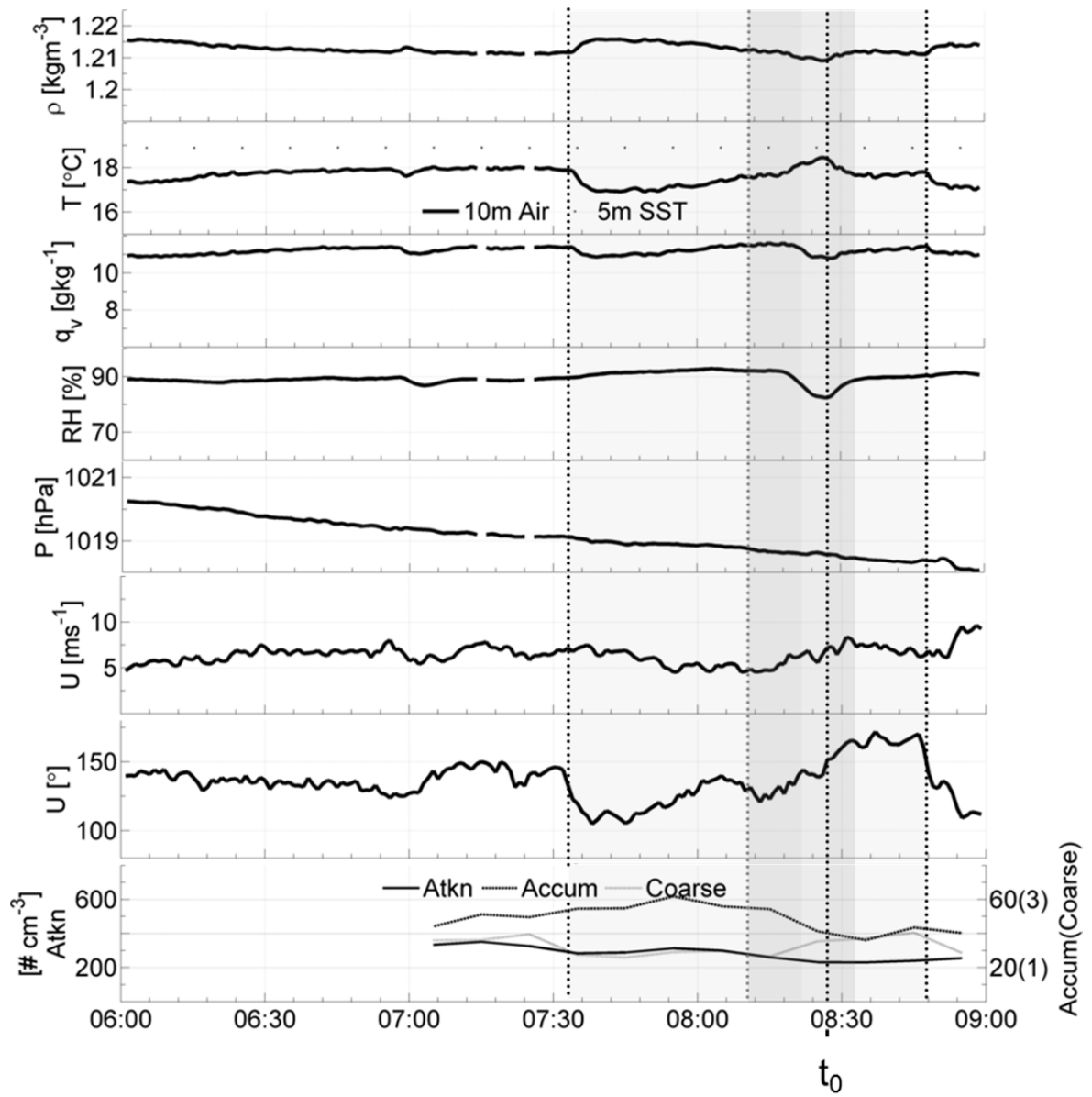
Fig. 3.15: Same as Fig. 3.9, except light shading indicates the presence of either of the two density currents detailed in this case over the ship on 26 October 2008.
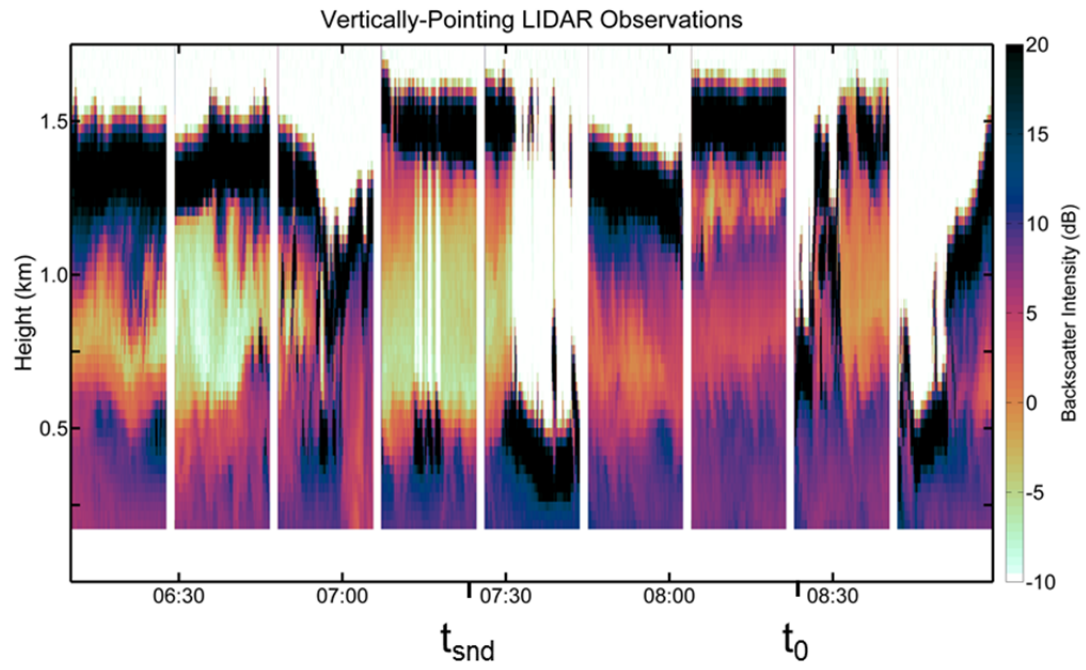
Fig. 3.16: Same as Fig. 3.3, but for the period between 600 GMT and 900 GMT on 26 October 2008.
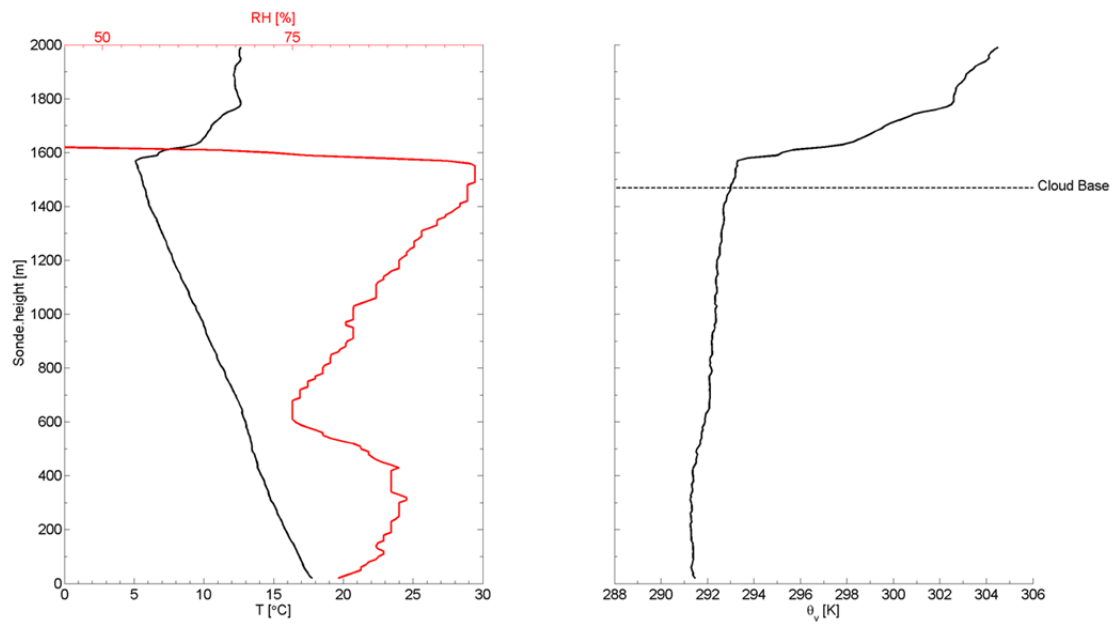
Fig. 3.17: Same as Fig. 3.4, but for the sounding launched at 719 GMT on 26 October 2008.
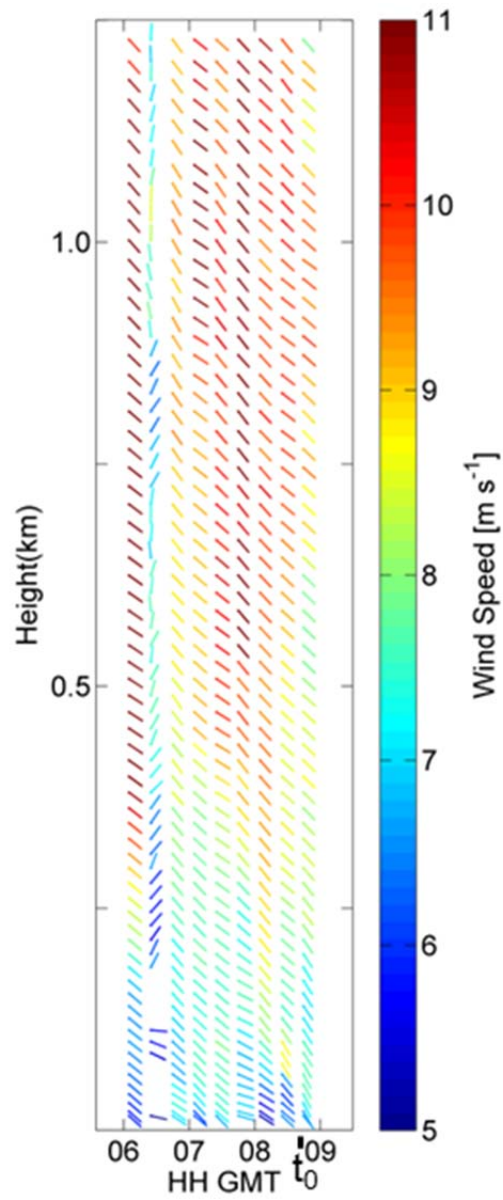
Fig. 3.18: Same as Fig. 3.5, but for the period between 605 GMT and 845 GMT on 26 October 2008.
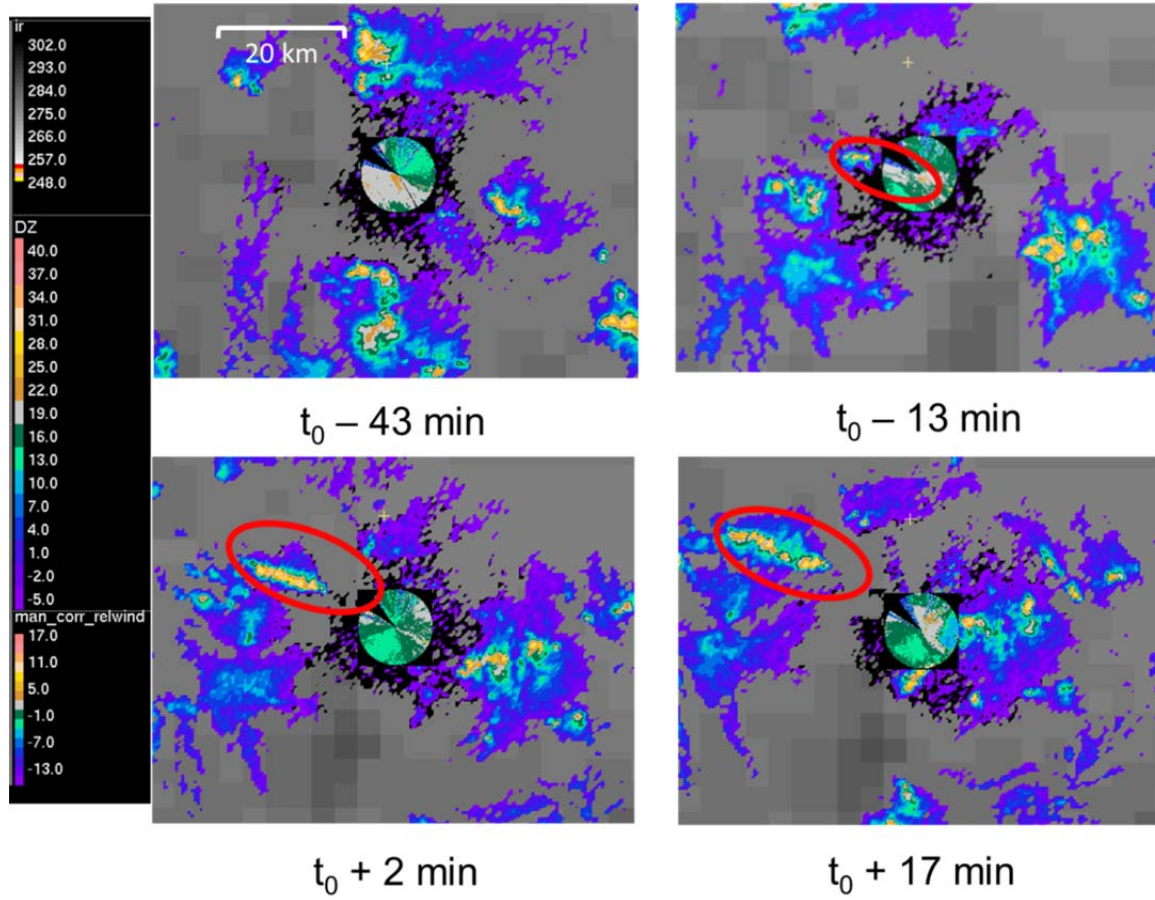
Fig. 3.19: Same as Fig. 3.6, but with t_0 = 827 GMT on 26 October 2008. The red circle indicates the location of a new drizzle cell forming along the zone of convergence between the two density currents detailed in this case (see Fig. 3.14).
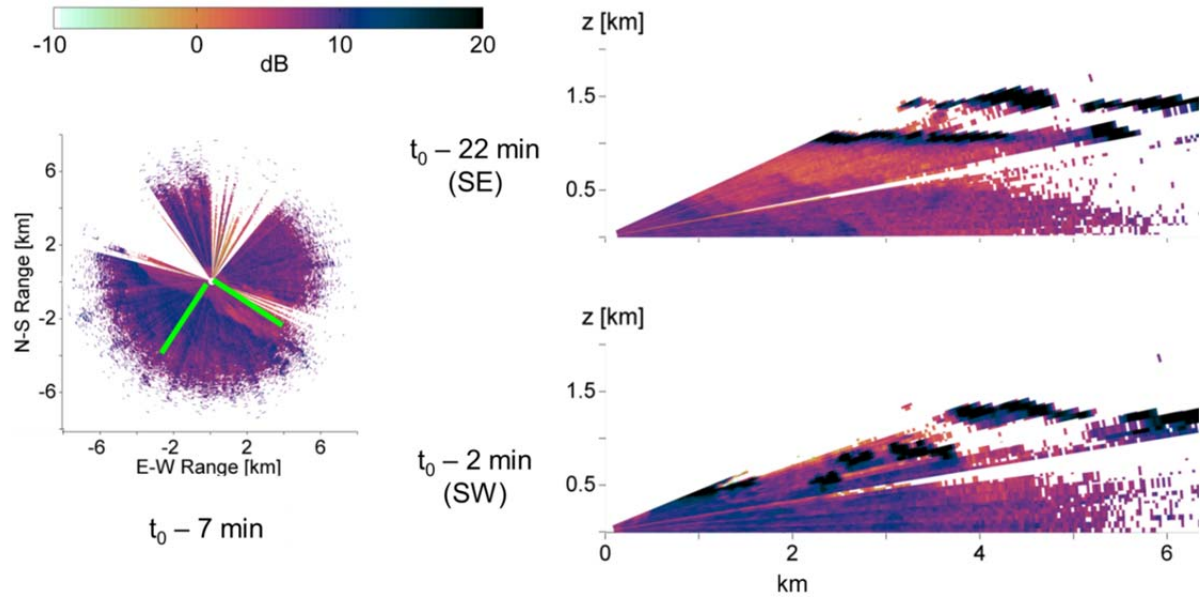
Fig. 3.20: Same as Fig. 3.7, but with $t_0 = 827$ GMT on 26 October 2008. The upper rhi scan was taken roughly along the central axis of the convergence zone detailed in this case. The lower rhi scan was taken through the second density current detailed in this case along its axis of propagation as it approached to within 500 meter range of the ship. Cloud formation is indicated by backscatter intensities above 20 dB.

CHAPTER 4

Density Current Bulk Statistics

I.   Temperature and Moisture Changes Across Frontal Features

Temperature and vapor mixing ratio changes across the combined density current front and

core regions are shown in Fig. 4.a. Surface temperature decreases across the front and core region of

each density current ranged from approximately -0.15 K to -2 K. Water vapor mixing ratio (q_v)

changes across the front and core region varied from approximately -0.75 to 1.25 g kg^{-1}. The four

density currents studied in Chapter 3 are annotated. This result confirms that the case study density

currents were among the stronger density currents observed during the cruise. In particular, the

combined drop in temperature across the two flanks of the Feingold outflow (-2 K) was an outlier.

Cases in which q_v decreased across the front and core region are believed to result from the presence

of very nearly saturated near-surface air in advance of the cooler air within the density current.

Temperature and vapor mixing ratio changes across cold pool edges are shown in Fig. 4.1b. The

majority of the cases identified as density currents had a portion of their structures also identified as a

cold pool edge. Recall from Ch. 2 that Terai's cold pool definition identifies a narrower segment of

the full transition in air mass properties observed as a density current passed the ship. Since the cold

pool definition encompasses only a portion of density current transition, on average the cold pool

edges had smaller decreases in temperature and slightly larger increases in moisture content than

density current front and core zones. Across the cold pool edges, temperature dropped between

approximately -0.2 K and -1.7 K and the moisture change varied from -0.6 to 1.6 g kg^{-1}. The cold

pool edge associated with the Feingold outflow in particular showed a much smaller (~-1 K) drop in

temperature than our algorithm (~-2 K). This is because the cold pool algorithm did not detect both

flanks of the outflow observed in that case (see Chapter 3, Fig. 3.8) This may change upon future

revisions to the cold pool identification method.

II. Estimates of Density Current Dimensions

Estimates of the size of the front and core region compared with the size of the tail region of

each density current are shown in Fig. 4.2. These size estimates were obtained by calculating the

resultant displacement of the ship relative wind vector over the density current feature. The majority

of density currents tail regions were found to be larger the corresponding front and core region. The

front and core regions were between 3 km and 17 km in length and tail regions varied in size from 2

to 27 km.

Fig. 4.3 shows the ship transect length through the frontal zone and tail zone of each density

current as a function of the change in density measured across the frontal zone or tail zone

respectively. Because our algorithm uses a slope criteria to identify density current frontal zones, it is

not surprising that the increase in density across frontal zones is well-correlated with its ship transect

length across the frontal zone (Fig. 4.3a). The density drop across the tail region reliably increases

with increasing ship transect length (Fig. 4.3b). This suggests that there is a somewhat consistent

process by which density decreases across density current tail zones. Additionally, the rate of density

decrease across the tail region tends to be significantly more gradual than the rate of density increases

across the frontal zone. Generally, this finding is consistent with our understanding of density current

flow structure and evolution. The frontal zone is maintained and propagated forward by hydrostatic

pressure gradients caused by sharp horizontal density gradients. The dynamics in the tail region are

however dominated by gradual turbulent mixing processes. A sharp density and temperature gradient

at the end of the density current tail would be the signature of a ship transect through a radially

symmetric cold pool with outflow boundaries of roughly equal intensity on all sides. Instead, the

outflow boundary sampled on the back side of the cold pool appears to be consistently much less intense then its front side. This finding is surprising because it does not appear to be consistent with previous studies of marine shallow convection which assumed a somewhat radially symmetric precipitation outflow structure (Terai 2011; Feingold 2010; Zuidema 2012).

The distribution of estimated depth of the main flow for 33 density currents observed in lidar rhi radial velocity scans is plotted in Fig. 4.4. The depth of maximum flow was estimated by manually detecting the altitude at which the mean wind corrected radial velocity within the density current flow began to decrease rapidly with height. The depth of the main flow was found in all cases to be between 200 meters and 650 meters. When the density current head was seen in the rhi scan, it was found to be 50-200 meters deeper than the flow immediately behind it. Therefore, the estimate of main flow depth was lower when no density current head was seen. The density currents observed however showed remarkable consistency in their main flow depth and the flow appears to be constrained to several hundred meters below the stratocumulus cloud base height in this region, which typically exceeded 1000 meters. The depth of the turbulent zone over top of the density current is not shown because the upper reaches of the density current flow were often attenuated by clouds and drizzle. Where it was observed, the layer of increased shear over top of the main density current flow was found between 200 meters and 900 meters altitude.

III. Frontal Updrafts and Associated Cloud Features

Each of the vertically-pointing lidar scans collected during the passage of 24 density currents over the ship are displayed in Fig. 4.5. Backscatter intensity (left) and vertical velocity (right) for each density current are assigned to a row. The origin of the x-axis is set to the time that each density current crossed the ship (i.e. x=0 at t_0) within one minute accuracy. The first three rows show the data acquired during the passage of three of the case study density currents—see Chapter 3. The humidity

front is shown in row 1, the Feingold outflow boundary is shown in row 2, and the first of the two converging density currents in the third case study is shown in row 3. Rows are arranged roughly in order of lower to higher of the degree of coupling between the cloud layer and ocean surface as evidenced by the backscatter intensity gradients present in the boundary layer. The first twelve rows either have lower backscatter between ~500 meters and ~1000 meters, indicating less moisture and aerosol below the stratocumulus layer, or have more extensive sublcoud cumulus below 1000 meters ahead of the density current. These indicators both suggest a less-coupled boundary layer. The dozen rows afterward (rows 13-24) mostly exhibit higher backscatter throughout the boundary layer, suggesting a higher degree of coupling.

The backscatter intensity data in Fig. 4.5 indicate that subcloud cumulus formation was often quite extensive just before and after density currents crossed the ship. Subcloud cumulus formed above the frontal zone (e.g. rows 3, 4, 5, 6, 7, 8, 9, 11, and 12), often in a large shelf distinct in form to the sporadic cumulus typically observed in less-coupled boundary layers (compare row 17). Multiple cloud layers beneath the stratocumulus deck can also occur (e.g. rows 4, corresponding to cloud photo in Fig. 4.6). The base of the stratocumulus deck sometimes descended by up to 300 meters as the frontal zone approached, and this effect was most obvious when subcloud cumulus were not extensive (e.g. rows 14, 15, 17, and 20). Perhaps the stratocumulus deck lowered due to cooling and moistening of the boundary layer in the region surrounding the density current front.

Examination of the vertical velocity data (right column of Fig 4.5) shows that updrafts were consistently observed over top and immediately prior to the arrival of each density current. The updrafts extended between 300 and 1000 meters height, with maximum speeds within individual updrafts of between ~0.5 m s^{-1} and ~4 m s^{-1}. Clouds often attenuated the lidar signal at the tops of the updrafts, which limited the maximum height estimates in these cases. The updrafts showed some

variations in overall shape, which indicate complexity in lifting duration and the altitudes over which the lifting progressed. For example, the updraft observed over the density current shown in row 4 was less intense and lasted longer than the updraft observed in row 6. Additionally, many of the updrafts appear slanted, and this could occur for two reasons. One is simply that the density current itself began to occupy the lowest levels behind the initial updraft, thereafter confining the updraft to the altitudes above it (e.g. rows 1, 6, 8, and 9). Another reason for the slant in the updraft may be vertical shear across the layer above the main flow. Where it was exhibited, the slanting was consistently orientated back over the density current, indicating increasing motion against the density current flow with increasing height. The slanting of the updraft was stronger in some cases than others (e.g. row 13 vs. row 15). These differences may either indicate differences in the intensity of the shear over top of the density current frontal zone, or in the curvature of the density current frontal boundary. Finally, in a few cases the updraft along the frontal zone was not prominent (rows 17, 18, and 23).

Additional information about the characteristic cloud structures found along density current frontal zones is provided by photographs taken from the deck of the ship. Fig. 4.6a shows a panoramic image taken of a drizzle cell as it bypassed the ship at ~1205 GMT on 27 October 2008. This drizzle cell is also visible in the radar domain to the east of the ship at this time in Fig. 4.6b. The passage of the density current associated with this drizzle cell was captured at 1213 GMT in the upward-pointing scan shown in Fig. 4.5, row 4. The cellular structure of this isolated drizzle cell in an open cellular region is striking. The outflow near the top of the cell is especially prominent in the photograph. This flow is traced by the somewhat diffuse anvil-like cloud pattern spreading out beneath the inversion (e.g. in the top half of red box B). The cell also exhibits cumulus cloud layers in the mid-levels of the cell circulation (red boxes A and B) and a shelf cloud immediately over top of the main density current flow (red box C). The mid-level cloud formations adjacent to the region of greatest precipitation (red box A) show evidence of a stronger inflow pattern. This is noticeable to the

right side of box A, where cumulus clouds are increasing in altitude with decreasing distance to the cell, suggesting that they are being lifted as they stream into the cell's mid-level inflow. Cumulus clouds are also formed up to at least 20 km behind the main drizzling region (red box B). These trailing cumulus structures have a roll-like structure and are present along and above the frontal boundary of the density current.

Fig. 4.7 shows a panoramic photo (Fig. 4.7a) of a linear cloud formation above the frontal zone of density current which crossed the ship at 1544 GMT on 28 October 2008. A lidar rhi scan (Fig. 4.7b) captures this cloud band that formed between ~300 meters and 500 meters altitude, well below the stratocumulus deck and directly along the density current's frontal zone. The associated mesoscale cloud and precipitation field is shown in Fig. 4.7c, which indicates that the precipitation field associated with the density current is less intense and more diffuse than the drizzling region shown in Fig. 4.6.

Fig. 4.8 shows a final panoramic photo (Fig. 4.8a) of a precipitating shelf cloud above the frontal zone of density current which crossed the ship at 1353 GMT on 29 October 2008. The passage of the density current associated with this feature was captured in the upward-pointing scan and is shown in 4.5, row 13. The lidar data indicate that the boundary layer environment was more coupled. The associated mesoscale cloud and precipitation field shown in Fig. 4.8b confirms that the stratocumulus cloud deck exhibited a closed cellular configuration and high cloud fraction, suggesting a more coupled regime. Unlike the Figs. 4.6 and 4.7, this shelf cloud appears to be connected to the stratocumulus deck and is definitely precipitating. This is confirmed by the band of increased radar reflectivities to the southeast of the ship in Fig. 4.8b.

IV. Relationship to the Mesoscale Precipitation Field

As expected, density currents were found to be closely associated with elevated rain rates in the vicinity of the ship. Fig. 4.9 shows the relative frequency distribution of areal average rain rates within 15 km of the ship for radar scans taken at the start of a density current compared with the distribution at all times during the cruise. Approximately ~13,000 radar scans comprise the full data set, of which 70 correspond to the crossing of a density current front over the ship. The 15 km maximum radius was selected as trade-off. On the one hand, the 15 km radius is large enough that it is likely to capture the specific drizzle cells capable of producing an outflow which reached the ship at the time of the radar scene. On the other hand, the radius is small enough that the increases in rain rate associated with these specific drizzle cells are not averaged out over too large of an area. It should therefore be kept in mind that these rain rates are not intended to be representative of the larger mesoscale precipitation field. The areal average rain rates within 15 km of the ship that are coincident with density currents crossing over the ship are overall significantly higher than the distribution throughout the rest of the data set. Approximately 88% of drizzle scenes captured when a density current crossed the ship were accompanied by local areal average rain rates in excess of 0.1 mm d^{-1}. By comparison, only about 10% off all drizzle scenes exhibited local areal average rain rates in this range. This fact suggests that density current fronts are very likely to be in close proximity to moderate or intense drizzle.

Further evidence for diagnosing the observed density currents as drizzle outflows comes from the measurement of cloud liquid water path (LWP) directly over the ship. Fig. 4.10 shows radiometer-derived 10-minute average cloud LWP observed at the start of each density current vs. the change in cloud LWP across the front and core zone. Conservative estimates of the minimum LWP threshold for moderate to heavy drizzle are 200 g m^{-2} (Zuidema et al. 2005; Bretherton et al. 2004; Miller 2012). LWPs above 200 g m^{-2} were observed in ~60% of density current cores identified. The

90

additional 40% of cases may be explained by the fact the density current was sampled as it travelled away from its source drizzling region, which bypassed the ship entirely. Notably, two out of four density currents described in Chapter 3 fit this scenario (see Fig. 3.19).

A visual inspection of radar and lidar data indicate that the majority of density currents exhibited frontal zones that were systematically aligned to the borders of precipitating regions near the ship (for example, see Chapter 3 Figs. 3.13 and 3.19) The relationship of density current frontal zones to the gross and fine structure of drizzle cells is rather complex and difficult to summarize via a comparison of lidar-derived density current location and the radar-derived precipitation field. Density currents were observed when very light rain was observed in the vicinity of the ship. One such case was the humidity front (see Chapter 3 Fig. 3.6). The humidity front case demonstrated that density currents could be present in the immediate vicinity of regions of virga and light precipitiation, without moderate or heavy drizzle present within 15 km range of the ship. Light precipitation would not markedly increase areal average rain rates. For this reason, some of the density currents may be associated with drizzle even if areal average rain rates near the ship are low. A possible explanation for these cases is that localized convective initiation along the outflow boundary could extend the range of a propagating outflow by maintaining a small but persistent band/patch of light drizzle and virga along and behind the frontal zone. Such phenomena are difficult to verify with radar data, because the accompanying precipitation is likely to be light, narrow and broken in coverage, and detectible only very near the ship. These characteristics make for a radar signature that is easy to confuse with sea clutter. Moreover, instantaneous cross-referencing of the radar and lidar data is not possible for such small and localized features, because the lidar data are situated largely within the cone of silence of the radar.

V. Relationship to Areas of Open Cells

Density currents were observed in both open and closed cell regions as far east as 76 W (not shown). However, density currents were preferentially observed in the west of 80W within or beside a large area of open cells that was seen in the IR satellite domain between 26 October and 28 October. Areas of open cells are by definition associated low cloud fraction but they are also correlated with exceptionally high drizzle rates (Comstock et al. 2005; Stevens et al. 2005) and very scarce accumulation mode aerosols (Petters et al. 2006; Sharon et al. 2006). Areas of open cells have often been observed to encroach upon the surrounding closed cellular regions, and such transitions are associated some the highest rain rates observed in the Southeast Pacific stratocumulus region (Wood et al. 2011; Comstock et al. 2005).

Fig. 4.11 shows the relationship between mesoscale conditional average rain rates, accumulation mode aerosol concentrations and satellite-IR derived cloud fraction averaged over the duration of the density current. To eliminate contamination from sea clutter, conditional average rain rates are estimated between 25 km range and 60 km range from the ship. Of the 70 density currents, 66 had aerosol concentration data available. The data indicate that slightly more than half of the density currents (34) were observed in an open cell region. Additionally, the data confirm the expected correlation between lower aerosol concentrations, higher rain rates, and lower cloud fraction observed in open cell regions. Aerosol concentrations above 50 cm^{-3} tended to occur when cloud fraction was near 100% and these higher aerosols concentrations are not well-correlated with precipitation intensity. These findings support the idea that the aerosol-cloud interactions that characterize open cells are quite distinct from those occurring in closed cell regions. It also hints that the 'switch' needed to form and maintain an open cell region may be 'turned on' when conditional rain rates exceed a specific value (here, ~7-8 mm d^{-1}) and accumulation mode aerosol concentrations

fall below a specific value (here, ~50 cm^{-3}) (Savic-Jovcic and Stevens 2008; Wang et al. 2010; Feingold 1999).

VI. Evidence for Previous Aerosol Scavenging within Density Currents

Fig. 4.12 plots the change in aerosol number concentrations across the front and core of each density current as a function the number concentration at the start of the front. Aerosols concentrations in accumulation mode, Aitken mode, and coarse mode were not observed to consistently drop after the density current passed over the ship. This finding is surprising because we expect to see evidence of previous cloud processing within outflows, particularly in the coarse mode and accumulation mode where aerosol scavenging is generally most efficient (Glantz et al. 2003; Wang et al. 2011). This result is partly consistent with Terai (2011), who sampled cold pools at ~150 meters altitude and found no statistically significant change in fine mode (< 1 µm) aerosol concentrations inside cold pools. However, he found a statistically significant increase in coarse mode aerosol inside cold pools, which does not appear to be the case in the ship data. Additionally, the lack of a downward trend in aerosol concentrations was observed in the ship data regardless of starting concentrations. This further indicates that the trace of scavenging was not more pronounced in comparatively dirty boundary layers, where preferential scavenging of the larger accumulation and coarse mode particles should be most noticeable. These findings support the conclusion that the signature of aerosol scavenging is insufficiently pronounced to be consistently observed within the near-surface outflow.

We suggest that the decrease in aerosol concentrations due to cloud processing is counteracted by three processes occurring in the near-surface layer. First, surface aerosol fluxes are enhanced by the higher wind speeds observed within the density current (Ovadnevaite et al. 2012; O'Dowd and de Leeuw 2007). Second, lower virtual potential temperature within the density current

increases stability beneath the stratocumulus layer. The stable layer present above the surface traps

aerosol beneath and within the main flow of the density current thereby reducing turbulent diffusion

of aerosol upwards. Finally, the higher relative humidity observed within density currents may shift

the aerosol size distribution towards the larger size modes through hygroscopic growth. We observed

that Aitken mode particles were typically present in higher (up to 10x) concentrations than larger

particles for density currents occurring near heavy precipitation (e.g. see Chapter 3: Figs. 3.2, 3.9, and

3.15). This indicates that the mode of the aerosol number distribution was sometimes well into the

ultrafine mode, and hygroscopic growth could therefore increase concentrations in all three size

modes.

VII.   Relationship to the Diurnal Cycle of Precipitation and Boundary Layer Stability Below

   Cloud

Fig. 4.13 shows the diurnal cycle of aggregated times when density currents were observed

over the ship. For example, a density current passing over the ship from 6:30 to 7:15 UTC would

count as 30 min between 6 and 7 UTC and 15 min between 7 and 8 UTC. Density currents occurred

throughout the day, though they were most frequent in the morning and least frequent in the afternoon

and evening. The diurnal cycle of density current frequency peaked between 5AM and 11AM local

time. For comparison, Burleyson et. al's (2013) diurnal cycles of drizzle area and areal average rain

rates are shown in Fig. 4.14a,b (their Fig. 8b,c). The peak density current period is between one and

six hours after the overnight peak in areal average rain rates and total drizzle area observed in the

western portion of the VOCALS domain (W of 80W). The timing of the density current peak is

therefore intriguing because it coincides with a period of *decreasing* precipitation coverage in the

mesoscale environment surrounding the ship.

An explanation for the delayed peak in drizzle outflow occurrence may come from an examination of the diurnal cycle of subcloud boundary layer stability when density currents are and are not present over the ship. Daytime shortwave heating and subcloud evaporation of drizzle both influence the diurnal cycle of boundary layer stability. Solar radiation increases stabilization by balancing (to a degree but not completely) the combination of LW cloud top cooling and evaporative cooling from cloud top entrainment (Wood 2012; Turton and Nicholls 1987). It takes very little solar heating to significantly reduce boundary layer mixing. In fact, Duynkerke (1989) demonstrated that solar radiation can significantly reduce boundary layer coupling shortly after sunrise and that the effect can persist until sunset. The subcloud evaporation of precipitation has also been suggested to increase subcloud boundary layer stability. Negatively buoyant parcels cooled by evaporation mix with ambient air and sink to their level of neutral stability. The presence of these neutral parcels in between the cloud and ocean hinders boundary layer coupling (Wang and Wang 1994; Bretherton and Wyant 1997; Wang and Feingold 2009; Burleyson et al. 2013).

Fig. 4.15 shows the diurnal trend in areal average rain rates within 15 km range of the ship plotted against coincident sounding-derived dry Brunt-Väisälä frequency in the layer from the surface to just beneath the median cloud base. From these figures we can see that more stable conditions in the subcloud boundary layer are associated with two factors: daytime shortwave heating of the stratocumulus layer and increased rain within 15 km of the ship. The soundings taken through a density current (marked with an enclosing circle) and through the prefrontal environment of a density current (marked with an 'x' through the data point) are associated with higher local areal average rain rates, stable conditions ($N^2 > 1 \times 10^{-5}$ s^{-2}), occurring both by day and by night. The soundings collected overnight (blue colors) exhibit a trend of increasing stability with increasing areal rain rates above 0.5 mm d^{-1}. Notably, once areal rain rates exceed 0.5 mm d^{-1}, unstable conditions are not present during either day or night.

The relationship among density currents, increasing rain rates, and increased subcloud boundary layer stability suggest a somewhat counterintuitive conclusion. Density currents are closely associated with *both* more intense precipitation and more stable boundary layers. The development of a stable layer below cloud suggests two explanations for the late morning peak in density current occurrence (see Figs. 4.13 and 4.14). First, the stable layer reduces the transport of surface moisture into the subcloud layer. A drier subcloud layer more readily evaporates drizzle and leads to stronger and more frequent density currents. Subcloud drying may be enhanced by solar warming of the stratocumulus layer after sunrise, further extending the density current peak into the morning as drizzle frequency rapidly wanes. Second, density currents could be providing an alternative vertical moisture transport mechanism via lifting that penetrates the subcloud stable layer along their frontal boundaries. Drizzle cells which support density currents would have a higher probability of maintaining inflow of near surface moisture within the more stable early morning and daytime boundary layer, than drizzle cells without density currents. Future work examining the bulk statistics of the diurnal cycle of drizzle cell shape, lifecycle, or organization may therefore provide additional evidence for the significance of density current frontal boundary lifting as a moisture transport mechanism.

VIII.   Estimating Density Current Propagation Speed

The association of density currents with near surface temperature drops, wind shifts, and pressure increases has been well documented in previous studies of atmospheric density currents. For a Boussinesq fluid, the theoretical density current propagation speed is readily derived via energy conservation and is proportional the strength of the density anomaly across the front and the flow depth:

$$C_{theory} = Fr\sqrt{g'h} \qquad\qquad (4.1)$$

where $g' = g\frac{\Delta\rho}{\rho}$ is reduced gravity, h is the density current depth, and Fr is the Froude number. The

Froude number represents the ratio of inertial and gravitational forces acting within the flow. It can be

used to summarize a number of factors that affect density current propagation speed. These include

atmospheric stability, surface friction, viscosity, the boundary layer depth relative to the depth of the

flow (i.e. normalized height of "the lid" of the system), and entrainment of overlying fluid into the

flow via mixing. For calculation of $C_{theory,}$ Fr was set to 1.

For this study, we derived C_{theory} by calculating g' from ship air density across the front and

core of each density current and by estimating h from the wind anomaly observed in the lidar VAD

profiles. The wind anomaly profiles were calculated from the difference in u and v wind components

between the VAD taken within the front or core and the VAD which most immediately preceded the

density current (approximately 20 minutes prior to the density current VAD). Fig. 4.16a demonstrates

the technique for determining h from the VAD wind direction anomaly profiles during an example

density current event. At the heights corresponding to the main flow of the density current (0-300

meters), the direction of the wind anomaly is roughly constant. At the top of the main flow (~300

meters), the wind perturbation begins to turn, consistent with the presence of an overlying return

circulation/drizzle cell inflow. We recorded the height at which this directional transition occurs as

the density current depth, h. The corresponding pattern in wind speed anomaly is shown in Fig.

4.16b. Above the surface Ekman layer (~100 meters), the wind speed anomaly decreases with height,

reaching a minimum at a height corresponding to h. Wind speed perturbations at heights above h

were variable but consistently smaller on average than those within the main flow present below h.

When speed shear and directional shear estimates of h differed by less than 100 meters, the average

of the two estimates were used to determine h. In 2 out of 34 cases the difference was greater than

100 m, and the height of the directional shear anomaly was used.

Observed density current propagation speed (C_{obs}) was estimated using the maximum ship wind anomaly measured within the front and core zone of each density current. The ship anemometer data were used since there were large uncertainties inherent in determining propagation speed based on radial Doppler velocities and frontal boundary locations within lidar ppi scans. The background flow was estimated using the average wind components measured during the 10 minutes prior to the arrival of the front. This background wind estimate will have varying error depending on the presence or absence of other processes that produce wind anomalies near the surface including: previously deposited cold pools, nonhydrostatic pressure gradients that slow and turn the winds immediately in advance of the front (Charba 1974; Wakimoto 1982), gravity waves or bores propagating through the subcloud stable layer out ahead of the advancing density current, and any turbulent or mesoscale flows that are unrelated to density currents. The wind anomaly relative to the background flow was calculated for each 1-min wind measurement within the front and core of the density current. The propagation speed was estimated using the maximum 1-min wind anomaly for each density current. The maximum value was in all cases located a distance of 3 km or less behind the frontal boundary. However, this maximum value is unavoidably an overestimate of propagation speed because, in addition to the main density current flow, the maximum wind anomaly includes winds resulting from turbulent eddies present at surface. One technique for reducing the estimate of observed propagation speed is to use the average wind anomaly over the entire duration of the density current front. However, the propagation of the frontal boundary is driven by the deepest and strongest horizontal density gradients, which are found across the head of the density current. As a result, averaging winds over several kilometers behind the front reduces the correlation of the observed estimate to theoretical measures of front propagation speed.

Fig. 4.17 plots the estimated C_{obs} against the theoretical propagation speed derived using equation 4.1. The estimated C_{obs} was reasonably correlated (R = 0.66) with the propagation speed

expected from theory. Sources of error in this analysis originate from uncertainties in estimates of the wind anomaly behind the front (± 1 ms^{-1}) and density current depth ($+100$ m). Additionally, two factors may contribute to an underestimate of h. First, the h estimate was obtained at whatever point within the front and core zone that the lidar collected the VAD and may not have been at the deepest point. Second, the return flow above the main flow of the density current, which can be within the cold air anomaly, is not included in our estimate of h. Unsurprisingly, the combination of a likely underestimate of h and a likely overestimate of C_{obs} yields Froude numbers ($\overline{Fr} = 1.24$) that are higher than the expected values ($Fr \approx 0.75 - 1$) for density currents (Wakimoto 1982). Given the limitations of the data set, we cannot rule out gravity waves or bores.

Behind the front of a density current, we expect to see a hydrostatic high pressure area, which drives the forward propagation of the front. The pressure change across the front and core of each density current was poorly correlated with estimated C_{obs} (not shown). This poor correlation is likely a result of uncertainties in estimation of C_{obs} and the fact that the density currents are occurring in a non-quiescent, non-uniform background environment.
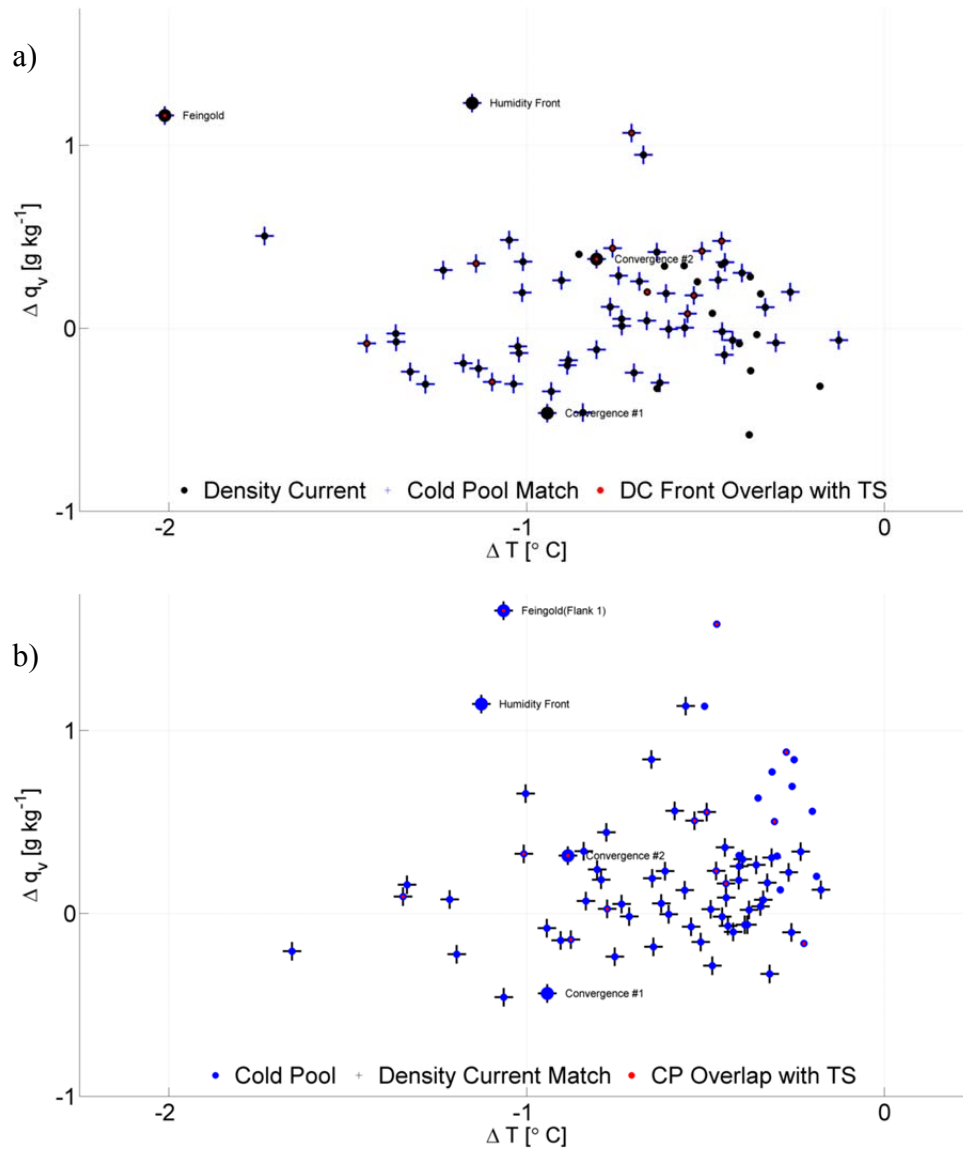
Fig. 4.1: The change in vapor mixing ratio (q_v) vs. the change in temperature observed from a) the start of the density current front to the end of the density current core b) start and end of the cold pool edge. Density currents that were also identified as cold pools are marked with a blue hatch and cold pools that were also identified as density currents are marked with a black hatch. Inset red dots indicate when a temperature spike rebound overlapped with the density current front or cold pool edge, respectively. Density currents examined in the case study analysis presented in Chapter 3 are annotated.
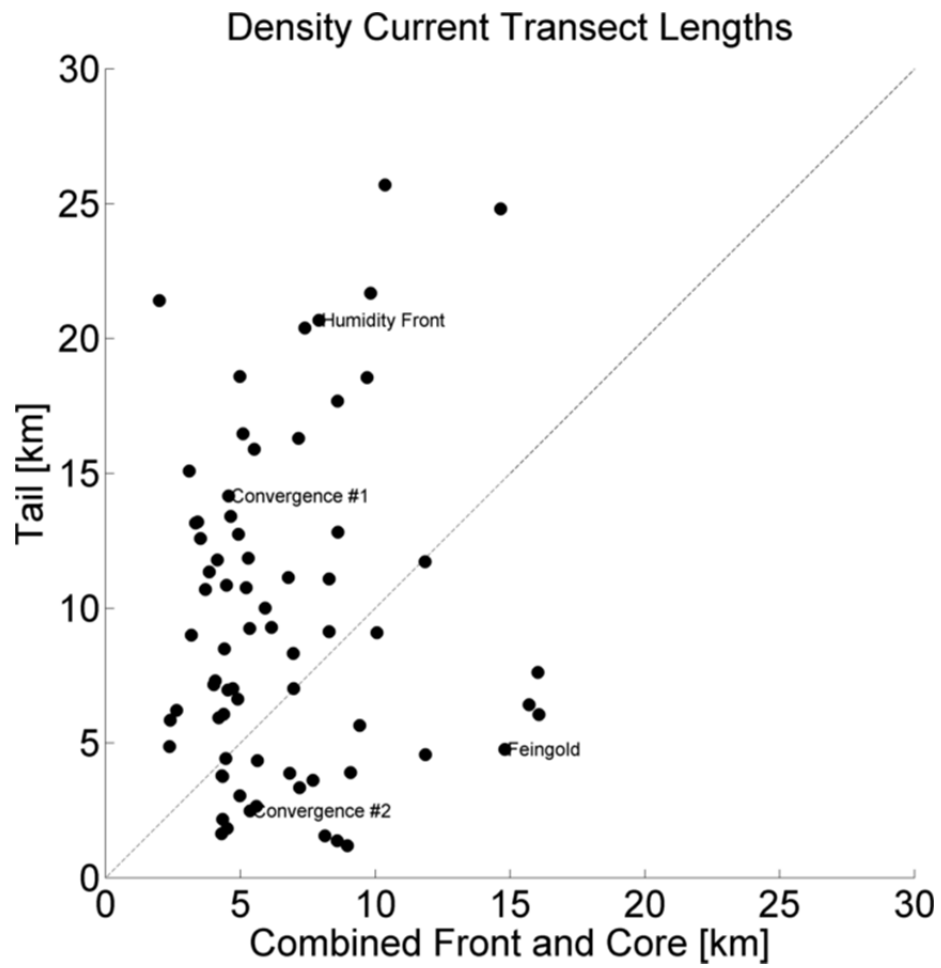
Fig. 4.2: Ship transect lengths through the surface wind field within the front and core regions vs. the transect lengths through the tail regions of each density current.
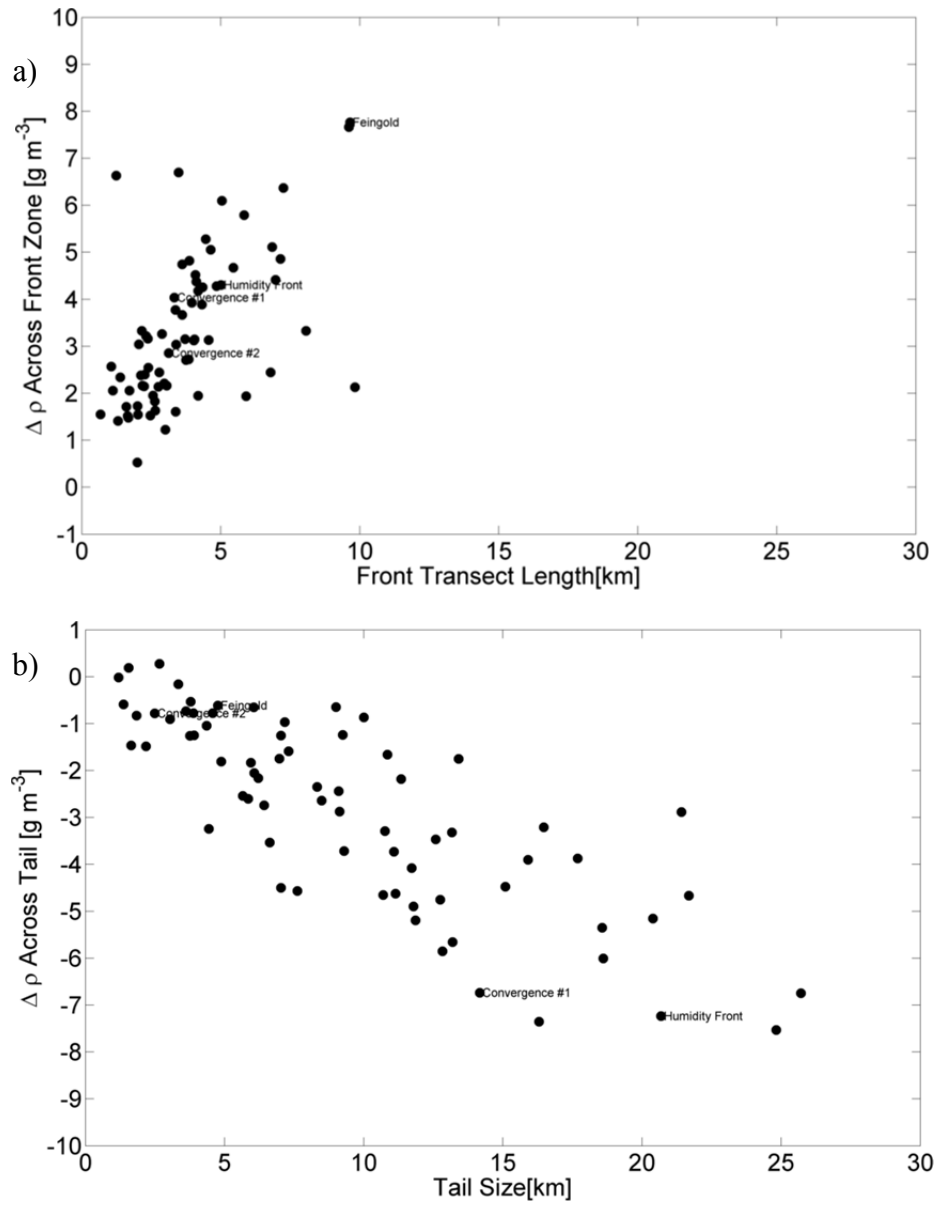
Fig. 4.3: a) Front zone transect lengths and b) tail zone transect lengths vs. the change in density observed over the zone.
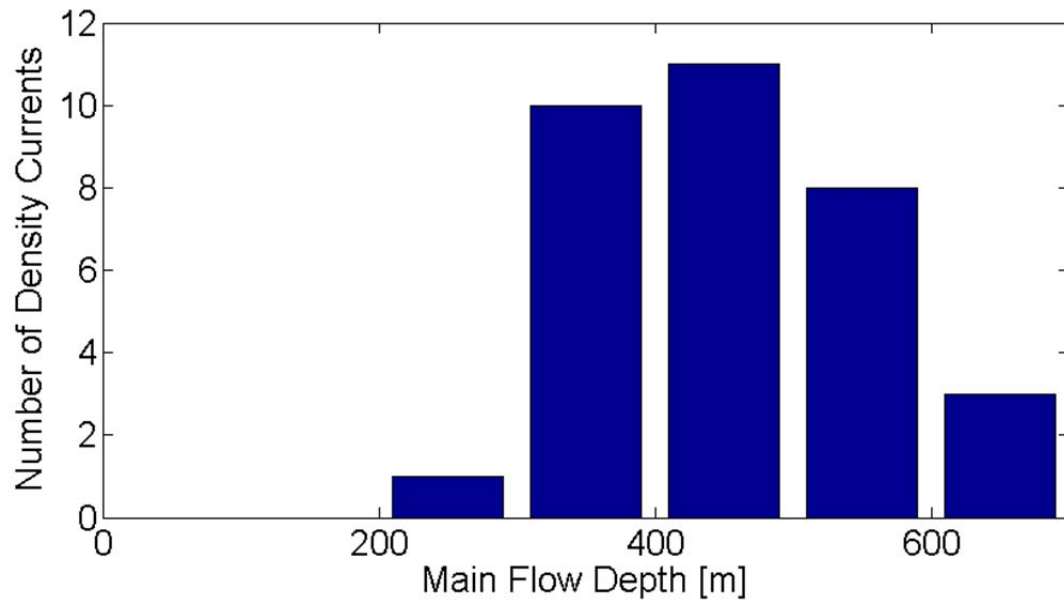
Fig. 4.4: The maximum observed depth of the main layer of horizontal flow associated with 33 density currents observed in lidar rhi scans.

Fig. 4.5: Composited upward-pointing lidar images taken as a density current front passed over the ship at x=0. Each row shows data acquired during the passage of a unique density current. All data available within 10 minutes of the start of the front are shown for context. Backscatter intensity values above 20 dB indicate cloud. Radial velocities (right column) are red within updrafts, and blue within downdrafts. Density current case studies the density currents associated with the cloud features shown in Fig. 4.6 and Fig. 4.8 are annotated on the right.

Humidity Front

Feingold

Convergence #1
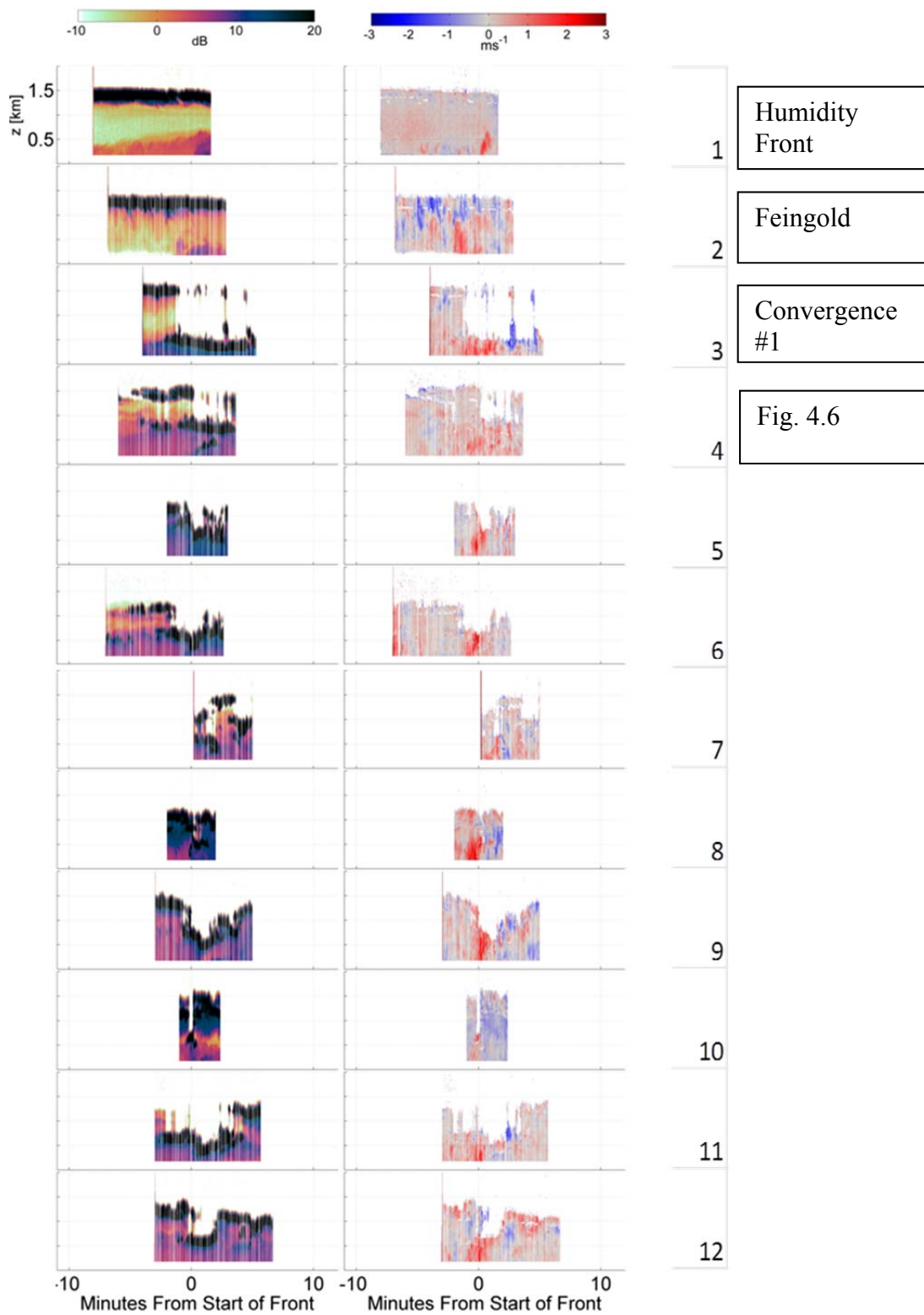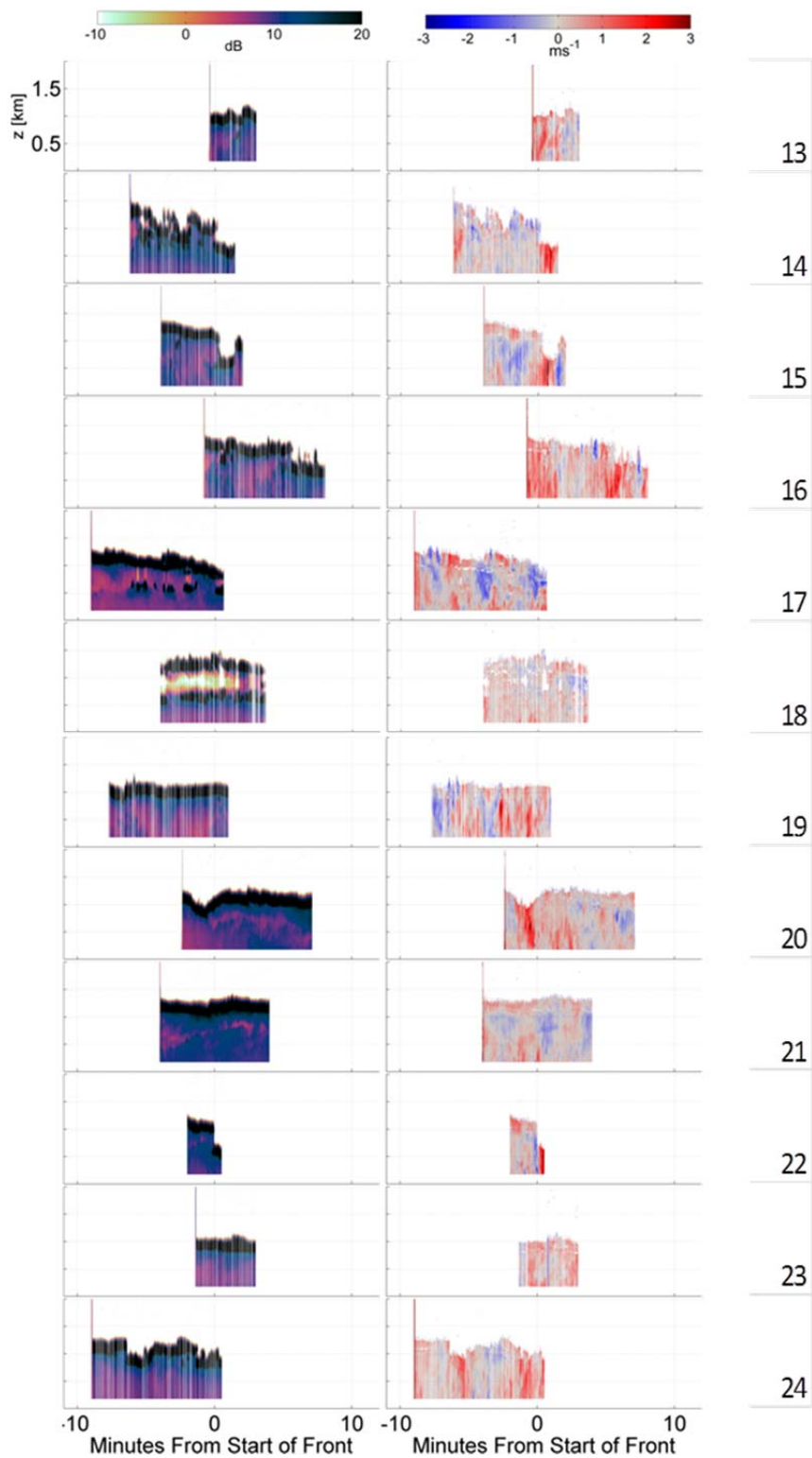
Fig. 4.6

Fig. 4.8
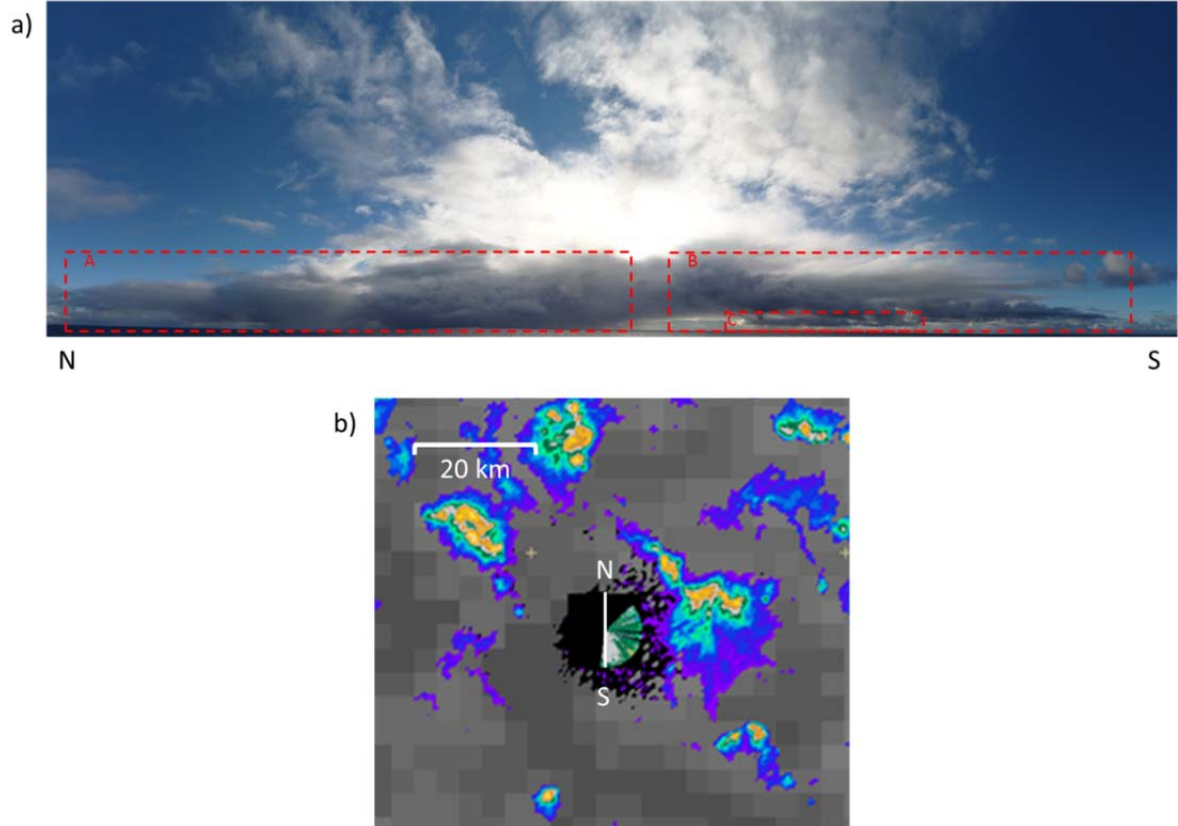
Fig. 4.6: a) Panoramic photograph taken across the bow of the ship from N (left edge) to S (right edge) at ~1205 GMT on 27 October 2008. A density current crossed the ship from the east southeast at 1213 GMT. Boxes indicate cumulus formations in the mid-levels adjacent to the main drizzling regions (A); mid-level cumulus bands trailing the main drizzling region (B); very low level (<300 meters altitude) cumulus forming along the top of the main density current flow (C) b) Corresponding C-band radar scan with the lidar ppi mean wind corrected velocity data superimposed within 6 km range of the ship. The white line indicates the field of view of a).
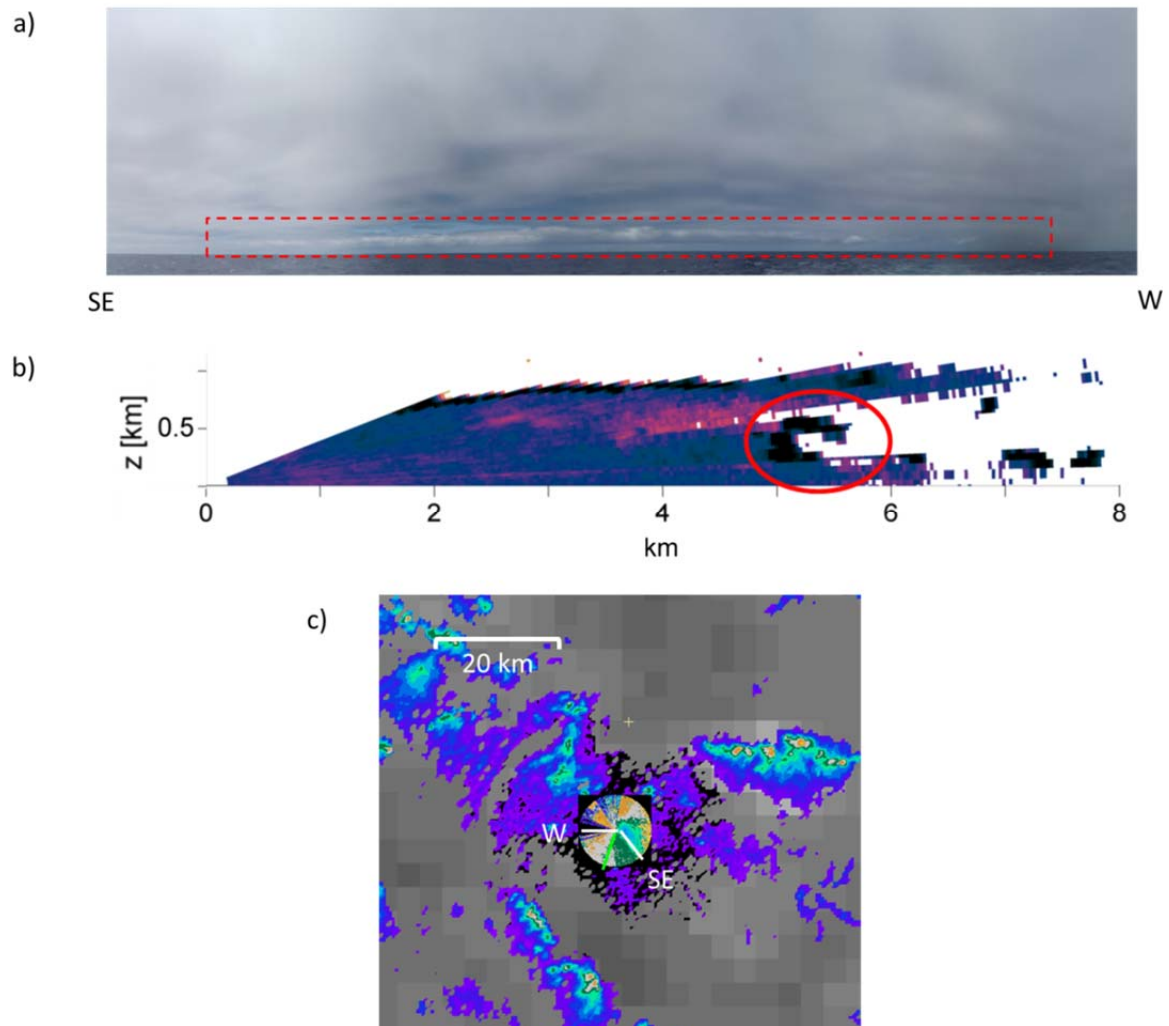
Fig. 4.7 a-c: a) Panoramic photographs taken across the starboard and stern of the ship from the SE (L) to the W (R) at ~1605 GMT on 28 October 2008. The red box outlines the linear subcloud cumulus structure seen along and directly above the density current front that approached from the east and southeast and crossed the ship at 1544 GMT. b) Lidar rhi taken at 190^0 azimuth that captures the cloud structure seen in a) (red circle) between 250 meters and 500 meters altitude. c) Corresponding C-band radar scan with the lidar ppi mean wind corrected velocity data superimposed within 6 km range of the ship. The white line indicates the field of view of a). The green line indicates the azimuth angle at which b) was taken.
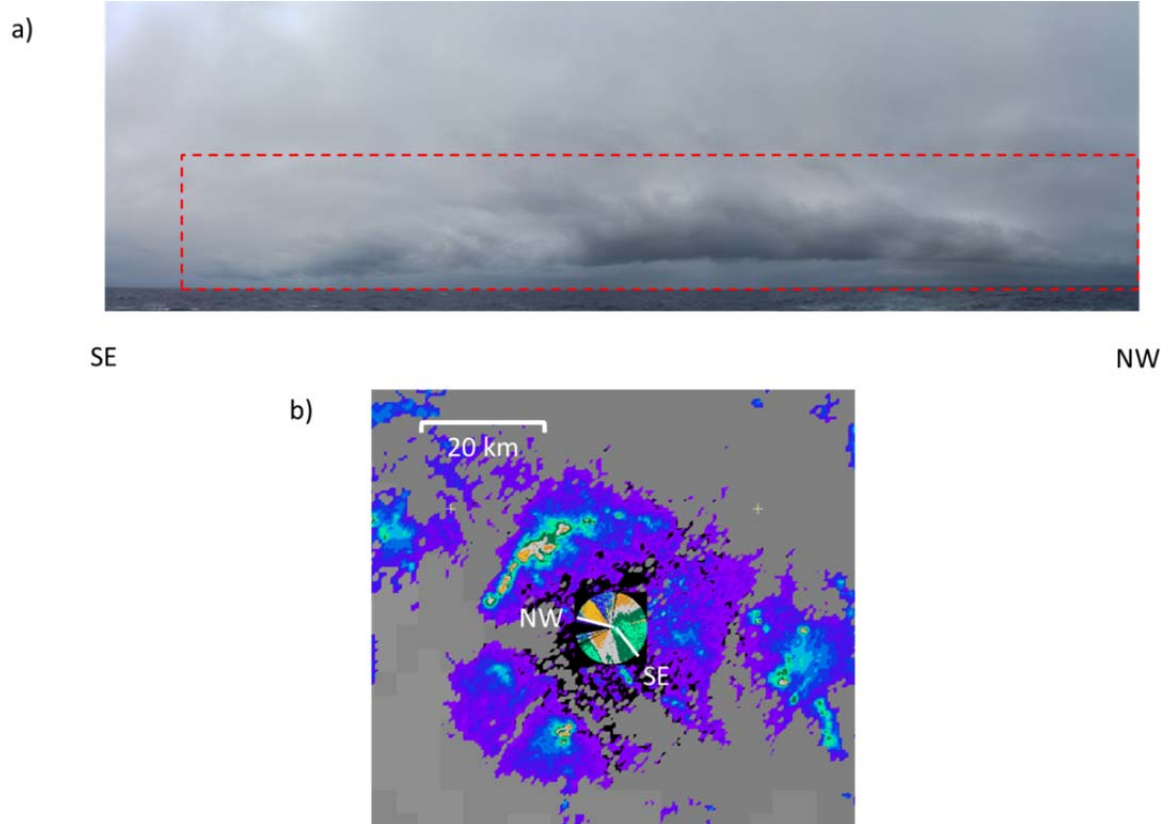
Fig. 4.8a-b: Panoramic photographs taken across the starboard and stern of the ship from the SE (L) to the NW (R) at ~1405 GMT on 29 October 2008. The red box outlines the linear subcloud cumulus structure seen along and directly above the density current front that approached from the east and crossed the ship at 1353 GMT. b) Corresponding C-band radar scan with the lidar ppi mean wind corrected velocity data superimposed within 6 km range of the ship. The white line indicates the field of view of a). The radar confirms that the linear cloud feature is drizzling, which is visible along a line winding to the south and southeast of the ship.
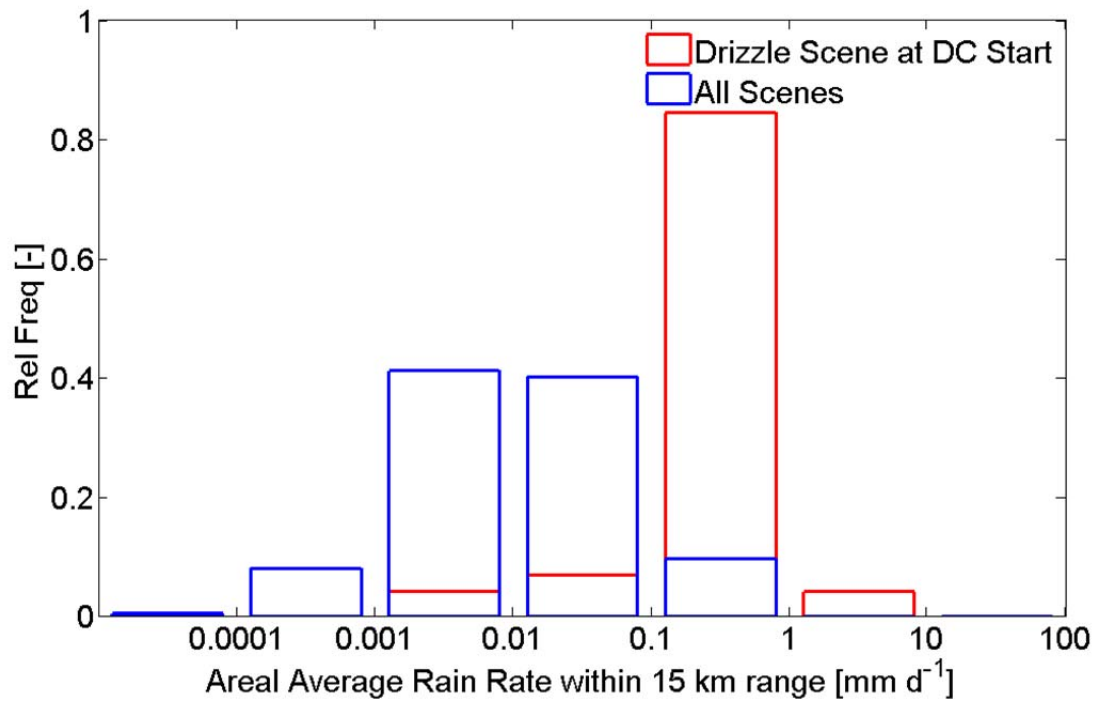
Fig. 4.9: Relative frequency distribution of areal average rain rates within 15 km of the ship. The distribution all drizzle scenes throughout the 30 day data set (24 October 2008 through 2 November 2008 & 11 November 2008 through 29 November 2008) is shown in blue, and the distribution for drizzle scenes within 3 minutes of the start of a density current is shown in red.
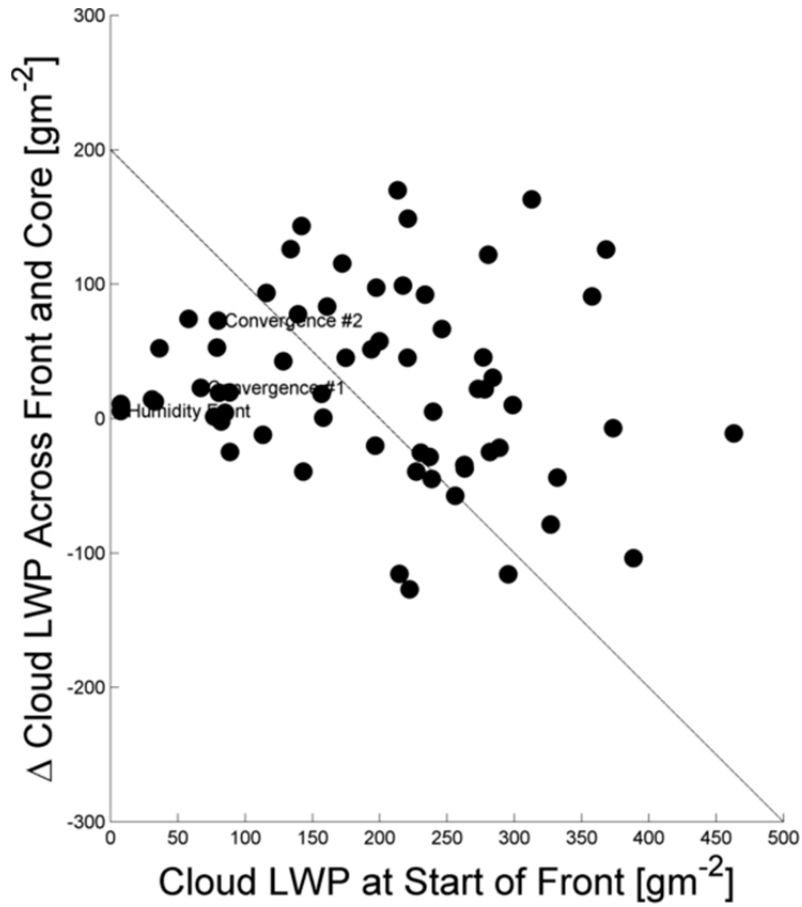
Fig. 4.10: Ten minute averaged cloud liquid water path (LWP) over the ship at the start of density current fronts vs. the change in cloud liquid water path observed across their front and core zones. LWP > 200 g m^{-2} is a proxy for moderate to heavy drizzle. The dotted line corresponds to a cloud liquid water path of 200 g m^{-2} at the end of the core zone.
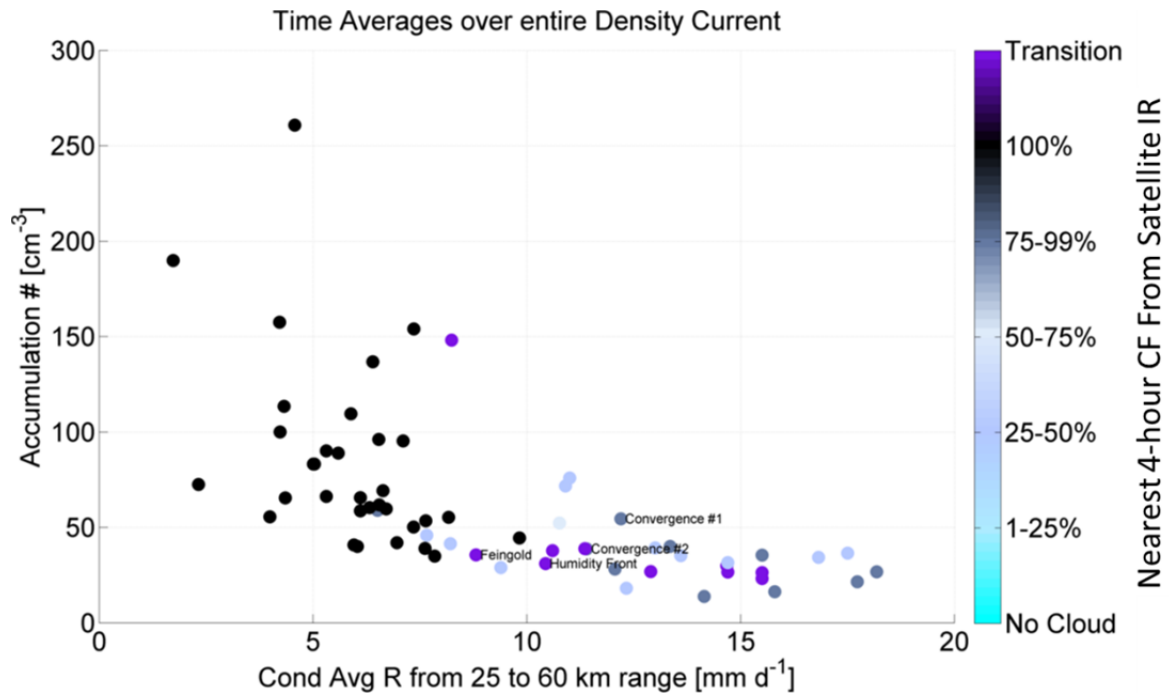
Fig. 4.11: Conditional average rain rates from 25 and 60 km range vs. accumulation mode aerosol number concentrations averaged over the duration of each density current. Color coding indicates the nearest 4-hourly satellite-IR derived cloud fraction in the region surrounding the ship for the start of the density current. Times when the cloud fraction was rapidly changing (purple) indicate a region of open-closed cell transition.

a)

b)

c)
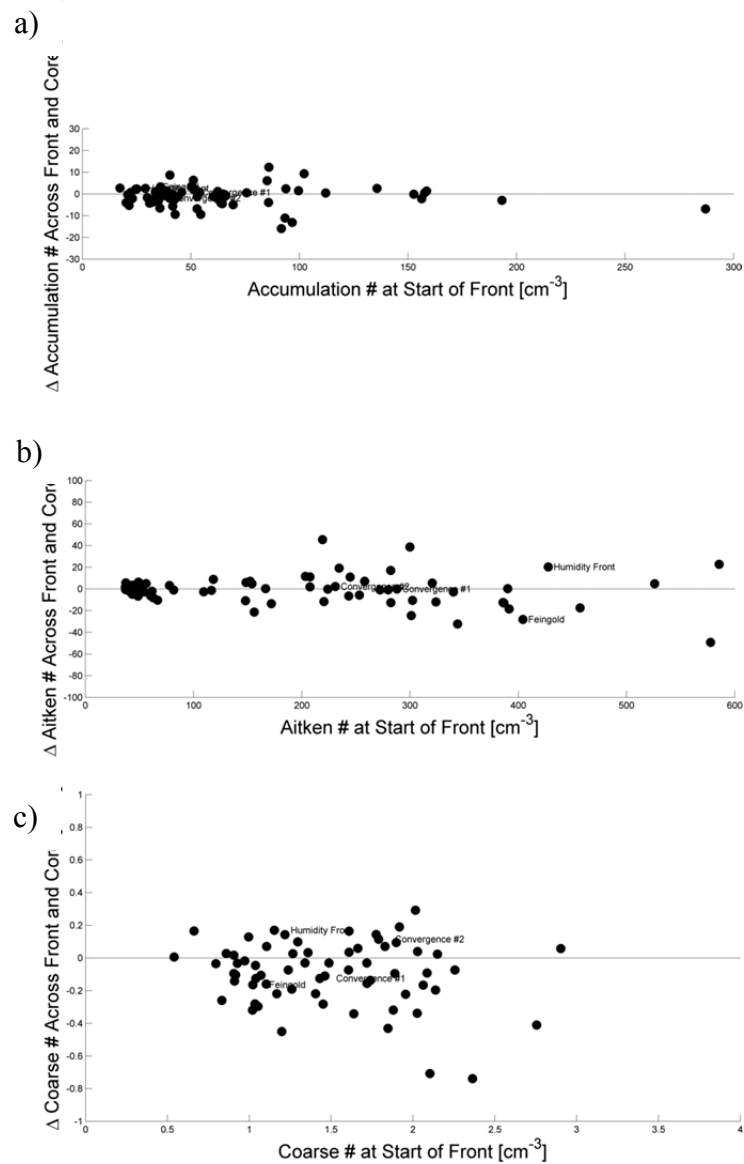
Fig. 4.12: Aerosol number concentrations at the start of density current fronts vs. the change in aerosol number concentration observed across their front and core zone for particles in the a) accumulation mode b) Aitken mode and c) coarse mode.
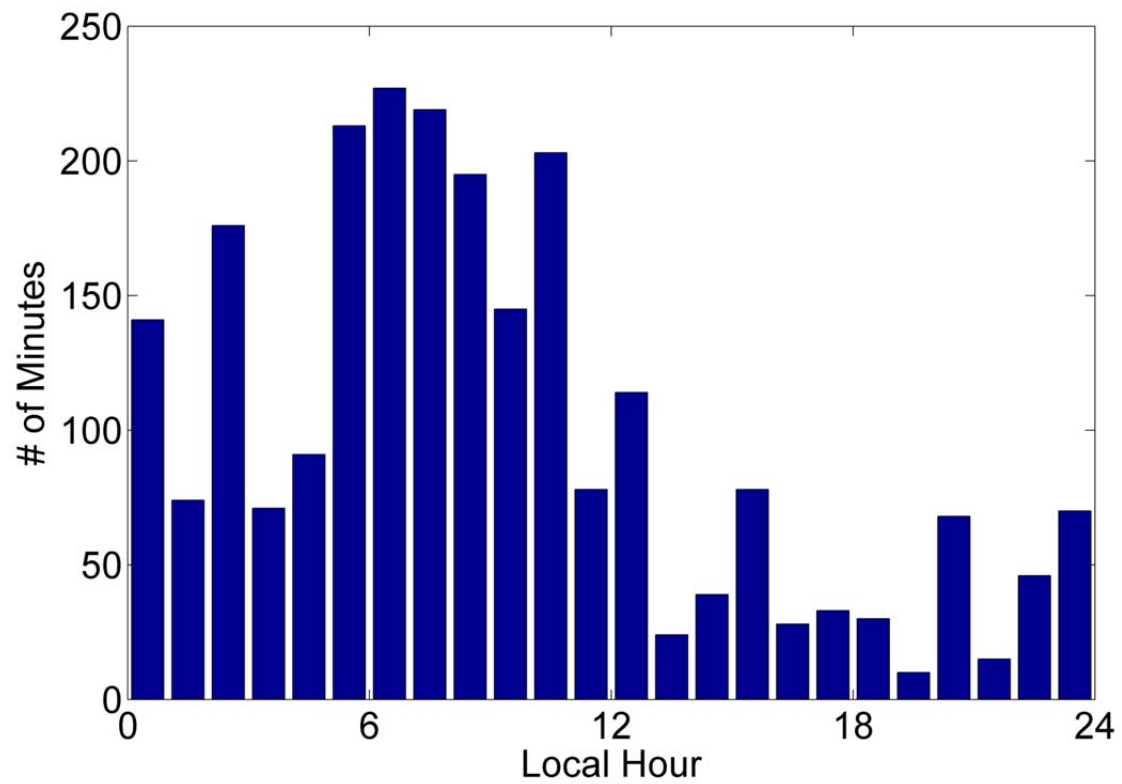
Fig. 4.13: Diurnal cycle of density current occurrence over the ship. All minutes when a density current was observed over the ship is binned into the corresponding local hour to produce the distribution.
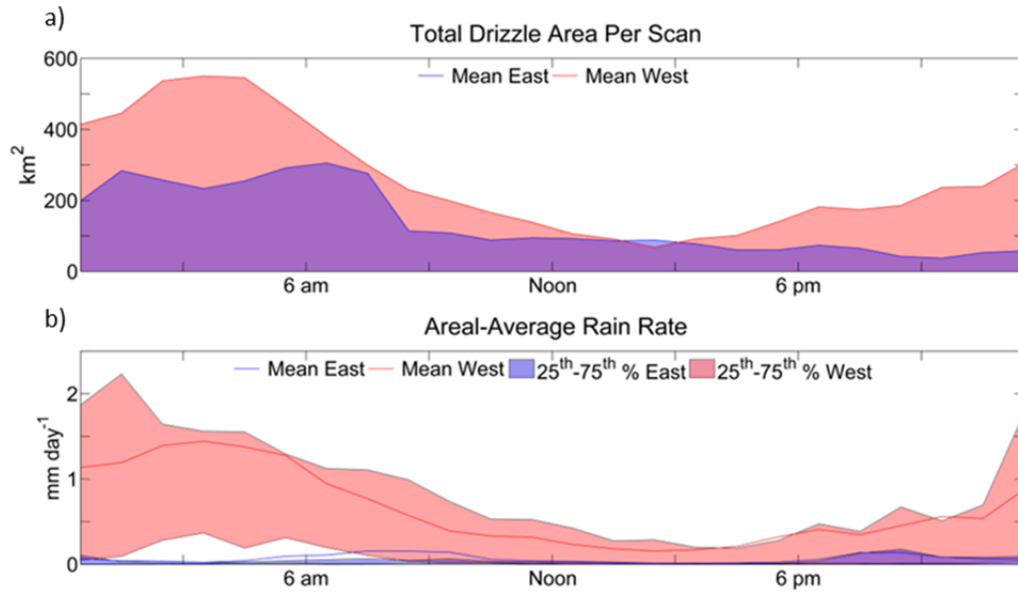
Fig. 4.14 a,b: Diurnal variation of the mean total precipitation area per scan (a), mean (solid line) and interquartile range (shaded region) of the hourly areal-average rain rate (b), derived from measurements from the scanning C-band precipitation radar aboard the *RHB*. Adapted from Burleyson et al. (2013), their Fig. 8b,c.
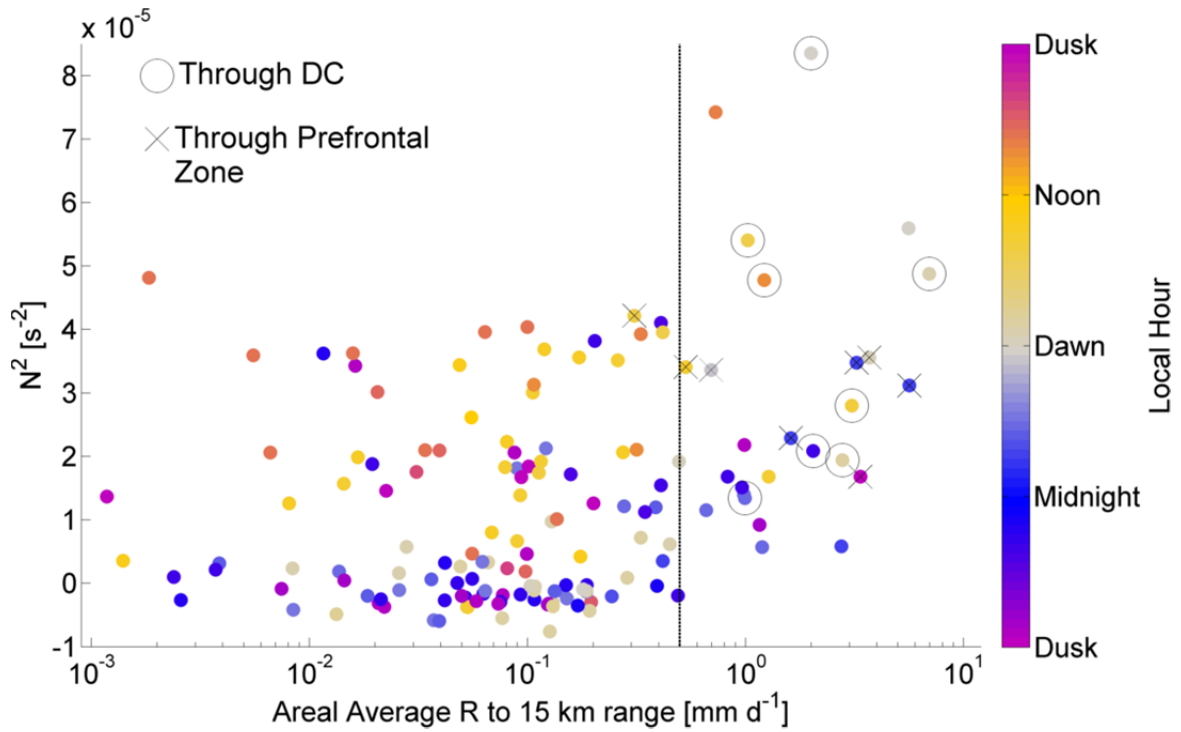
Fig. 4.15: C-band radar derived areal average rain rates within 15 km range of the ship vs. the square of sounding-derived dry Brunt-Väisälä frequency (N^2). N^2 was calculated across the 100 layer nearest the ocean surface to the 100 meter layer just below the median cloud base. Color indicates local time of day. An 'o' marks soundings launched through a density current. An 'x' marks soundings launched less than 30 minutes prior to a density current front passage over the ship. As radar reflectivity near the ship is affected by sea clutter, data points to the right of the vertical dotted black line indicate areal average rain rates that we are most confident indicate moderate or intense drizzle.

116
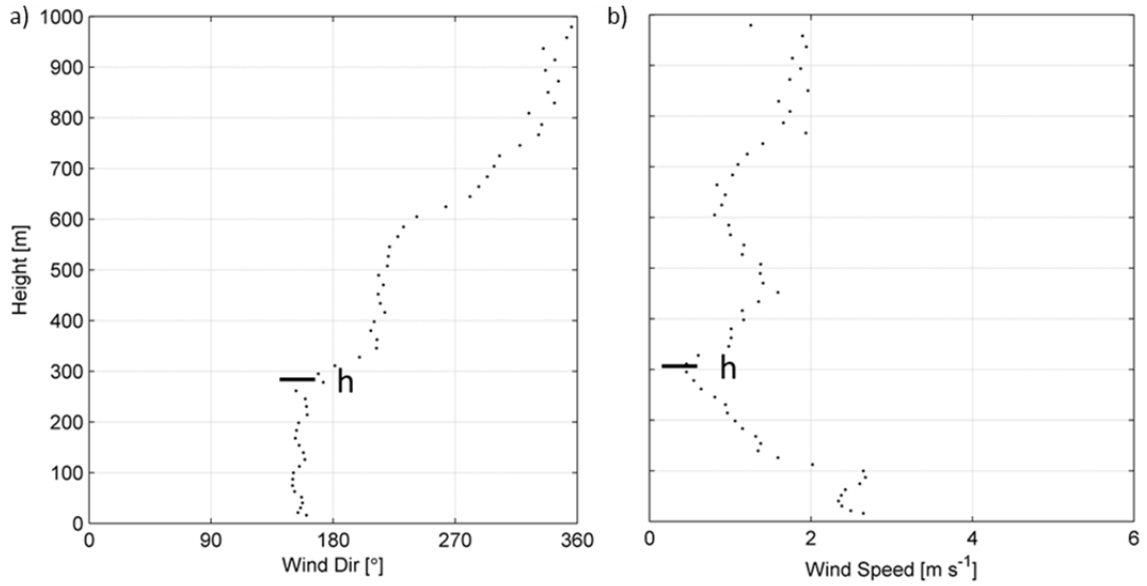
Fig. 4.16: Example VAD wind anomaly direction (a) and speed (b) through the frontal zone of a density current taken at 1624 GMT on 26Oct2008. The wind anomaly was calculated by subtracting the components of the wind measured at each height during the preceding VAD scan, taken at 1604 GMT. The density current front crossed the ship during the interim between the two scans (1618 GMT). Density current depth (*h*) estimates for this scan are marked with a black line at ~300 meters height.

Fig. 4.17: Maximum 1-minute ship wind anomalies within the front and core region (C_{obs}) of 34 density currents as a function of theoretical gravity current propagation speed (C_{theory}). Theoretical propagation speed was calculated via equation 4.1 using VAD derived density current depth estimates, ship-level density perturbations across each front, and a Froude number (Fr) of unity. The dashed line indicates perfect agreement between observed and theoretical propagation speed for an ideal critical flow (Fr =1). Vertical error bars represent a ± 1 ms^{-1} uncertainty in the estimation of maximum ship wind anomaly. Horizontal error bars represent the increase in theoretical propagation speed for a 100 meter increase in density current depth.

CHAPTER 5

Synthesis Diagrams of Drizzle Outflow Structure

I.   Vertical Structure of Density Current in a Less-Coupled Boundary Layer

Fig. 5.1 shows an idealized schematic diagram of a vertical cross section through a drizzle-induced density current flow structure along its axis of propagation. This density current is moving from right to left and is situated within a less-coupled marine stratocumulus boundary layer. Representative moisture (RH) and virtual potential temperature profiles (θ_v) within a less-coupled boundary layer are provided. Moving up from the ocean surface, virtual potential temperature decreases up to ~100 meters height, which roughly corresponds to the height of the surface layer. This layer is dominated by air-sea interactions between the comparatively warmer ocean surface and is generally slightly unstable. Any residual cold air left behind by a previous density current may also increase the negative gradient of θ_v through this layer. Above the surface layer, virtual potential temperature levels off until it reaches a stable layer (here, ~750 meters height) which corresponds to the height of the surface mixed layer. Because the lifting condensation level (LCL) height is often located near the height of the surface mixed layer, small and patchy subcloud cumulus may form along the top of the surface mixed layer. Above the surface mixed layer is a layer that we have generically termed the 'mixed layer', which is separated from the surface mixed layer by the stability boundary and consequently is drier and cleaner than the surface mixed layer (Wood 2012). For this reason, there tends to be reduced lidar backscatter intensity within the mixed layer.

Mechanical lifting of prefrontal air associated with high pressure adjacent to the frontal zone of the density current is indicated by the large, bent black arrow in Fig. 5.1. Along and near the path of the lifted prefrontal air, extensive cloud formation is observed often well above the main density

119

current flow, often forming shelves or arcs, and may extend to the base of the stratocumulus deck. The main flow of the example density current is located in the right half of Fig. 5.1 from the surface to 400 meters height. The main flow exhibits some of the key structural features seen in well-defined density currents. The frontal zone arcs backward with up to the maximum depth of the flow from the prominent nose found within 100 meters of the surface. The trailing vortex directly behind the head draws in air from above the main flow and reduces its depth. Behind the trailing vortex the height of the main flow levels off and gradually descends.

The wind profile through the core of the density current is shown on the righthand side of Fig. 5.1 and it captures the maximum winds associated with the main density current flow below 400 meters. Drag forces reduce the wind perturbation in the lowest ~100 meters of the main density current flow, causing some shear across this layer. The rightbound return flow, which is induced by dynamical pressure perturbations along the front, is located between ~400 meters and ~800 meters height. The shear present across this layer generates turbulent eddies which over time tend to mix out the main density current flow and contribute to dissipation of the associated temperature and density perturbation. The mixing in this layer in turn may transport moisture and aerosol upwards. Furthermore, parcels lifted by the turbulent motions cool and may approach saturation, causing hygroscopic growth of aerosol. The combined result of these effects is to extend the depth of the zone of increased lidar backscatter intensity through much of the shear layer (here, up to ~900 meters). The turbulent motions behind the frontal zone may also generate subcloud cumulus over the top and within the main density current flow, some of which are very low-lying (<400 meters). The reasons that clouds form much lower here than in the prefrontal zone is that the air within the density current is cooler and has a higher relative humidity than the near-surface air in the prefrontal zone, and therefore has a lower lifting condensation level (LCL) height.

II. Horizontal Drizzle Outflow Structure

Fig. 5.2 shows an idealized schematic diagram of the horizontal structure of an isolated drizzle outflow complex. This outflow complex can be thought of as the kinematic description of a mature drizzle-induced cold pool. In this model, the source drizzle cell has persisted for some time with approximately the same shape and intensity. The drizzle cell is advected with the southeasterly mean cloud layer winds ($\overline{U_{cl}}$).. Mean near-surface winds are also traveling in approximately the same direction as the cloud layer in this model, but at a reduced speed. Successive outflow pulses that comprise the outflow complex propagate out roughly orthogonally from the boundaries of the drizzle cell core at any given time. A region of lighter drizzle surrounds the drizzle cell core from which the outflow emanates. This pattern is consistent with radar observations. These peripheral low reflectivity regions can be quite extensive and likely contribute to the anvil structure seen in cloud photos (e.g. see Figs. 4.6, 4.7, 4.8). In this schematic, the region of lighter drizzle is extends towards the back of the drizzle cell (e.g., as in Fig. 4.6), although it may also be present along other sides of the drizzle cell core.

Despite the fact that the drizzle cell core is roughly circular, the outflow structure itself is however not circular. In fact, a key feature of the outflow complex's overall shape is its elongation about an axis roughly parallel to the mean wind. Another characteristic of the outflow structure is the fact that it grows wider behind the drizzle cell before it tapers off at the end. This overall oblong, comet-like shape is a result of two factors. The first is the fact that wind speeds in the cloud layer are higher than near the surface. This means that the drizzle cell overtakes the successive outflow pulses that it creates, essentially depositing the outflow pulses in its wake. The resulting outflow complex is extended along the track of the drizzle cell that produced it. A second reason for the shape of the outflow complex is the horizontal near-surface flow perturbations associated with the outflow pulses

121

and how those perturbations evolve over time. The overall outflow complex is being advected by the mean near-surface wind. However, the horizontal wind perturbations within the outflow structure are divergent and this leads to deformation of the outflow complex. To the left and right of the drizzle cell track, the outflow complex is bounded by density currents propagating orthogonally to the drizzle cell track in opposite directions to one another. Older outflow pulses have had more time to travel farther to the right and left than the newer outflow pulses. This is the reason that the outflow complex becomes wider behind the drizzle cell. Over time, the density currents travelling orthogonally to the drizzle cell track gradual dissipate and stall out, because they are no longer being replenished by freshly deposited outflow pulses. This is the reason that the right and left boundaries of the outflow complex gradually become less curved behind the drizzle cell. Between these two density current bands, lies the region of the outflow complex corresponding to the tail zone of *both* the right and the left density current bands. Compared the front and core zone of a density current, the density anomalies and flow depths within the tail zone are smaller. For this reason, the tail zone spreads out more slowly. As you move inwards from the front and core zones of the density current bands and into the tail zone, the wind perturbations slacken and gradually turn *against* the mean wind. This is because the near-surface air within the tail zone remains relatively cool, which stabilizes the near-surface layer. Drag forces therefore become increasingly dominant towards the center of the tail zone, and tend to reduce wind speeds there.

A typical ship transect through the outflow complex is also shown in Fig. 5.2 to illustrate how density current front, core, and tail zones were sampled by the ship. The ship transect is angled towards the direction of the mean near-surface wind flow. This is because ship-relative winds were within 80^0 of the bow during times when a density current was identified, and rarely exceeded 60^0. Because the ship therefore travelled through the long axis of the outflow complex, it tended to sample

an extended tail zone—as evidenced in Fig. 4.2. This fact also explains why sharp jumps in density were not commonly observed at the terminating end of density current tails. The drizzle outflow complex does not have a well-defined 'backside' in this model. The back of the outflow complex is indistinct because the dynamical processes that characterize its forward propagating front, left, and right sides are largely absent there. Instead, the cooler near-surface air at the back end of the outflow complex is being gradually diluted by turbulent mixing from above and below.

A final feature of Fig. 5.2 is the shelf cloud along the drizzle outflow boundary. These clouds indicate condensation associated with mechanical lifting along the active propagating portions of the outflow boundary. The enhancement of convection indicated by the shelf cloud can occur anywhere along the propagating frontal boundaries of the outflow complex. The shelf cloud is likely more extensive in the immediate vicinity of the front edge of the outflow complex where the outflow boundary is stronger and deeper. Additionally, the air forced up and over the outflow boundary may be important for transporting moisture into the drizzle cell core. The path of the pre-outflow near-surface parcels after they are lifted can be described in a manner analogous to RKW theory. The shear profile above outflow boundaries propagating in less-coupled boundary layers would be influenced by three factors. First, there is the circulation generated by the outflow itself, which would tend to draw the near surface parcels along the frontal zone up and back over the density current flow (i.e. the counterflow of the density current itself). Second, there is the mid-level drizzle cell inflow pattern, which results in a shear vector over the top of the outflow which points towards the source drizzle cell. When the outflow boundary is ahead of the cell, the shear vector from the mid-level inflow would therefore be pointed more or less in the same direction as the density current counterflow and reinforce the flow of parcels back over the density current. Finally, there is the preexisting shear profile in the less-coupled boundary layer, which is not generated by drizzle cell circulations. This shear vector generally points in the direction of the mean wind (i.e. wind speed increases with height

up to the cloud layer). Along the front edge of the outflow boundary, the density perturbation is strongest and the density current flow is most closely aligned with the forward track of the active drizzle cell. Moisture transported by the lifting occurring along the front of the outflow complex would be more likely to be drawn backwards and into the updrafts associated with the existing drizzling regions, and may therefore serve to maintain the source drizzle cell (e.g. see Fig. 3.13). Another effect of the preexisting shear profile may be to deepen and speed up density currents present along the front edge of the outflow complex, which would act to enhance frontal lifting and convection along the front edge of the outflow (Liu and Moncrieff 1996).

III. Interactions between Evolving Outflow Complexes

Interactions between distinct drizzle outflow complexes are not shown in Fig. 5.2. This phenomenon was not frequently detected using the methods presented in our study, though it may nonetheless be a factor for mesoscale convective activity in the study domain. Convective initiation would be likely to occur if one outflow complex collides with an outflow boundary propagating out from a new and distinct drizzle cell travelling beside it. This convection would tend to be most vigorous if the collision occurred along the actively propagating outflow boundaries, as was suggested by Feingold et al. (2010). Given the fact that outflow complexes tend to be elongated along the axis of the mean wind however, the left and right propagating outflow boundaries—not the front side—would be most likely to initiate new drizzle cells in this way.

Alternatively, it is possible that convection may be enhanced even if the front of an outflow boundary collides with the stalled, dissipating tail zone of another outflow complex. In order for this to occur, the equivalent potential energy in the boundary layer above and within the dissipating tail zone of an outflow complex would need to be higher than regions surrounding the outflow complex and this layer would need to be lifted (by some mechanism, including possibly by entrainment).

Zuidema et al. (2012) found that this was in fact the case for dissipating cold pools generated by subtropical shallow convection. Fig. 5.3 (bottom) shows their model for cold pool recovery, which indicates greater boundary layer conditional instability over dissipating cold pools. Unlike cold pools generated by convection over land, cold pools over the ocean are provided with a constant source of both heat *and* moisture by the ocean surface below. As a result, the air within cold pools over the ocean would tend to warm and moisten as they dissipate. Furthermore, they transport this moisture to the layers above cold pool through enhanced turbulent mixing. In an analogous manner, the dissipating tail zone of marine stratocumulus drizzle outflow complexes may also be regions in which the boundary layer environment has been primed for new convective activity. This process may have been observed in our convergence case study (Chapter 3). In comparison to the pattern of lifting that was observed over and along frontal boundaries (Fig. 4.5), the convective initiation observed in that case was preceded by at least 10 minutes of sustained, less intense lifting (see Fig. 3.14). This lifting occurred between 25 and 35 minutes after first density current began stall and dissipate and 5-15 minutes before the second density current crossed the ship. Moreover, the ship variables coincident with the lifting (see Fig. 3.15), showed that mixing ratios at the surface rebounded around this time and relative humidity remained very high (~90%). Finally, the upward-pointing and rhi scan from the lidar showed evidence of sustained moistening and lifting throughout boundary layer well in advance of the second density current (Figs. 3.16 and 3.20). A more systematic examination of the interactions between evolving drizzle outflow complexes in the VOCALS-REx study domain, their relationship to the near surface convergence field, and their role in enhancing convective initiation may prove fruitful for future studies.
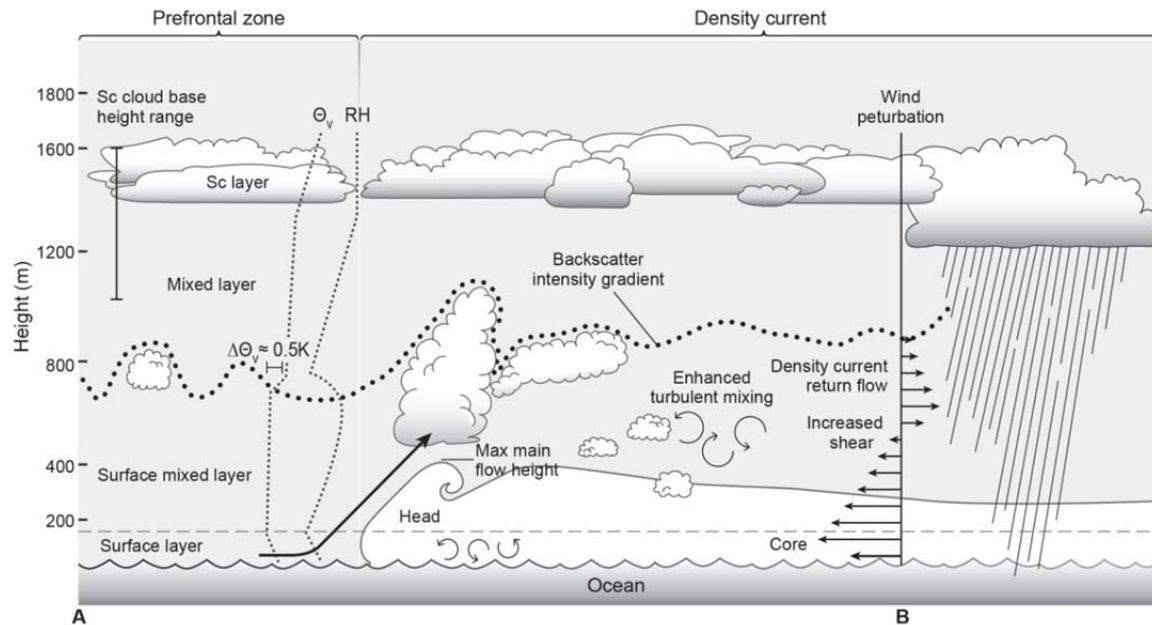
Fig. 5.1: Vertical cross-section along the axis of propagation of an idealized drizzle-induced near surface density current. The density current is travelling from right to left and is situated in a less-coupled stratocumulus-topped marine boundary layer. In the prefrontal zone located to the left of the density current, the constituent layers are annotated. The dotted line indicates the height of the peak vertical gradient in lidar backscatter intensity, which marks the divide between the mixed layer and the surface mixed layer. Profiles of virtual potential temperature (θ_v) and relative humidity (RH) are characteristic of a less-coupled boundary layer. Labels A and B at the bottom of the figure refer to Fig 5.2 and indicate the location of this vertical cross-section within the horizontal layout of the outflow.
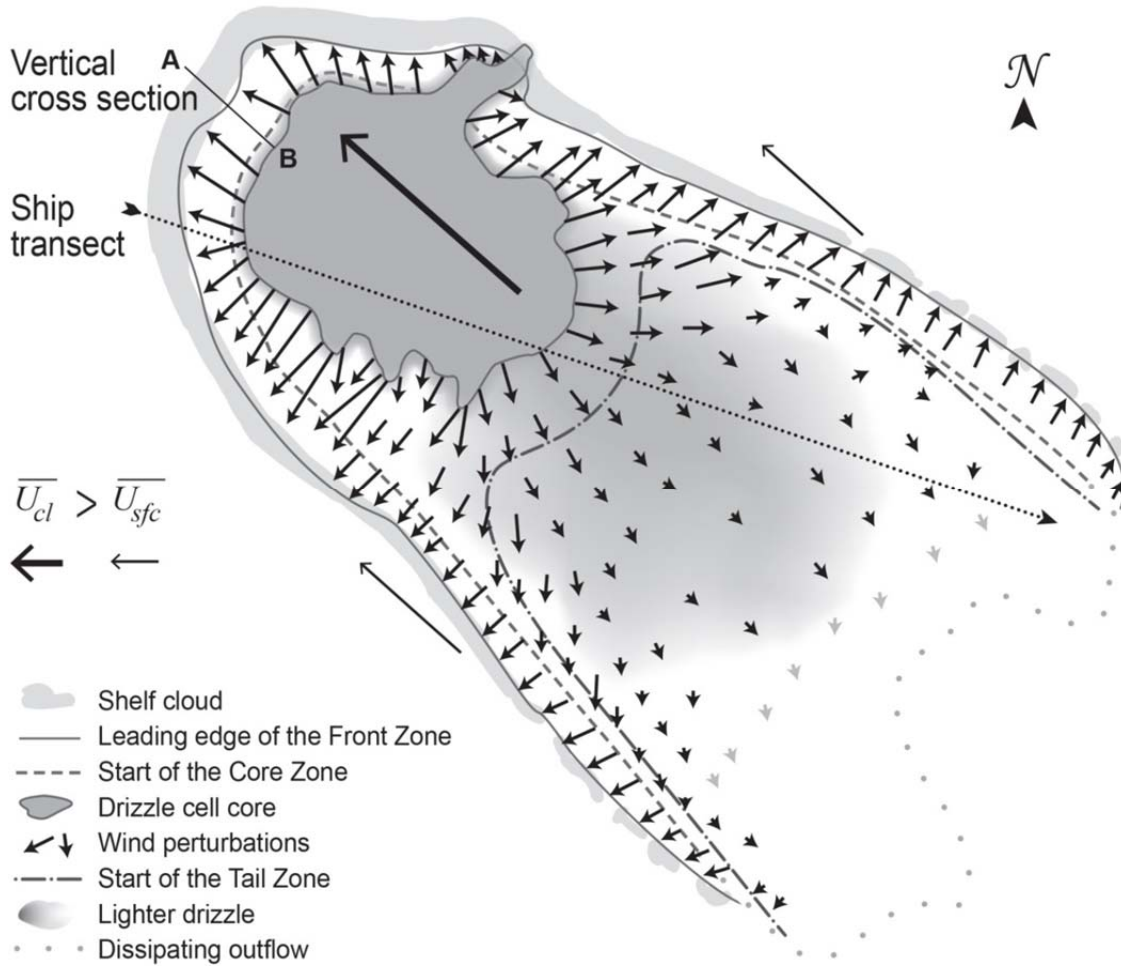
Fig. 5.2: Idealized horizontal flow structure of an isolated drizzle outflow complex. The outflow emanates from the drizzle cell core, which is trailed by a region of light drizzle and virga. A shelf cloud is formed along the outflow's leading edge. The size and orientation of the large black arrows indicate typical wind speed and direction at the surface ($\overline{U_{sfc}}$) and at the cloud level ($\overline{U_{cl}}$) in a sheared boundary layer. The wind perturbations associated with the outflow are relative to $\overline{U_{sfc}}$. A representative ship transect through the outflow illustrates the location of density current front, core, and tail zones detected in the ship density data (see Fig. 2.1).
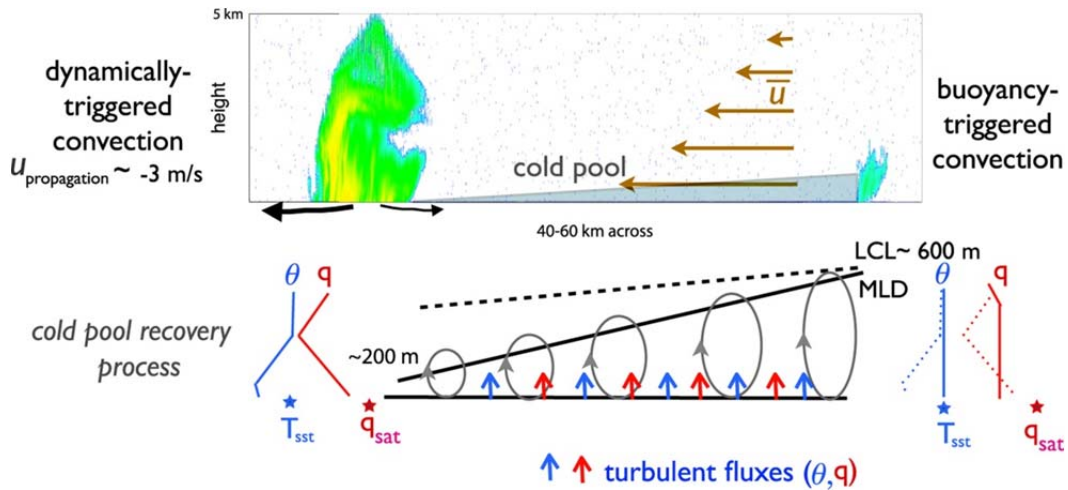
Fig. 5.3: Schematic of propagating precipitating shallow convection and the cold pool recovery. (top) Time–distance cross section of a cold pool, using an X-band radar reflectivity section from 1200 to 1400 UTC 11 January, with time interchanged for distance. Winds are moving from right to left (east to west); $\bar{u}$ is the mean wind speed. (bottom) Thermodynamic recovery of the surface-based mixed layer cold pool. The left (western) end marks the newly developed cold pool, while the right (eastern) end is the fully recovered boundary layer. MLD is mixed layer depth and the LCL is that of a surface parcel; T_{sst} and q_{sat} indicate the sea surface temperature and its saturated specific humidity, with the stars indicating their values relative to those of the vertical profiles of θ and q. From Zuidema et al. (2012), their Fig. 19.

CHAPTER 6

Conclusions

Cold, dense surface outflows (also referred to as cold pools, gravity currents, or density currents) associated with evaporative cooling of air by precipitation have been studied in a wide variety of storm settings (Wilson and Schreiber 1986; Charba 1974; Engerer 2008; Goff 1976; Wakimoto 1982; Droegemeier and Wilhelmson 1987; Houze 1977; Gamache and Houze 1982; Zipser 1977; and many others). While density currents associated with deep, mixed phase-clouds have been studied extensively for decades, it is only relatively recently that such outflows were found to occur below shallow marine clouds. Observational studies have suggested the importance of precipitation outflows to mesoscale organization and precipitation initiation in subtropical cumulus convection (Zuidema et al. 2012; Snodgrass 2009). Previous observational work on marine stratocumulus density currents has utilized data "snapshots" either of aircraft flight leg transects (Terai et al. 2011; Jensen et al. 2000) or single scans of lidar and C-band radar data (Feingold et al. 2010). This study is unique in that it examines the evolution of these density currents to provide a more complete picture of their nature and relationship to the ambient thermodynamic and kinematic environments.

Seventy marine stratocumulus region density currents of ~0.25-2K strength, 100-600 meter depth, and 5-40 km horizontal length are characterized using ship-based data sets including, for the first time, a scanning Doppler Lidar. The observed density currents are 5-10 times thinner and weaker than typical continental thunderstorm cold pools. Density currents were generally associated with moderate or intense local drizzle, thereby strongly implicating them as drizzle outflows. Previous studies using aircraft data assumed an approximately radially-symmetric outflow shape (Terai 2011), whereas most density currents observed from the ship possessed elongated tails of gradually dissipating temperature and density oriented along the mean wind. These elongated tails of the

density current are attributed to the boundary layer shear ($+1$-5 ms^{-1}), which had been neglected in previous work (Feingold et al. 2010; Terai 2013). Updrafts of 0.5-3.5 ms^{-1} in the layer from the surface to 300-900 meters altitude were present along the leading edge of nearly all density current flows. These Doppler-lidar-observed updrafts represent direct evidence for cold-pool-induced updrafts beneath drizzling marine stratocumulus. In previous studies, the updrafts were measured via flight-level anemometer, (Terai 2011) or were inferred from surface convergence (Feingold et al. 2010). However, convective initiation of a new and vigorous drizzle cell along a propagating frontal boundary was rarely observed.

Subcloud cumulus formation in the form of shelf or arc clouds associated with the prefrontal updraft were very often observed. Sometimes these clouds were distinct from the stratocumulus deck and sometimes they extended up into the stratocumulus deck. Surprisingly, density currents frequency peaked after sunrise, approximately 3 hours after the overnight drizzle area and cell number peaks. Density currents preferentially occurred in environments of increased mesoscale boundary layer stability.

Seventy density currents that passed over the RHB during VOCALS-REx are analyzed. Four density currents are examined in three detailed case studies to illustrate the evolution of relatively strong and well-defined density currents. Scanning High Resolution Doppler Lidar (HRDL) captured the evolving horizontal and vertical structures of these features for the first time. Observations from the ship's in situ and remote sensors as well as satellite-retrieved IR cloud fields provide context for these events and allow a comparison of the near surface wind field with the evolving cloud and precipitation field. The prefrontal environment exhibited dry and clean subcloud layers, a well-defined surface mixed layer in the lidar backscatter data, and low magnitude boundary layer vertical motions, indicating that the events commenced in less-coupled boundary layers.

The gross shape of frontal boundaries within the ~16 km horizontal domain of the 1^0 elevation angle lidar ppis differed among cases. The "humidity front" boundary and the frontal zone of the second "convergence case" density current were nearly linear. The Feingold outflow was highly irregular and defined by two distinct, converging flanks that spanned 5-10 km across. The colliding outflows in the Feingold case were found to emanate from a bifurcated coherent drizzling region, rather than from isolated and distinct drizzling regions as was suggested by Feingold et al. (2010). The collision occurred immediately in front of an already intense advancing drizzle cell and therefore was unlikely to have generated a new and distinct drizzle cell. The Feingold outflow was also found to be the strongest in the data set (in terms of perturbations in density and temperature). Collisions between two intense and propagating outflow boundaries—as was observed in this case— were not common. Further contrast in frontal zone features was provided by the first "convergence case" density current. This density current stalled and dissipated over the lidar domain posterior its source drizzle cell, gradually mixing out and trailing out of the lidar domain. Unlike the Feingold case, the collision between this dissipating density current and a second vigorous and propagating density current resulted in initiation of a new and intense drizzle cell along the zone of convergence.

Temperature spikes—which are identified by increases in surface air temperature of more than 0.24 K over 3.5 km followed by anomalously high peak temperatures (see Chapter 2)—occurred 19 times over the study period. In the Feingold case, the temperature spike occurred as a patch of warm, dry, clean air in the near surface layer in advance of the drizzle outflow. Six of these temperature spikes in the data set occurred in air that was not significantly drier and cleaner than the air that preceded them. A physical mechanism for temperature spikes has not been determined. We have included a statistical summary and discussion of the observed temperature spikes in the Appendix.

Seventy density currents fronts were identified throughout a 30 day period of ship meteorological data and used to examine bulk statistics. A minimum density increase threshold was applied commensurate to Terai's (2011) criterion for a cold pool edge. The data were interpolated over a ship-relative advective displacement axis prior to application of a 3.5 km moving window average of ship air density to smooth small-scale variations in air mass properties and to allow a more physical interpretation of density current scale and structure. In addition to the frontal zone, the full duration of each density current was identified using a recursive technique to find the core (peak density) and tail (dissipating) regions of the advancing air mass. Time periods corresponding to front, core, and tail regions of density currents passing over the ship were used to derive bulk statistics in the study region and to further characterize density current kinematic features observed in the lidar data.

Ship transects lengths of density currents tail regions were generally found to be larger than front and core regions. The front and core regions were between 3 km and 17 km in length, and tail regions varied in size from 2 to 27 km. Surface temperature decreases across the front and core region of each density current ranged from approximately -0.15K to -2K. Water vapor mixing ratio (q_v) changes across the front and core region varied from approximately -0.75 to 1.25 g kg^{-1}. Cases in which q_v decreased across the front and core region are believed to result from the presence of very nearly saturated near surface air in advance of the cooler air within the density current. Density current depth was estimated from lidar rhi Doppler velocity and backscatter intensity data. Embedded within the 33 surveyed density currents, the depth of strongest flow was between 100 and 500 meters, with a zone of increased shear observed above this layer between 200 and 900 meters altitude.

Updrafts occurring in the immediate vicinity of density current fronts were estimated from upward pointing lidar in the 24 cases where these data were available. The updrafts extended between

300 and 1000 meters height, with a maximum intensity of 3.5 m s^{-1}. Clouds often attenuated the lidar signal at the tops of the updrafts, so some updraft heights were underestimated. The updrafts showed some variations in overall shape, which indicate complexity in lifting duration and the altitudes at which the lifting progressed. Updrafts were observed slanted back over and above the front density current in many cases, likely due to the presence of a counterflow over the top of the density current front. Cloud photos corroborated evidence from lidar of the existence of shelf clouds along and over density current fronts. Variable cloud heights, broken stratocumulus layers, and well-defined surface mixed layers suggest that less-coupled boundary layers were also observed in a majority of cases.

Density currents were observed in both open and closed cell regions as far east as 76 W. However, they were most common west of 80W. Approximately half of the events occurred within or beside an area of open cells that was seen in the IR satellite domain from 26 Oct through 28 Oct (total of 34 cases). Consistent with previous studies, the open cell region was associated with the highest conditional rain rates and the lowest accumulation and coarse mode aerosol concentrations observed during the cruise. Surface aerosol in Aitken, accumulation, and coarse modes were however not observed to consistently drop across density current fronts. Changes in concentration showed poor correlation with absolute concentrations. Our finding supports the conclusion that the signature of aerosol scavenging is insufficient to persist very near the ocean surface. This is perhaps because the higher wind speeds and surface aerosol fluxes increased stability in lower boundary layer and enhanced hygroscopic growth within the density current.

Density currents occurred throughout the day, though they were most frequent from late night to late morning and least frequent in the early evening. The mode of the diurnal cycle of density current frequency was between 5AM and 11AM local time, 1-7 hours after the overnight peak in areal average rain rates observed in the radar domain during the cruise (Burleyson et al. 2013). An

explanation for this surprising finding may come from analysis of sounding-derived dry Brunt-Väisälä frequency from the lowest 100 meters of the atmosphere to the layer 100 meters below the median cloud base. We found that high Brunt-Väisälä frequencies in this layer are associated with two factors: daytime heating of the stratocumulus layer and areal average rain rates in excess of ~0.5 mm d^{-1} within 15 km of the ship. Both daytime heating and evaporative cooling of drizzle have been proposed as mechanisms for boundary layer stabilization in this region (Turton and Nicholls 1987; Duynkerke 1989; Wang and Wang 1994; Bretherton and Wyant 1997; Wang and Feingold 2009; Burleyson et al. 2013). Boundary layer stabilization, in turn, is associated with reduced turbulent moisture transport from the ocean to the stratocumulus deck. The sounding data confirm the somewhat counterintuitive conclusion that density currents are closely associated with both stronger precipitation rates and more stable boundary layers. The data are consistent with the hypothesis that density currents are providing an alternative vertical moisture transport mechanism via lifting along their frontal zones, in a manner analogous to RKW theory (Weisman and Rotunno 2004). This mechanism could persist into the early morning and daylight hours when cloud-driven turbulent transport wanes and boundary layer stability increases.

Approximately 88% of drizzle scenes captured when density currents crossed the ship were accompanied by areal average rain rates in excess of 0.1 mm d^{-1} within 15 km of the ship. By comparison, only about 10% off all drizzle scenes exhibited local areal average rain rates in this range. This fact suggests that moderate and intense drizzle is likely to be accompanied by a detectible near-surface outflow within ~10-15 km of the drizzle cell. Conversely, density currents were also observed when areal average rain rates nearest the ship were lower (0.001 – 0.1 mm d^{-1}). The relationship of these features to the gross and fine structure of drizzle cells is rather complex and difficult to summarize via a comparison of lidar-derived density current location and the radar-derived precipitation field. The spatial decorrelation of density currents from the boundaries of

precipitating regions can be partly explained by the fact that drizzle outflows were observed to trail behind the source drizzle cell. This phenomenon leads to a distinctive "comet" outflow shape which allowed the ship to sample a subset of density currents emanating from drizzle cells that had completely bypassed the ship.

We present a new conceptual model for an isolated drizzle outflow complex propagating in a less-coupled boundary layer. The outflow complex can be thought as the kinematic equivalent of a drizzle-induced cold pool. This model integrates observations of the evolution of near surface horizontal flow perturbation associated with density currents. It also addresses differential advection of the cloud layer with respect to the near surface layer, which was commonly observed in less-coupled boundary layers. The outflow complex is composed of successive outflow 'pulses' generated by the drizzle cell as it propagates faster than the surface wind field in the direction of the mean wind. The back, right and left side of each successive outflow pulse propagates more slowly in the direction of the mean wind than the advancing drizzle cell which produced it. As these portions of the outflow are overtaken by the advancing drizzle cell, the resulting outflow complex develops a comet-like, oblong shape. To the left and right of the drizzle cell track, the outflow complex is bounded by density currents propagating orthogonally to the mean wind in opposite directions. Density currents propagate in parallel bands that gradually dissipate and stall towards the rear of the outflow complex. It should be noted that the outflow complex does not have a well-defined back side in this model. The back edge of the outflow complex is dominated by turbulent mixing and gradual dissipation, rather than dynamical pressure perturbations that drive the propagating density current frontal zones. Our model of the evolution of this dissipating 'tail' region of the outflow complex is similar to the model presented in Zuidema et al. (2012) for dissipating trade wind cumulus cold pools.

135

An additional feature of our model is convective activity, denoted by cloud and virga, along the propagating frontal zones. Convective initiation along the front, right, and left propagating boundaries of the outflow complex may be associated with changes in the shape and extent of the source drizzle cell boundary. The contribution of outflow boundaries to convective activity is proposed to be most significant in the immediate vicinity of the front edge of the outflow complex. Here, the density perturbation is strong and the density current flow is most closely aligned with the forward track of the active drizzle cell. Moisture lifted above the density outflow boundary in front of the active drizzle cell would most likely to be carried by the density current counterflow and drizzle cell inflow back and over the density current and into the advancing drizzle cell's updraft region. In this way, drizzle cells that possess a near-surface outflow may be maintained by the moisture transported by their outflow boundaries.

REFERENCES

Allen, G. and Coauthors, 2011: South East Pacific atmospheric composition and variability sampled along 20° S during VOCALS-REx. *Atmos. Chem. Phys.*, **11**, 5237–5262, doi:10.5194/acp-11-5237-2011.

Bates, T. S. and Coauthors, 2008: Boundary layer aerosol chemistry during TexAQS/GoMACCS 2006: Insights into aerosol sources and transformation processes. *J. Geophys. Res.*, **113**, D00F01, doi:10.1029/2008JD010023.

Bretherton, C. S., and M. C. Wyant, 1997: Moisture Transport, Lower-Tropospheric Stability, and Decoupling of Cloud-Topped Boundary Layers. *Journal of the Atmospheric Sciences*, **54**, 148–167, doi:10.1175/1520-0469(1997)054<0148:MTLTSA>2.0.CO;2.

Bretherton, C. S. and Coauthors, 2004: The Epic 2001 Stratocumulus Study. *Bulletin of the American Meteorological Society*, **85**, 967–977, doi:10.1175/BAMS-85-7-967.

Browning, K. A., and R. Wexler, 1968: The Determination of Kinematic Properties of a Wind Field Using Doppler Radar. *Journal of Applied Meteorology*, **7**, 105–113, doi:10.1175/1520-0450(1968)007<0105:TDOKPO>2.0.CO;2.

Burleyson, , S de Szoeke, SE Yuter, M Wilbanks, A Brewer, 2013: Observations of the Diurnal Cycle of Southeast Pacific Marine Stratocumulus Clouds and Precipitation, *Journal of Atmospheric Sciences*, Submitted.

Capaldo, K. P., P. Kasibhatla, and S. N. Pandis, 1999: Is aerosol production within the remote marine boundary layer sufficient to maintain observed concentrations? *Journal of Geophysical Research: Atmospheres*, **104**, 3483–3500, doi:10.1029/1998JD100080.

Charba, J., 1974: Application of Gravity Current Model to Analysis of Squall-Line Gust Front. *Monthly Weather Review*, **102**, 140–156, doi:10.1175/1520-0493(1974)102<0140:AOGCMT>2.0.CO;2.

Charlson, R. J., J. E. Lovelock, M. O. Andreae, and S. G. Warren, 1987: Oceanic phytoplankton, atmospheric sulphur, cloud albedo and climate. *Nature*, **326**, 655–661, doi:10.1038/326655a0.

Comstock, K. K., R. Wood, S. E. Yuter, and C. S. Bretherton, 2004: Reflectivity and rain rate in and below drizzling stratocumulus. *Quarterly Journal of the Royal Meteorological Society*, **130**, 2891–2918, doi:10.1256/qj.03.187.

Comstock, K. K., C. S. Bretherton, and S. E. Yuter, 2005: Mesoscale Variability and Drizzle in Southeast Pacific Stratocumulus. *Journal of the Atmospheric Sciences*, **62**, 3792–3807, doi:10.1175/JAS3567.1.

Comstock, K. K., S. E. Yuter, R. Wood, and C. S. Bretherton, 2007: The Three-Dimensional Structure and Kinematics of Drizzling Stratocumulus. *Monthly Weather Review*, **135**, 3767–3784, doi:10.1175/2007MWR1944.1.

Craig Goff, R., 1976: Vertical Structure of Thunderstorm Outflows. *Monthly Weather Review*, **104**, 1429–1440, doi:10.1175/1520-0493(1976)104<1429:VSOTO>2.0.CO;2.

Droegemeier, K. K., and R. B. Wilhelmson, 1987: Numerical Simulation of Thunderstorm Outflow Dynamics. Part I: Outflow Sensitivity Experiments and Turbulence Dynamics. *Journal of the Atmospheric Sciences*, **44**, 1180–1210, doi:10.1175/1520-0469(1987)044<1180:NSOTOD>2.0.CO;2.

Duynkerke, P. G., 1989: The Diurnal Variation of a Marine Stratocumulus Layer: A Model Sensitivity Study. *Monthly Weather Review*, **117**, 1710–1725, doi:10.1175/1520-0493(1989)117<1710:TDVOAM>2.0.CO;2.

Engerer, N. A., D. J. Stensrud, and M. C. Coniglio, 2008: Surface Characteristics of Observed Cold Pools. *Monthly Weather Review*, **136**, 4839–4849, doi:10.1175/2008MWR2528.1.

Fairall, C. W., A. B. White, J. B. Edson, and J. E. Hare, 1997: Integrated Shipboard Measurements of the Marine Boundary Layer. *Journal of Atmospheric and Oceanic Technology*, **14**, 338–359, doi:10.1175/1520-0426(1997)014<0338:ISMOTM>2.0.CO;2.

Feingold, G., W. R. Cotton, S. M. Kreidenweis, and J. T. Davis, 1999: The Impact of Giant Cloud Condensation Nuclei on Drizzle Formation in Stratocumulus: Implications for Cloud Radiative Properties. *Journal of the Atmospheric Sciences*, **56**, 4100–4117, doi:10.1175/1520-0469(1999)056<4100:TIOGCC>2.0.CO;2.

Feingold, G., I. Koren, H. Wang, H. Xue, and W. A. Brewer, 2010: Precipitation-generated oscillations in open cellular cloud fields. *Nature*, **466**, 849–852, doi:10.1038/nature09314.

Fovell, R. G., 2002: Upstream influence of numerically simulated squall-line storms. *Quarterly Journal of the Royal Meteorological Society*, **128**, 893–912, doi:10.1256/0035900021643737.

Frehlich, R., 2001: Estimation of Velocity Error for Doppler Lidar Measurements. *Journal of Atmospheric and Oceanic Technology*, **18**, 1628–1639, doi:10.1175/1520-0426(2001)018<1628:EOVEFD>2.0.CO;2.

Frehlich, R. G., and M. J. Yadlowsky, 1994: Performance of Mean-Frequency Estimators for Doppler Radar and Lidar. *Journal of Atmospheric and Oceanic Technology*, **11**, 1217–1230, doi:10.1175/1520-0426(1994)011<1217:POMFEF>2.0.CO;2.

Gamache, J. F., and R. A. Houze, 1982: Mesoscale Air Motions Associated with a Tropical Squall Line. *Monthly Weather Review*, **110**, 118–135, doi:10.1175/1520-0493(1982)110<0118:MAMAWA>2.0.CO;2.

Gamache, J. F., and R. A. Houze, 1985: Further Analysis of the Composite Wind and Thermodynamic Structure of the 12 September GATE Squall Line. *Monthly Weather Review*, **113**, 1241–1260, doi:10.1175/1520-0493(1985)113<1241:FAOTCW>2.0.CO;2.

Glantz, P., K. J. Noone, and S. R. Osborne, 2003: Scavenging efficiencies of aerosol particles in marine stratocumulus and cumulus clouds. *Quarterly Journal of the Royal Meteorological Society*, **129**, 1329–1350, doi:10.1256/qj.02.73.

Gossard, E. E., and R. G. Strauch, 1983: *Radar Observations of Clear Air and Clouds*. Elsevier, pp. 292

Grund, C. J., R. M. Banta, J. L. George, J. N. Howell, M. J. Post, R. A. Richter, and A. M. Weickmann, 2001: High-Resolution Doppler Lidar for Boundary Layer and Cloud Research. *Journal of Atmospheric and Oceanic Technology*, **18**, 376–393, doi:10.1175/1520-0426(2001)018<0376:HRDLFB>2.0.CO;2.

Haertel, P. T., R. H. Johnson, and S. N. Tulich, 2001: Some Simple Simulations of Thunderstorm Outflows. *Journal of the Atmospheric Sciences*, **58**, 504–516, doi:10.1175/1520-0469(2001)058<0504:SSSOTO>2.0.CO;2.

Harrison, S. J., J. R. Mecikalski, and K. R. Knupp, 2009: Analysis of Outflow Boundary Collisions in North-Central Alabama. *Weather and Forecasting*, **24**, 1680–1690, doi:10.1175/2009WAF2222268.1.

Hill, R. J., W. A. Brewer, and S. C. Tucker, 2008: Platform-Motion Correction of Velocity Measured by Doppler Lidar. *Journal of Atmospheric and Oceanic Technology*, **25**, 1369–1382, doi:10.1175/2007JTECHA972.1.

Houze, R. A., 1977: Structure and Dynamics of a Tropical Squall–Line System. *Monthly Weather Review*, **105**, 1540–1567, doi:10.1175/1520-0493(1977)105<1540:SADOAT>2.0.CO;2.

Houze, R. A., 2004: Mesoscale convective systems. *Reviews of Geophysics*, **42**, n/a–n/a, doi:10.1029/2004RG000150.

Intrieri, J. M., G. L. Stephens, W. L. Eberhard, and T. Uttal, 1993: A Method for Determining Cirrus Cloud Particle Sizes Using Lidar and Radar Backscatter Technique. *Journal of Applied Meteorology*, **32**, 1074–1082, doi:10.1175/1520-0450(1993)032<1074:AMFDCC>2.0.CO;2.

Jensen, J. B., S. Lee, P. B. Krummel, J. Katzfey, and D. Gogoasa, 2000: Precipitation in marine cumulus and stratocumulus.: Part I: Thermodynamic and dynamic observations of closed cell circulations and cumulus bands. *Atmospheric Research*, **54**, 117–155, doi:10.1016/S0169-8095(00)00040-5.

Jones, C. R., C. S. Bretherton, and D. Leon, 2011: Coupled vs. decoupled boundary layers in VOCALS-REx. *Atmos. Chem. Phys.*, **11**, 7143–7153, doi:10.5194/acp-11-7143-2011.

Kingsmill, D. E., and N. Andrew Crook, 2003: An Observational Study of Atmospheric Bore Formation from Colliding Density Currents. *Monthly Weather Review*, **131**, 2985–3002, doi:10.1175/1520-0493(2003)131<2985:AOSOAB>2.0.CO;2.

Kleinman, L. I. and Coauthors, 2012: Aerosol concentration and size distribution measured below, in, and above cloud from the DOE G-1 during VOCALS-REx. *Atmos. Chem. Phys.*, **12**, 207–223, doi:10.5194/acp-12-207-2012.

Kot, SC and JE Simspon, 1987: Laboratory Experiments on Two Crossing Flows, In Proc. 1st Conf. Fluid Mech., Beijing, 1987, pp. 731-6. Beijing University Press.

Leon, D. C., Z. Wang, and D. Liu, 2008: Climatology of drizzle in marine boundary layer clouds based on 1 year of data from CloudSat and Cloud-Aerosol Lidar and Infrared Pathfinder Satellite Observations (CALIPSO). *J. Geophys. Res.*, **113**, 15 PP., doi:200810.1029/2008JD009835.

Liu, C., and M. W. Moncrieff, 1996: An Analytical Study of Density Currents in Sheared, Stratified Fluids Including the Effects of Latent Heating. *Journal of the Atmospheric Sciences*, **53**, 3303–3312, doi:10.1175/1520-0469(1996)053<3303:AASODC>2.0.CO;2.

Mahoney, W. P., 1988: Gust Front Characteristics and the Kinematics Associated with Interacting Thunderstorm Outflows. *Monthly Weather Review*, **116**, 1474–1492, doi:10.1175/1520-0493(1988)116<1474:GFCATK>2.0.CO;2.

Miller, M. A., and S. E. Yuter, 2013: Detection and characterization of heavy drizzle cells within subtropical marine stratocumulus using AMSR-E 89-GHz passive microwave measurements. *Atmospheric Measurement Techniques*, **6**, 1–13, doi:10.5194/amt-6-1-2013.

O'Dowd, C. D., and G. de Leeuw, 2007: Marine aerosol production: a review of the current knowledge. *Phil. Trans. R. Soc. A*, **365**, 1753–1774, doi:10.1098/rsta.2007.2043.

O'Dowd, C. D. and Coauthors, 2002: Marine aerosol formation from biogenic iodine emissions. *Nature*, **417**, 632–636, doi:10.1038/nature00775.

Ovadnevaite, J., D. Ceburnis, M. Canagaratna, H. Berresheim, J. Bialek, G. Martucci, D. R. Worsnop, and C. O'Dowd, 2012: On the effect of wind speed on submicron sea salt mass concentrations and source fluxes. *Journal of Geophysical Research*, **117**, doi:10.1029/2011JD017379. http://www.agu.org/pubs/crossref/pip/2011JD017379.shtml (Accessed April 12, 2013).

Pandya, R. E., and D. R. Durran, 1996: The Influence of Convectively Generated Thermal Forcing on the Mesoscale Circulation around Squall Lines. *Journal of the Atmospheric Sciences*, **53**, 2924–2951, doi:10.1175/1520-0469(1996)053<2924:TIOCGT>2.0.CO;2.

Petters, M. D., J. R. Snider, B. Stevens, G. Vali, I. Faloona, and L. M. Russell, 2006: Accumulation mode aerosol, pockets of open cells, and particle nucleation in the remote subtropical Pacific marine boundary layer. *J. Geophys. Res.*, **111**, D02206, doi:10.1029/2004JD005694.

Rottman, J. W., and J. E. Simpson, 1989: The formation of internal bores in the atmosphere: A laboratory model. *Quarterly Journal of the Royal Meteorological Society*, **115**, 941–963, doi:10.1002/qj.49711548809.

Rotunno, R., J. B. Klemp, and M. L. Weisman, 1988: A Theory for Strong, Long-Lived Squall Lines. *Journal of the Atmospheric Sciences*, **45**, 463–485, doi:10.1175/1520-0469(1988)045<0463:ATFSLL>2.0.CO;2.

Ryan, M, M. J. Post, B. Martner, J. Novak and L. Davis, 2002: *The NOAA Ron Brown's shipboard Doppler precipitation radar. 6th Symposium on Integrated Observing Systems,* American Meteorological Society, Orlando, Florida, January 2002.

Rye, B. J. and Hardesty, R. M., 1993: *Discrete Spectral Peak Estimation in Incoherent Backscatter Heterodyne Lidar. I. Spectral Accumulation and the Cramer-Rao Lower Bound, IEEE Trans. Geo. Sci. Remote Sensing*, 31,16-27.

Savic-Jovcic, V., and B. Stevens, 2008: The Structure and Mesoscale Organization of Precipitating Stratocumulus. *Journal of the Atmospheric Sciences*, **65**, 1587–1605, doi:10.1175/2007JAS2456.1.

Shank, L. M. and Coauthors, 2012: Organic matter and non-refractory aerosol over the remote Southeast Pacific: oceanic and combustion sources. *Atmos. Chem. Phys.*, **12**, 557–576, doi:10.5194/acp-12-557-2012.

Sharon, T. M., B. A. Albrecht, H. H. Jonsson, P. Minnis, M. M. Khaiyer, T. M. van Reken, J. Seinfeld, and R. Flagan, 2006: Aerosol and Cloud Microphysical Characteristics of Rifts and Gradients in Maritime Stratocumulus Clouds. *Journal of the Atmospheric Sciences*, **63**, 983–997, doi:10.1175/JAS3667.1.

Simpson, J. E., 1997: *Gravity Currents: In the Environment and the Laboratory*, 2nd Edn. Cambridge University Press.

Snodgrass, E. R., L. Di Girolamo, and R. M. Rauber, 2009: Precipitation Characteristics of Trade Wind Clouds during RICO Derived from Radar, Satellite, and Aircraft Measurements. *Journal of Applied Meteorology and Climatology*, **48**, 464–483, doi:10.1175/2008JAMC1946.1.

Srivastava, R. C., 1987: A Model of Intense Downdrafts Driven by the Melting and Evaporation of Precipitation. *Journal of the Atmospheric Sciences*, **44**, 1752–1774, doi:10.1175/1520-0469(1987)044<1752:AMOIDD>2.0.CO;2.

Stevens, B., G. Vali, K. Comstock, R. Wood, M. C. Van Zanten, P. H. Austin, C. S. Bretherton, and D. H. Lenschow, 2005: POCKETS OF OPEN CELLS AND DRIZZLE IN MARINE STRATOCUMULUS. *Bulletin of the American Meteorological Society*, **86**, 51–57, doi:10.1175/BAMS-86-1-51.

De Szoeke, S. P., C. W. Fairall, D. E. Wolfe, L. Bariteau, and P. Zuidema, 2010: Surface Flux Observations on the Southeastern Tropical Pacific Ocean and Attribution of SST Errors in

Coupled Ocean–Atmosphere Models. *Journal of Climate*, **23**, 4152–4174, doi:10.1175/2010JCLI3411.1.

Tang, I. N., 1996: Chemical and size effects of hygroscopic aerosols on light scattering coefficients. *J. Geophys. Res.*, **101**, PP. 19,245–19,250, doi:199610.1029/96JD03003.

Tang, I. N., A. C. Tridico, and K. H. Fung, 1997: Thermodynamic and optical properties of sea salt aerosols. *J. Geophys. Res.*, **102**, PP. 23,269–23,275, doi:199710.1029/97JD01806.

Terai, Christopher R., 2011: Drizzle and the aerosol indirect effect in marine stratocumulus. Masters thesis, Department of Atmospheric Sciences, University of Washington.

Terai, C. R., and R. Wood, 2013: Aircraft observations of cold pools under marine stratocumulus. *Atmospheric Chemistry and Physics Discussions*, **13**, 11023–11069, doi:10.5194/acpd-13-11023-2013.

Tucker, S. C., C. J. Senff, A. M. Weickmann, W. A. Brewer, R. M. Banta, S. P. Sandberg, D. C. Law, and R. M. Hardesty, 2009: Doppler Lidar Estimation of Mixing Height Using Turbulence, Shear, and Aerosol Profiles. *Journal of Atmospheric and Oceanic Technology*, **26**, 673–688, doi:10.1175/2008JTECHA1157.1.

Turton, J. D., and S. Nicholls, 1987: A Study of the Diurnal Variation of Stratocumulus Using A Multiple Mixed Layer Model. *Quarterly Journal of the Royal Meteorological Society*, **113**, 969–1009, doi:10.1002/qj.49711347712.

Wakimoto, R. M., 1982: The Life Cycle of Thunderstorm Gust Fronts as Viewed with Doppler Radar and Rawinsonde Data. *Monthly Weather Review*, **110**, 1060–1082, doi:10.1175/1520-0493(1982)110<1060:TLCOTG>2.0.CO;2.

Wakimoto, R. M., and D. E. Kingsmill, 1995: Structure of an Atmospheric Undular Bore Generated from Colliding Boundaries during CaPE. *Monthly Weather Review*, **123**, 1374–1393, doi:10.1175/1520-0493(1995)123<1374:SOAAUB>2.0.CO;2.

Wang, H., and G. Feingold, 2009: Modeling Mesoscale Cellular Structures and Drizzle in Marine Stratocumulus. Part II: The Microphysics and Dynamics of the Boundary Region between Open and Closed Cells. *Journal of the Atmospheric Sciences*, **66**, 3257–3275, doi:10.1175/2009JAS3120.1.

Wang, H., G. Feingold, R. Wood, and J. Kazil, 2010: Modelling microphysical and meteorological controls on precipitation and cloud cellular structures in Southeast Pacific stratocumulus. *Atmos. Chem. Phys.*, **10**, 6347–6362, doi:10.5194/acp-10-6347-2010.

Wang, H., P. J. Rasch, and G. Feingold, 2011: Manipulating marine stratocumulus cloud amount and albedo: a process-modelling study of aerosol-cloud-precipitation interactions in response to injection of cloud condensation nuclei. *Atmos. Chem. Phys.*, **11**, 4237–4249, doi:10.5194/acp-11-4237-2011.

Wang, S., and Q. Wang, 1994: Roles of Drizzle in a One-Dimensional Third-Order Turbulence Closure Model of the Nocturnal Stratus-Topped Marine Boundary Layer. *Journal of the Atmospheric Sciences*, **51**, 1559–1576, doi:10.1175/1520-0469(1994)051<1559:RODIAO>2.0.CO;2.

Weisman, M. L., and R. Rotunno, 2004: "A Theory for Strong Long-Lived Squall Lines" Revisited. *Journal of the Atmospheric Sciences*, **61**, 361–382, doi:10.1175/1520-0469(2004)061<0361:ATFSLS>2.0.CO;2.

Wilson, J. W., and W. E. Schreiber, 1986: Initiation of Convective Storms at Radar-Observed Boundary-Layer Convergence Lines. *Monthly Weather Review*, **114**, 2516–2536, doi:10.1175/1520-0493(1986)114<2516:IOCSAR>2.0.CO;2.

Wood, R., 2012: Stratocumulus Clouds. *Monthly Weather Review*, 120209141617009, doi:10.1175/MWR-D-11-00121.1.

Wood, R., C. S. Bretherton, D. Leon, A. D. Clarke, P. Zuidema, G. Allen, and H. Coe, 2011: An aircraft case study of the spatial transition from closed to open mesoscale cellular convection over the Southeast Pacific. *Atmos. Chem. Phys.*, **11**, 2341–2370, doi:10.5194/acp-11-2341-2011.

Wulfmeyer, V., and G. Feingold, 2000: On the relationship between relative humidity and particle backscattering coefficient in the marine boundary layer determined with differential absorption lidar. *Journal of Geophysical Research: Atmospheres*, **105**, 4729–4741, doi:10.1029/1999JD901030.

Wulfmeyer, V., M. Randall, A. Brewer, and R. M. Hardesty, 2000: 2-μm Doppler lidar transmitter with high frequency stability and low chirp. *Opt. Lett.*, **25**, 1228–1230, doi:10.1364/OL.25.001228.

Zipser, E. J., 1977: Mesoscale and Convective–Scale Downdrafts as Distinct Components of Squall-Line Structure. *Monthly Weather Review*, **105**, 1568–1589, doi:10.1175/1520-0493(1977)105<1568:MACDAD>2.0.CO;2.

Zuidema, P., E. R. Westwater, C. Fairall, and D. Hazen, 2005: Ship-based liquid water path estimates in marine stratocumulus. *Journal of Geophysical Research: Atmospheres*, **110**, n/a–n/a, doi:10.1029/2005JD005833.

Zuidema, P. and Coauthors, 2012: On Trade Wind Cumulus Cold Pools. *Journal of the Atmospheric Sciences*, **69**, 258–280, doi:10.1175/JAS-D-11-0143.1.

APPENDIX

APPENDIX A

Temperature Spike Discussion

During the 30 days analyzed in the VOCALS-REx ship data set, nineteen temperature spikes were identified using the methods outlined in Chapter 2. Two of the temperature spikes were observed during the case studies (Chapter 3). One was observed immediately prior to the Feingold outflow (see Figs. 3.8 and 3.9) and the other was during the period when a convergence zone between two density currents was closing in on the ship (see Figs. 3.14 and 3.15). In addition to the sudden increase in temperature and anomalously high maximum temperatures which defined these events, the air measured during the temperature spike was often drier and sometimes cleaner than before its onset. Fig. A.1 shows the change in temperature and moisture observed across the onset of each of the temperature spikes identified in the data series. Temperature increased by 0.3 K to 1.6 K and moisture changed by between -1.8 g kg^{-1} and 0.3 g kg^{-1} across the onset of the temperature spike. Notably, the temperature spike in advance of the Feingold outflow was among the driest observed. Also, the temperature spikes that were bounded on both sides by a density current—such as the convergence zone—generally showed a smaller drop in mixing ratio and a larger increase in temperature than those that were not.

We were not able to determine a physical mechanism which could explain the temperature spikes. We suggest that the air sampled at the surface during these events originated from above, specifically in the subcloud mixed layer above the surface mixed layer. Higher potential temperatures and lower moisture content were often observed in the subcloud mixed layer, and aerosol concentrations may also have been significantly lower than at the surface. This suggests that the air aloft may have been ingested or entrained into the surface mixed layer and carried down to the

surface via an unknown process. The mechanisms behind near-surface temperature spikes may be investigated in future studies.
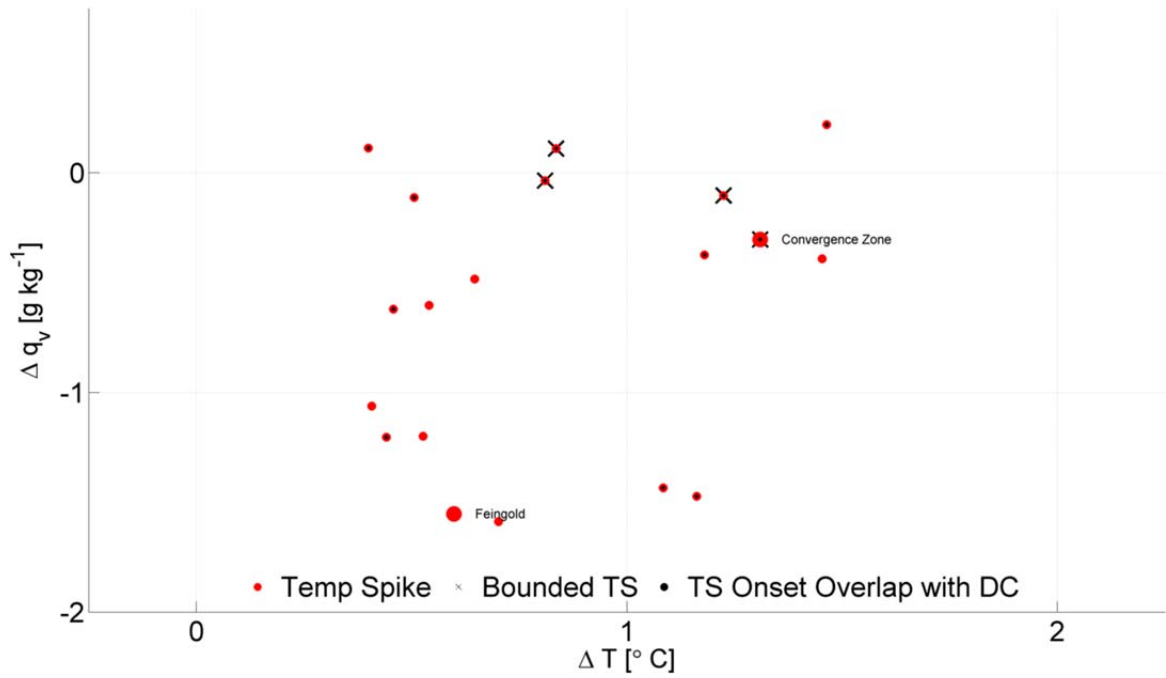
Fig. A.1: The change in vapor mixing ratio (q_v) vs. the change in temperature observed from the start of the temperature spike to the point where temperature is at a maximum (TSmax) Inset red dots indicate when a temperature spike onset overlapped with the density current tail. Points with a black 'x' overlaid are bounded on both sides by a density current. Temperature spikes examined in the case study analysis presented in Chapter 3 are annotated.